# The role of DNA damage in mammalian metabolic regulation

Ioannidou Anna

PhD thesis

Heraklion, 2019

**Τριμελής Συμβουλευτική Επιτροπή**

- **Γαρίνης Γιώργος:** Καθηγητής, τμήμα Βιολογίας, Πανεπιστήμιο Κρήτης και συνεργαζόμενο μέλος ΔΕΠ, Ινστιτούτο Μοριακής Βιολογίας και Βιοτεχνολογίας-ΙΤΕ
- **Τσατσάνης Χρήστος:** Καθηγητής, Ιατρική Σχολή, Πανεπιστήμιο Κρήτης και συνεργαζόμενο μέλος ΔΕΠ, Ινστιτούτο Μοριακής Βιολογίας και Βιοτεχνολογίας-ΙΤΕ
- **Παπαματθαιάκης Ιωσήφ:** Καθηγητής, τμήμα Βιολογίας, Πανεπιστήμιο Κρήτης και συνεργαζόμενο μέλος ΔΕΠ, Ινστιτούτο Μοριακής Βιολογίας και Βιοτεχνολογίας-ΙΤΕ

**Επταμελής Εξεταστική Επιτροπή**

- **Γαρίνης Γιώργος:** Καθηγητής, τμήμα Βιολογίας, Πανεπιστήμιο Κρήτης και συνεργαζόμενο μέλος ΔΕΠ, Ινστιτούτο Μοριακής Βιολογίας και Βιοτεχνολογίας-ΙΤΕ
- **Τσατσάνης Χρήστος:** Καθηγητής, Ιατρική Σχολή, Πανεπιστήμιο Κρήτης και συνεργαζόμενο μέλος ΔΕΠ, Ινστιτούτο Μοριακής Βιολογίας και Βιοτεχνολογίας-ΙΤΕ
- **Δελιδάκης Χρήστος:** Καθηγητής, τμήμα Βιολογίας, Πανεπιστήμιο Κρήτης και συνεργαζόμενο μέλος ΔΕΠ, Ινστιτούτο Μοριακής Βιολογίας και Βιοτεχνολογίας-ΙΤΕ
- **Τζαμαρίας Δημήτρης:** Αναπληρωτής Καθηγητής, τμήμα Βιολογίας, Πανεπιστήμιο Κρήτης
- **Καρδάσης Δημήτρης:** Καθηγητής, Ιατρική Σχολή, Πανεπιστήμιο Κρήτης και συνεργαζόμενο μέλος ΔΕΠ, Ινστιτούτο Μοριακής Βιολογίας και Βιοτεχνολογίας-ΙΤΕ
- **Σπηλιανάκης Χαράλαμπος:** Αναπληρωτής Καθηγητής, τμήμα Βιολογίας, Πανεπιστήμιο Κρήτης και συνεργαζόμενο μέλος ΔΕΠ, Ινστιτούτο Μοριακής Βιολογίας και Βιοτεχνολογίας-ΙΤΕ
- **Χαλεπάκης Γιώργος:** Καθηγητής, τμήμα Βιολογίας, Πανεπιστήμιο Κρήτης και συνεργαζόμενο μέλος ΔΕΠ, Ινστιτούτο Μοριακής Βιολογίας και Βιοτεχνολογίας-ΙΤΕ

## Ευχαριστίες

Με την παρούσα εργασία επισφραγίζεται ένα ταξίδι 11 ετών, που ξεκίνησε με τις προπτυχιακές μου σπουδές στο πανεπιστήμιο Κρήτης. Ήταν ένα μεγάλο (όχι μόνο χρονικά) κεφάλαιο στη ζωή μου που, παρά τις δυσκολίες, μου προσέφερε χαρούμενες αναμνήσεις, γνώσεις, διδάγματα, όπως υπομονή και επιμονή, αλλά και ανθρώπινες σχέσεις. Ήταν μια ανεκτίμητη εμπειρία που όμως δε θα μπορούσε να είχε ολοκληρωθεί χωρίς τη συμβολή κάποιων ανθρώπων. Ανθρώπων που με στήριξαν ο κάθε ένας με το δικό του τρόπο, στάθηκαν δίπλα μου, μου έδιναν ώθηση να συνεχίζω και αποτέλεσαν για μένα πηγή έμπνευσης, δύναμης και αισιοδοξίας.

Αρχικά, θα ήθελα να ευχαριστήσω τον υπεύθυνο καθηγητή μου Γιώργο Γαρίνη, για όλα όσα μου προσέφερε, όχι μόνο κατά τη διάρκεια του διδακτορικού, αλλά καθ' όλη τη διάρκεια των τελευταίων 8 χρόνων που δουλέψαμε μαζί, στα πλαίσια της πρακτικής, πτυχιακής και μεταπτυχιακής μου εργασίας. Η πόρτα του γραφείου του ήταν πάντα ανοιχτή και έβρισκε κάθε φορά χρόνο να συζητήσουμε κάθε ζήτημα που προέκυπτε. Πρόθυμα και με υπομονή μου έδειχνε το δρόμο για τη σωστή αξιολόγηση, συλλογισμό και προσέγγιση του κάθε επιστημονικού ή πειραματικού προβληματισμού μου. Τον ευχαριστώ για τις γνώσεις, την καθοδήγηση, τον τρόπο σκέψης, τις συμβουλές, καθώς και την υποστήριξή του σε εύκολες και δύσκολες στιγμές, τόσο σε επαγγελματικό, όσο και σε προσωπικό επίπεδο.

Θα ήθελα να ευχαριστήσω θερμά και τα μέλη της τριμελούς συμβουλευτικής επιτροπής, τον κ. Παπαματθαιάκη και τον κ. Τσατσάνη, που από την αρχή της διατριβής με βοήθησαν με συμβουλές και εύστοχα σχόλια. Όπως επίσης και τα υπόλοιπα μέλη της επταμελούς επιτροπής που δέχτηκαν πρόθυμα να συμμετάσχουν και να αφιερώσουν χρόνο για την αξιολόγηση της παρούσας εργασίας. Δε θα μπορούσα να μην αναφέρω και τους καθηγητές του τμήματος Βιολογίας του Πανεπιστημίου Κρήτης, που με ενέπνευσαν και έθεσαν τις βάσεις για τη μετέπειτα πορεία μου.

Ένα μεγάλο ευχαριστώ και στα μέλη του εργαστηρίου, πρώην και νυν, με τα οποία μοιράστηκα την κάθε μέρα τα τελευταία 8 χρόνια. Την Ισμήνη, την Ειρήνη και τον Τεό, που ήταν η αρχική σύνθεση της ομάδας όταν εντάχθηκα στο Garinis Lab. Με αγκάλιασαν στα πρώτα μου βήματα και έβαλαν τα πρώτα λιθαράκια στην εργαστηριακή μου ζωή. Επίσης, την κα Νίτσα, τη Μαρία, την Καλλίνα, το Νίκο και την Ουρανία για όλες τις ώρες (πολλές φορές περασμένες) που περάσαμε, τις ανησυχίες και τα άγχη που μοιραστήκαμε. Χάρη στην καλή διάθεση, το χιούμορ, τα γέλια και την αισιοδοξία τους έγινε η καθημερινότητα πιο εύκολη και οι πολύωρες αναμονές πιο ευχάριστες. Την Τζωρτζίνα και το Ζήση, που εκτός από τις ατελείωτες ώρες στο εργαστήριο, περάσαμε και αξέχαστες γιορτές Χριστουγέννων. Ιδιαίτερα όμως θα ήθελα να ευχαριστήσω το Ευάκι, που με τη σκληρή δουλειά και βοήθειά της (πρακτική και ψυχολογική) αυτή η δουλειά έχει τη σημερινή μορφή της. Πέρα από τις τεχνικές γνώσεις, μου έμαθε πολλά ως άνθρωπος, με το ήθος, την εργατικότητα και την υπομονή της. Θα είναι ένας άνθρωπος που θα θυμάμαι πάντα με θαυμασμό και

ευγνωμοσύνη. Εύη μου ειλικρινά σε ευχαριστώ! Ευχαριστώ επίσης και τα μέλη του Animal Facility του IMBB. Ειδικά την Ελένη και τη Νίκη για τα ατελείωτα breedings που ζητούσα, τα πολλά ποντικάκια που φρόντιζαν και την ευχάριστη νότα που έδιναν με το χιούμορ τους στα πολύωρα glucose tests.

Αφήνω για το τέλος τους δικούς μου ανθρώπους. Τους φίλους μου Ειρήνη, Κική και Πάνο, που έμειναν δίπλα μου από την άλλη άκρη της Ελλάδας, με υπομονή και κατανόηση για τις προτεραιότητες που κατά καιρούς έβαζα, ακόμη και όταν εγώ «εξαφανιζόμουν». Ένα μεγάλο ευχαριστώ και στις φίλες Μαρία, Χριστινιώ και Αγγελικάκι(Angel) μου, που ξεκινήσαμε μαζί και ήμασταν συνοδοιπόροι όλα αυτά τα 11 χρόνια. Δε θα ξεχάσω ποτέ τις ατελείωτες ώρες και τα ξενύχτια της εξεταστικής, τις κουβέντες που κάναμε, τα λόγια ενθάρρυνσης, παρηγοριάς και υποστήριξης που ανταλλάξαμε (πολλές φορές με τη συνοδεία ρακής). Τις ευχαριστώ για όλα και για κάθε φορά που πίστεψαν σε μένα, πολλές φορές περισσότερο από ότι πίστευα εγώ σε μένα. Όπως και την Γωγώ, που μας αγκάλιαζε και μας συμβούλευε ή μας έδινε ώθηση όταν μας έπιαναν οι γκρίνιες μας. Σας οφείλω πολλά και χαίρομαι για τη σχέση που έχουμε και είναι πολλά περισσότερα από απλή φιλία. Ελπίζω να σας έχω στη ζωή μου ακόμη και τώρα που οι δρόμοι μας χωρίζουν (ένα μεγάλο ευχαριστώ στην τεχνολογία και τα αεροπλάνα!). δε θα μπορούσα να ξεχάσω την κα Άννα και τον κ. Μανώλη, που μου στάθηκαν και τα 11 χρόνια ως δεύτερη οικογένεια.

Το μεγαλύτερο ευχαριστώ του κόσμου το χρωστάω στους ανθρώπους στους οποίους οφείλω το ότι έφτασα εδώ και όπου και αν καταφέρω να φτάσω. Στην οικογένειά μου. Μέσα από τον καθημερινό τους αγώνα και τις περισσότερες φορές σιωπηλά μου εξασφάλιζαν τα πάντα, ώστε να συγκεντρώνομαι και να αφοσιώνομαι στις σπουδές και σε αυτό που αγαπάω να κάνω, χωρίς άλλες έννοιες. Ευχαριστώ τη Χριστίνα, που με την αστείρευτη και ανιδιοτελή αγάπη που μας δίνει αποτελεί για μένα πρότυπο, ακόμη αν τέσταρα πολλές φορές τα όρια της υπομονής της. Τον μπαμπά μου, που ήταν και είναι πάντα δίπλα μου και πίσω μου, να με στηρίζει και να με ωθεί να προχωράω. Τον ευχαριστώ για όλα όσα κάνει και θυσιάζει για εμάς. Και ειδικά γιατί ομολογουμένως δεν ήμουν και το πιο εύκολο παιδί του κόσμου (Συγγνώμη μπαμπά!). το Νικολάκη, που με το χιούμορ του έκανε δύσκολες καταστάσεις πιο ευχάριστές και μου έφτιαχνε τη διάθεση. Ευχαριστώ και τον αδερφό μου Γιωργάκη (το μικρό μας). Και μόνο που υπάρχει, κάνει τη ζωή μου πιο όμορφη και αποτελεί για μένα μάθημα ζωής και πηγή δύναμης να εξελίσσομαι και να βελτιώνομαι, όχι επαγγελματικά, αλλά ως άνθρωπος. Ένα μεγάλο ευχαριστώ και στον αδερφό μου, Θάνο. Μπορεί να μη μιλάμε συχνά ή να μη λέμε πολλά, αλλά κάνουμε πολλά ο ένας για τον άλλο. Τον ευχαριστώ που είναι εκεί για μένα και ελπίζω να ξέρει ότι θα είμαι εκεί για εκείνον για ό,τι και αν χρειαστεί. Σε ευχαριστώ για τις κουβέντες που κάνουμε, για τις συμβουλές σου , αλλά και για τις στιγμές που μου την έλεγες (με το γάντι ή χωρίς), γιατί μου έδινες δύναμη. Μου έμαθες πολλά! Όλοι η οικογένειά μου μου μάθατε πολλά. Και θα προσπαθώ πάντα να σας δίνω λόγους να είστε περήφανοι για μένα. Σας ευχαριστώ που ομορφαίνετε τη ζωή μου και μου δίνετε δύναμη να συνεχίζω και να μην τα παρατάω.

# Table of contents

## Περίληψη

Ο μηχανισμός απόκρισης στις γενωμικές βλάβες, καθώς και αυτός της ανοσολογικής απόκρισης σχετίζονται με τη ρύθμιση του μεταβολισμού και την ανάπτυξη παθολογιών γήρανσης. Παρ' όλα αυτά, οι μοριακοί μηχανισμοί που μεσολαβούν αυτή τη σύνδεση δεν είναι γνωστοί. Αξιοποιώντας το γενετικό σύστημα Cre/LoxP, δημιουργήσαμε ένα μοντέλο ποντικού, που φέρει ιστοειδική απώλεια λειτουργίας της ενδονουκλεάσης ERCC1 στα μακροφάγα. Τα ποντίκια *Er*$^{F/-}$ αναπτύσσονται φυσιολογικά, αλλά παρουσιάζουν προοδευτικά μεταβολικές μεταβολές, όπως συσσώρευση γλυκογόνου στο ήπαρ και αυξημένη ανοχή στη γλυκόζη. Τα ευρήματα έδειξαν ότι, λόγω της έλλειψης της ERCC1 στα μακροφάγα, η συσσώρευση γενωμικών βλαβών επάγει κυτταροπλασματικές αποκρίσεις και αυξημένη βιοσύνθεση και έκκριση εξωκυττάριων κυστιδίων. Τα κυστίδια αυτά μεταφέρονται σε άλλα κύτταρα αποδέκτες, όπου μεταφέρουν το βιολογικό φορτίο τους και οδηγούν σε αυξημένα επίπεδα μεταφορέων γλυκόζης και σε συσσώρευση γλυκόζης. Τα υψηλά ενδοκυττάρια επίπεδα γλυκόζης ενεργοποιούν προ-φλεγμονώδεις αποκρίσεις, που βρέθηκαν να είναι ευαίσθητες στον αναστολέα του μονοπατιού mTOR, τη ραπαμυκίνη. Τα αποτελέσματα αυτά σηματοδοτούν τη συσχέτιση μεταξύ της απόκρισης σε γενετικές βλάβες, της μεταβολικής ρύθμισης και της χρόνιας, συστημικής φλεγμονής που παρατηρείται στα σύνδρομα προγηριάς NER.

## Abstract

DNA damage and Immune response are intimately linked with metabolism and the manifestation of age-related pathologies but the underlying mechanisms remain obscure. Using the Cre/LoxP system, we generated a mouse model carrying a defect in ERCC1, the obligatory partner of the structure-specific ERCC1-XPF endonuclease complex, in circulating macrophages. The *Er1*$^{F/-}$ mice develop normally, but progressively manifest metabolic alterations, including glycogen accumulation and increased tolerance to glucose. We found that accumulation of DNA damage in *Er1*$^{F/-}$ macrophages triggers various cytoplasmic stress responses and enhances the biogenesis and secretion of extracellular vesicles (EVs). These EVs are efficiently delivered to the recipient cells where they transfer their cargo, leading to glucose transporter upregulation and increased glucose uptake. In turn, high glucose activates pro-inflammatory signaling, in a rapamycin-sensitive manner, establishing a link between the DNA damage response (DDR), metabolic reprogramming and chronic, systemic inflammation in NER progeroid syndromes


**Key words:** DNA repair, Nucleotide excision repair, macrophages, inflammation, glucose, metabolism, extracellular vesicles, exosomes

# Introduction

Every multicellular organism is subject to hazardous environmental threats. To withstand them and to assure proper and coordinated function of the cells, defensive mechanisms have evolved to preserve the integrity and homeostatic balance of the organisms. Such mechanisms can be directed either inwards, to counteract macromolecular damage, or outwards, to protect the organism against infections and pathogens[1].

## DNA repair system

Every cell of a living organism is constantly exposed to damaging agents of exogenous (chemical compounds, solar irradiation) or endogenous (metabolic byproducts) origin that jeopardize the integrity and functionality of biological molecules. Out of all, DNA is the only biological molecule that cannot be replaced and solely relies on its repair in order to remain intact throughout lifespan and to be faithfully transmitted into progeny. Continuous and unavoidable damaging events occur on DNA, due to its inherent instability and vulnerability to chemical alterations, as well as due to extrinsic agents (UV, ionizing irradiation ) or physiological intrinsic functions (reactive oxygen species during respiration, mismatches during replication)[2]. Therefore, it is one of the biggest challenges for the cells to preserve their genome intact. For this reason, repair systems arose early in evolution and cells got equipped with a variety of sophisticated, specified and partially overlapping mechanisms, hierarchically structured to sense, signal and resolve each type of damage. Depending on the type of damage, the respective repair pathway is activated and the cells orchestrate the appropriate response[3]. DNA breaks are considered to be the most threatening DNA lesions for cell survival. For their repair, two principle pathways are utilized, depending on the stage of cell cycle. Homologous recombination (HR) occurs in late S-G2 phase, where the sister chromatid sequence is used as template for recombination and repair of the affected chromatid with high fidelity. The second mechanism, non-homologous end joining (NHEJ), is the predominant break repair pathway in G1 phase. Since there is no second DNA copy to be used as template, during NHEJ the two ends of the break are ligated in a quick, but error-prone manner[4]. Another highly cytotoxic type of lesions are interstrand crosslinks (ICLs), where the two DNA strands are covalently attached. The repair of these lesions is mediated by a combination of pathways, including HR, Fanconi's anemia proteins and Nucleotide excision repair (NER) machinery (see below)[5] . Insertions/deletion of repetitive sequences or mismatched nucleotides generated during replication are recognized and repaired by the highly conserved Mismatch repair pathway (MMR)[6]. Small chemical alterations, such as abasic sites and oxidized bases that can occur during cellular metabolism are dealt by the Base excision repair (BER) pathway[7], whereas helix distorting lesions, such as UV-induced cyclobutane pyrimidine dimers (CPDs) and 6-4 photoproducts (6-4PPs) are repaired by the Nucleotide excision repair (NER)[8]. After damage recognition by DNA damage sensors of the respective pathway, downstream signaling cascades are activated[9,10].

Improper or inefficient repair of the damage can lead to different outcomes, depending on various parameters, including the type and location of the damage, the phase of the cell cycle, the stage of differentiation etc.[3] . For example, some lesions, such as mismatched bases, are mainly mutagenic and contribute to carcinogenesis. On the other hand, cytotoxic or cytostatic lesions that alter DNA structure (e.g. bulky adducts, breaks), physically obstruct fundamental cellular processes (DNA replication and transcription) and lead to cell death[11]. At the organismal level, mutations in DNA repair factors are linked to congenital syndromes, termed genome instability syndromes, with various clinical manifestations, including cancer, developmental defects and ageing[2,12].

**Immune system**

All organisms live in an environment of potential threats, including toxic substances and pathogenic microbes. For this reason, they need caretaking systems that can eliminate and protect them from such threats. From early on in evolution, cells got equipped with protective mechanisms. Even unicellular organisms possess strategies to eliminate pathogenic factors, such as restriction endonucleases, antimicrobial peptides and RNA interference[13]. Transition to multicellularity was accompanied by the evolution of specialized cells and mechanisms with discrimination of “self” and “non-self” being their central characteristic. This self-surveillance system is known as innate immunity and it is a defensive system highly conserved in plants, invertebrates and mammals. It involves a number of different cell types, all originating from a common myeloid progenitor (CML)[14] and each designated with specialized functions. These include granulocytes (neutrophils, eosinophils), macrophages and dendritic cells (DCs). Neutrophils, which are terminally-differentiated, non-replicating phagocytic cells have antimicrobial functions and play a role in clearance of pathogenic microbes and resolution of inflammation[15]. Eosinophils have a prominent role in most allergic reactions, macrophages are the main phagocytic innate immune cells, while DCs are the main antigen-presenting cells (APCs) of the innate immune system[16]. Apart from protection from pathogens, innate immunity has a crucial role in homeostatic maintenance of multicellular organisms. Thus, in addition to “non-self”, removal of altered “self”, e.g. elimination of damaged, stressed and cancerous host cells, is another key responsibility of innate immune system. This is accomplished by germline-encoded receptors, termed Pattern Recognition Receptors (PRRs) which recognize either Pathogen-Associated Molecular Patterns. (PAMPs) or Damage-Associated Molecular Patterns (DAMPs). PAMPs include highly conserved features of pathogens, that are essential for their survival and pathogenicity and are absent in the host. DAMPs, on the other hand, include host components in abnormal form or location and serve as messengers of stressed or damaged “self” and mediate an immune response that eliminates the targeted dysfunctional cells, so as to maintain the integrity of the whole tissue or organism[17]. The 1$^{st}$ PRR class identified was the TLR family. TLRs can be either localized on the cell surface or associated with endocytic vesicles. At least 10 TLRs have been identified, with each being characterized by

specificity for a type of PAMP or DAMP. The continuous adaptation and the increasing heterogeneity of viruses and pathogens necessitated the emergence of a more diverse and specified system for the efficient protection of the organisms. This system, known as adaptive immune system arose in jaw vertebrates, not to replace but to complement innate immune system. Innate and adaptive immune system form a multilayered, hierarchical network where each system acts both autonomously and in synergy with one another[13]. The main discriminations between the two systems include the immense variety and specificity of the adaptive cells' receptors, as well as the immunological memory offered by those cells. Adaptive immune system is comprised of cells originating from a common lymphoid progenitor that is differentiated into T, B and natural killer (NK) cells. With the exception of NK cells, which are responsible for killing of virally infected or cancerous cells without any prior activation, or priming from antigen presenting cells, T and B cells express individual receptors that arose from random genetic rearrangements of the variable (V) /diversity (D)/ joining (J) loci, through a process known as V(D)J recombination. In B cells, the antibody-producing cells of the immune system, further diversification is achieved after somatic hypermutation and class-switch recombination[18]. In contrast to innate, adaptive system takes place in the late phase of infection after the Antigen Presenting Cells (APCs) have engulfed, processed and presented the invading pathogens' antigens (Ags) to adaptive immune cells. An optimal adaptive immune response, involves activation of naïve cells, proliferation and clonal expansion of the cells with the specific receptor against the invading antigen and contraction, which includes apoptotic death of most of the effector cells after successful elimination of the pathogen. At the end, after resolution of the immune response, some cells remain to provide immune memory[19].

Overall, DNA damage response and immune responses are surveillance systems responsible for protection, maintenance and preservation of proper cellular and tissue function. They are both characterized by high complexity, hierarchical structure and interplay between their sub-pathways. Thus, tight (auto) regulation of these responses is crucial for cellular and organismal survival, since their beneficial role could turn into detrimental threat if the responses are prolonged or uncontrolled. Indeed, deregulation of any of these responses have been linked to various pathogenic conditions. Inherited defects in immune system give rise to heterogenous disorders, including immunodeficiencies, malignancy, increased susceptibility to infections, autoimmune and chronic inflammatory diseases[20]**.** Likewise, inborn mutations in genes of DNA repair proteins have been associated with complex hereditary syndromes, namely genome instability syndromes[11,21]**.** The importance of the genome maintenance pathways is illustrated by the complex, wide variety of phenotypes that rise due to defects in DNA repair and signaling proteins[22,23]. Depending on the different type of damage, the protein and the pathway affected, the pathologies can range from cancer to developmental impairment and accelerated ageing[24]. For example, mutations in repair pathways protecting from mutagenic lesions, lead to increased cancer susceptibility, while the other

hand, inherited defects in proteins that repair cytotoxic damage (e.g. replication, transcription blocking lesions) give rise to developmental abnormalities and accelerated ageing phenotypes, including neurodegeneration, cachexia, hematopoietic stem cell exhaustion etc.[3].

**DNA damage and immune response interplay**

DNA damage response (DDR) and immune response are both protective mechanisms, evolved together to accomplish the homeostatic maintenance of multicellular organisms throughout lifespan. The notion of interplay between them came early on by the fact that viral DNA integration into host genome involves generation of DSBs and arousal of DDR, as well as by the involvement of repair pathways during normal development of lymphocytes[25]. Recent evidence extend this communication to a functional, reciprocal crosstalk, with DNA damage and subsequent DDR inducing immune signaling and chronic inflammation and vice versa[26]. During normal lymphocyte development, T and B cells undergo somatic rearrangements of the Ig and TCR loci, a process called V(D)J recombination. This process is essential for proper lymphocyte function and provides the cells with an unlimited number of different receptors, through random rearrangements of the V, D and J fragments, after the generation of DSBs[27]. These “programmed” breaks are initiated by the RAG endonuclease during G1 phase and lead to activation of kinases that orchestrate downstream effectors of DDR, so as to process and repair the damage through NHEJ repair process[28]. Two of the key kinases mediating DDR signaling, ATM and DNA-PK, have been shown to be induced after RAG DSBs and to have both distinct and overlapping roles in coordination of the DDR during V(D)J recombination[29]. For example, DNA-PK is essential for the activation of Artemis endonuclease and the subsequent processing of the hairpin intermediates[30,31]. On the other hand, ATM has been shown to activate transcriptional programs regulating not only the classical DDR, but also proper lymphocyte development[32]. In addition, ATM has an essential role in allelic exclusion and inhibits further Ag receptor loci rearrangements of the other allele[33]. In B cells that have undergone V(D)J recombination, two additional AG receptor diversification steps take place: Class-Switch Recombination (CSR), where Ig region is rearranged leading B cells to alter antibody isotype and effector functions and Somatic Hyper-Mutation (SHM) which leads to increased affinity of a stimulated antibody for a specific antigen, through induction of mutations in the variable region of the antibody[34].

Both of these processes are activated by activation-induced cytidine deaminase (AID) which converts cytidines to uracils thus creating U:G mismatches in antigen activated B cells. These “programmed” mutations are sensed and processed by two DNA repair pathways, BER and MMR.. More specifically, the modified bases are recognized and excised by a BER glycosylase Uracil-DNA glycosylase (UNG), or alternatively, MMR proteins sense the U:G mismatch and the gap formed after the excision is filled by low fidelity translesion synthesis (TLS) polymerases, contributing to mutagenesis-

mediated diversity of the receptor. Thus, BER and MMR are considered to act in parallel and in coordination to repair AID-induced base alterations[35,36].
During the excision of the U bases, Single-Strand Breaks (SSBs) arise that can act as precursors of DSBs. These lesions, instead of mutations, result in genetic rearrangements that contribute to CSR and have been shown to be dependent on both BER and MMR[37]. The importance of DNA repair mechanisms in regulation of proper immune system development is seen in a variety of disorders with defective adaptive immunity function, leukemias and lymphomas that result from mutations in DNA damage repair and signaling genes[27]. Such cases include, for example, mutations in either one of the central kinases ATM and DNA-PK. Defect in DNA-PK activity is associated with severe combined immunodeficiency (SCID), while mutations in ATM leads to Ataxia Telangiectasia (AT) syndrome, which among other phenotypes, is characterized by immunodeficiency, lymphopenia and predisposition for lymphoid malignancies[38].

Another aspect of immune response that led to its functional association with DDR is the fact that genomic integration and lytic replication involve the generation of DSBs. In addition, viral infection was correlated with increased chromosomal aberrations (breaks, translocations) and also, viruses depend on DNA metabolism processes of the host cell to replicate their genome. Thus, it could be hypothesized that the DDR provoked by the viral infected cells could mediate an inflammatory response to eliminate the virus or could be actively induced by viruses themselves at their advantage[39]. There have been many functional interactions between the two surveillance systems identified and is now clear that they both have active regulatory roles in one another.

It has been noticed that DDR factors can be part of the signaling cascades during innate immune responses. It has been shown that DDR is activated upon bacterial infection downstream of Toll-like Receptors (TLR) and type I IFN. More specifically, ATM and DNA-PK were found to regulate transcriptional programs and inflammasome function of activated macrophages[40]. Conversely, DNA damage has the potential to trigger immune signaling pathways. For example, DNA damage, either exogenous or due to ATM deficiency, results in enhanced IFN production and an amplified anti-microbial innate immune response[41]. IRF3, a transcriptional factor with central role in antiviral responses, can be induced by DNA damaging agents, such as mitomycin C and UV irradiation[42]. DNA-PK was shown to phosphorylate, activate and prevent degradation of IRF3 in response to viral infections[43]. Other DDR factors have been also implicated in the regulation of immune responses. BRCA1, a key factor of genome maintenance pathways, forms a complex with IFI16 and stabilizes the IFI16-inflammasome complex. IFI16 is a nuclear innate sensor of viral dsDNA that is associated with induction of IFN-β production. Thus, BRCA1 was shown to have immunomodulatory role by facilitating sensing of viral DNA and the downstream antiviral response[44]. One of the core HR repair proteins, Rad51 is essential for replication stress resolution and was recently found to regulate innate immune response. Irradiated Rad51-deficient cells accumulate

cytosolic DNA fragments and activate STING-TBK1 dependent immune genes upregulation[45].

Several DDR factors are now considered as critical mediators of inflammatory responses. Multiple studies have highlighted their role in expression of several immune-related transcription factors, cell surface ligands and adhesion molecules[46].

PARP1 is a multifactorial protein with diverse functions, including regulation of chromatin structure, transcription, cell cycle control and genome maintenance. Studies have shown that PARP1 participates in inflammatory gene expression by both directly interacting with NFκB and by facilitating NFκB nuclear translocation[47]. Recently, a new link between oxidative damage and immune response was described. PD-L1, a negative regulator of adaptive immunity, was shown to be upregulated upon oxidative stress or in the absence of key BER glycosylases in cancer cells. This upregulation was dependent on ATR/Chk1 signaling, highlighting a role of DDR in the regulation of adaptive immune response in cancer[48].

In addition, one of the main BER glycosylase, OGG1 has been functionally linked to immune response, by regulating cytokine and chemokine production. Absence of OGG1 results in decreased levels and activation of key transcription factors, such as STAT6 and NFκB, as well as hampered production of cytokines and chemokines[49,50]. APE1, another BER glycosylase, has also been linked to TLR2-mediated inflammatory responses[51].

NFκB is a master transcriptional regulator of both innate and adaptive immune genes, as well as coordinator of cell death and survival transcriptional programs during inflammation. NFκB is activated in response to various extracellular stimuli, including proinflammatory cytokines and PAMPs. DNA damage has been identified as a stress stimuli activating NFκB and this activation is mediated by ATM[26]. In the presence of DSBs, ATM, except for damage sensor and DDR mediator, has an active role in NFκB signaling pathway by both phosphorylating NEMO in the nucleolus and by participating in the mono-ubiquitination of NEMO in the cytoplasm. NEMO mono-ubiquitination by ATM has also been shown to be triggered by IL1b and TNFa and in the absence of damage. Thus, it is proposed that ATM has additional roles in immune signaling outside and independent of DDR. ATM has also been reported to downregulate proinflammatory cytokines. The oxidative burst during inflammation and ROS production could be the trigger for ATM activation, a mechanism used by neutrophils to resolve the inflammation. Additionally, ATM participates as a negative regulator of TLR4-activated transcriptional program for a subset of inflammatory genes[52]. An additional role attributed to the ATM and ATR kinases in the induction of innate immune response, is the upregulation of NKG2D ligands expression. NKG2D is an innate immune receptor, crucial for NK-mediated cytotoxicity and the removal of cancer and infected cells[53].

## Immune DNA sensing

Innate immune system rapidly recognizes and responds to invading threats by utilizing germline-encoded pattern recognition receptors (PRRs). These receptors are able to detect either microbial products (pathogen-associated molecular patterns, PAMPs) or self-components that are mislocalized or released from damaged and dying cells (damage-associated molecular patterns, DAMPs). Regarding nucleic acid recognition, Specified TLRs can recognize different nucleic acid structures. For example, TLR3 recognizes dsRNA formed after replication of positive-stranded RNA viruses, TLR7 and 8 ssRNA and TLR9 bacterial unmethylated CpG DNA[54]. In mammalian cells, DNA is localized and restricted in the nucleus. Leakage of host DNA or invasion of foreign DNA in the cytoplasm is perceived as a danger signal and leads to its recognition by certain types of PRRs and the induction of inflammatory responses.

Even in normal conditions, nuclear DNA fragments are exported in the cytoplasm and this is exacerbated under stressful conditions, such as excessive DNA damage. To avoid oversupply of the cytoplasm with nucleic acids, cells employ several nucleases that detect and degrade mislocalized DNA or RNA fragments, such as TREX1, RNase H2 and DNase II. Defective nucleic acid degradation and accumulation beyond immunostimulatory threshold results in cGAS-STING pathway activation and to the manifestation of autoimmune diseases[55].

Apart from endosomal TLR-dependent nucleic acid recognition, cytosolic nucleic acid sensing pathways have been characterized. DNA-dependent activator of IFN-regulatory factors (DAI), the first reported cytosolic dsDNA sensor, Interferon-γ-inducible protein16 (IFI16), DExD/H- box helicase 41 (DDX41) and cGMP–AMP synthase (cGAS) have been shown to bind to dsDNA and regulate type I IFN response, through activation of the STING-TBK1-IRF3 signaling pathway[56]. Absent in melanoma 2 (AIM2) is another cytosolic DNA receptor that, in contrast to the aforementioned, activates the ASC/Caspase I inflammasome pathway and the production of IL18 and IL1b proinflammatory cytokines[57]. Finally, another cytoplasmic DNA sensor is RNA pol III, an enzyme responsible for the transcription of 5S rRNA and tRNA. RNA pol III, was found to bind AT-rich dsDNA fragments and convert them into dsRNA, which then acts as RIG-1 ligand leading to type I IFN responses[58]. Cytoplasmic dsRNA can be detected in the cytoplasm by two RIG-I-like receptors (RLRs), RIG-I and MDA5, with RIG-I recognizing short and MDA5 longer RNA species, leading to interferon signaling through MAVS[59].

Over the last decade, several proteins, including central DNA damage sensors, have been identified as cytoplasmic DNA sensors. The first such report was in 2011, when Ku70, a protein involved in NHEJ, was identified as a cytosolic PRR that recognizes cytoplasmic DNA and induces type III IFN responses[60]. The protein complex DNA-PK was a year later found in the cytoplasm, where it detected DNA and triggered IRF-3 dependent type I IFN response[61]. The DNA

damage sensor MRE11 was detected in the cytoplasm, where it acts as cytoplasmic dsDNA sensor, but not of viral DNA, and induces STING-TBK1-IRF3 axis to stimulate responses to damaged host cell[62]. More recently, a new role for Rad50 as cytoplasmic DNA receptor. Upon DNA presence in the cytoplasm, Rad50 was found bound to it, together with Mre11, Nbs1 and the immune adapter CARD9 and resulted in NFκB-depented Il1b production[63].

**Nucleotide excision repair (NER)**

Nucleotide excision repair pathway is a highly conserved, multistep repair mechanism. It involves over 30 proteins which act in a “cut-and-patch” mode. One of the unique characteristics of this pathway is the most versatile range of helix distorting lesions it detects, including UV-induced cyclobutane–pyrimidine dimers (CPDs) and 6–4 pyrimidine–pyrimidone photoproducts (6–4PPs), bulky adducts, intrastrand crosslinks and ROS-generated cyclopurines[64]. During the recognition step, NER is divided in two sub pathways, named global genome NER (GG-NER) and transcription-coupled NER (TC-NER). GG-NER scans and detects lesions throughout the genome, while TC-NER probes the transcribed strand for RNA pol II-blocking lesions. In the case of GG-NER, damage recognition is performed by the UV-DDB complex and XPC. XPC, together with RAD23B and CETN2 have high affinity for the ss-ds DNA junctions of unpaired DNA and bind on the undamaged strand. UV-DDB complex comprises of the DDB1 and DDB2 proteins and binds to UV-induced lesions, creating unpaired bases that act as substrate for XPC[65]. The second NER sub-pathway is devoted to recognition of lesions blocking transcription, since stalled transcription is highly cytotoxic, threatening the cells with cell cycle arrest and apoptosis. The recognition step of TC-NER is coupled to transcription elongation and initiated upon arrested RNA pol II, setting the recognition of even subtle DNA structure alterations more efficient. Once stalled, RNA pol II associates with Cockayne syndrome B and A proteins (CSB and CSA, respectively) and this association renders the lesion accessible and facilitates the recruitment of other TC-NER factors, such as UV-stimulated scaffold protein A (UVSSA), ubiquitin-specific-processing protease 7 (USP7), XPA-binding protein 2 (XAB2) and high mobility group nucleosome-binding domain-containing protein 1 (HMGN1), as well as the downstream core NER factors[66]. After damage recognition, the two sub-pathways merge into a common cascade of reactions with the key steps being the formation of the pre-incision complex, unwinding of a ~25-30bp DNA stretch, excision of the ssDNA stretch around the lesion, filling of the gap with the opposite strand as template and finally the ligation of the newly synthesized DNA. More specifically, the multi-subunit transcription factor II H (TFIIH), with the assistance of XPA, verifies the lesion and, through its helicase subunits XPB and XPD, unwinds the DNA around the lesion[67]. Subsequently, incision and excision of the damaged strand is conducted by XPG and ERCC1-XPF structure-specific endonucleases at 3’ and 5’ site, respectively. XPG recruitment precedes that of ERCC1-XPF, although the 5’ incision is sufficient to initiate the re-synthesis of the excised fragment even prior to the 3’ incision, generating a single-strand gap, which is protected by RPA. Finally, gap filling

and ligation are executed by DNA Pol δ, DNA Pol ε or DNA Pol κ, and DNA ligase 1 or XRCC1– DNA ligase 3[68] , depending on the proliferative status off the cells, (**Figure 1**). Many NER factors have been attributed with additional roles, beyond that of repair.

XPG has been found to interact with WRN protein in S phase of cell cycle, possibly to resolve replication fork collapse due to DNA damage[69]. In addition, interaction of XPG with glycosylases have been reported, suggesting a role of XPG in removal of oxidized bases[70]. TFIIH, a core NER factor, is also a central regulator of RNA pol II-dependent transcription, being component of the pre-initiation complex. Through its CAK subunit, it is also involved in cell cycle regulation[71]. Additionally to TFIIH, other NER factors, such as XPC, CSB, XPA, RPA, XPG and ERCC1-XPF have been found to be recruited on promoters[72]. XPC was also found as part of a stem cell coactivator complex (SCC), regulating pluripotency of stem cells. Another role of NER factors in transcription regulation is the induction of transcription-associated DSBs, which arise during resolution of supercoiling ahead of and behind RNA pol II. Nascent RNAs can hybridize with DNA, both under normal conditions and upon stalling of RNA pol II. CSB, XPG and ERCC1-XPF have been shown to be involved in the processing of such structures[73]. Regulation of gene expression by NER factors can be accomplished through modulation of chromatin architecture and looping. More specifically, XPG and XPF are crucial for the recruitment of CCCTC-binding factor CTCF, a protein involved in transcription regulation, chromatin architecture and genomic imprinting[74]. CTCF also interacts with ERCC1-XPF during postnatal silencing of imprinted genes[75] and with CSB upon oxidative stress[76].

ERCC1/XPF endonuclease has been attributed with multiple roles beyond NER, due to its capacity to process 3' overhangs. The complex has been found to be involved in the repair of inter-strand crosslinks (ICLs)[77]. Furthermore, it has a role in DSB repair, by removing 3' non-homologous ends. Similarly, it can remove modified 3' ends, as a backup mechanism, during BER. Finally, ERCC1-XPF is implicated in telomere maintenance and processing, since it can cleave 3' uncapped telomeres[78].

CSB has been implicated in regulation of DSB repair and cell cycle checkpoint activation[79].It has been shown to have additional role in BER, being important for the efficient incision and repair of 8-oxoG. It also interacts with BER related proteins, such as PARP-1 and APE1[80]. In a recent study, the function of CSB in BER was examined and it was found that CSB is recruited to 8-oxoG oxidative lesions and induces subsequent XRCC1 recruitment lesions to coordinate the downstream repair process[81]. Finally, XPC has also been implicated to have a function during BER[82].

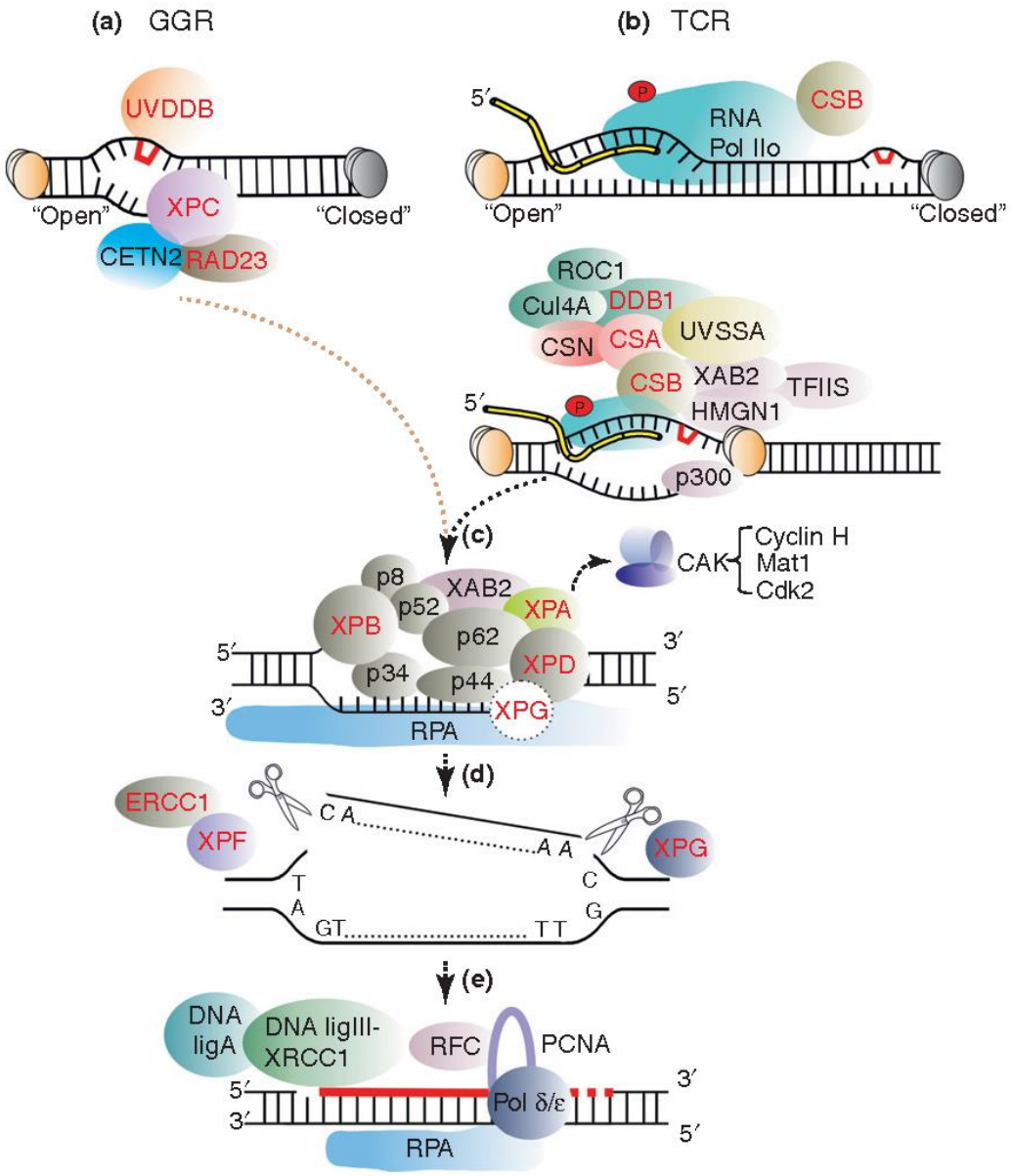


**Figure 1. The Nucleotide Excision Repair (NER) Pathway.** Helix-distorting lesions are detected by NER pathway via distinct mechanisms. The Global Genome NER (GG-NER) scans and detects lesions throughout the genome, while Transcription-Coupled NER (TC-NER) recognizes similar lesions selectively on the transcribed strand. Following the damage recognition step, the two sub-pathways merge into one common mechanism that involves the unwinding of the double helix around the damage, excision of the lesion-containing DNA fragment, filling of the gap and ligation of the newly synthesized DNA (Adapted from [83]).

## NER syndromes

Due to the high variability of the lesions detected and the multiple roles of NER proteins, inborn mutations of NER genes are associated with an extremely broad and highly diverse range of clinical consequences. Even mutations in the same gene can give rise to heterogeneous phenotypes that range from normal development with cancer predisposition to neurodevelopmental disorders and accelerated ageing, with UV sensitivity being a common trait in both cases. Thus, NER syndromes are characterized by both genetic pleiotropy and genetic heterogeneity[73]. There are three main syndromes that rise from mutations of NER genes, xeroderma pigmentosum (XP), Cockayne syndrome (CS) and Trichothiodystrophy (TTD). Depending on the NER sub-pathway affected, the clinical manifestations can vary dramatically and even be diametrically opposed. In patients with defective GG-NER, increased cancer susceptibility is reported, while those with mutations in TC-NER genes develop severe premature ageing phenotypes with no cancer predisposition.

Most of NER patients are reported to suffer from Xeroderma Pigmentosum (XP). XP originates from mutations in *XPA-XPG* genes and in the XP variant (*XPV*) gene, which encodes DNA polymerase eta, responsible for translesion synthesis, although distinct mutations give rise to different clinical outcomes. The common traits of all XP patients are pigmentation abnormalities, exquisite sun sensitivity and over 1000-fold increase of sun-induced skin cancer[23]. The clinical features can vary between each case though, depending on the complementation group that is mutated, the NER sub-pathway affected and the nature of the mutation. XPC and XPE are the only XP proteins required exclusively for GG-NER. Patients harbouring mutations in these two genes exhibit mild hypersensitivity to UV radiation, hypo- or hyper-pigmentation and have the highest cancer incidence among all XP groups[64]. Mutations in the rest of *XP* genes impact both branches of NER and manifest additional symptoms. For example, ~20% of XP patients develop neurological abnormalities and neurodegeneration. XPA patients fall also into this category and develop a severe form of XP, namely the De Sanctis-Cacchione Syndrome[84]. On the other hand, mutations in genes that compromise TC-NER are characterized by complex pathologies including mental retardation, growth defects and premature ageing. Those segmental progeria syndromes are Cockayne Syndrome (CS) and Trichothiodystrophy (TTD), which are mainly the result of mutations in CSB/CSA and TTDA genes. Most CS patients are characterized by short stature, growth impairment, mental retardation and accelerated ageing manifestations[23]. Again, the genotype-phenotype correlation can be very complicated, with different mutations resulting in a broad spectrum of symptoms. 78 different mutations of *CSB* have been reported with various clinical outcomes, while around 30 of *CSA*, which give rise to milder CS forms[85]. Depending on the clinical severity, CS is classified into three types: CS type I, which is the classical form of CS, CS type II, the most severe form of CS, also known as Cerebro-Oculo-Facio-Skeletal Syndrome (COFS), with the abnormalities being exerted even before birth, and CS type III, the milder, late

onset form, such as UVsS syndrome, which is not accompanied by neurodevelopmental abnormalities[86]. TTD's main features include sulfur deficient brittle hair, accompanied by common traits with CS. Apart from *TTDA*, it can result from mutations in *XPB* and *XPD* mutations as well[87].

To add more to the complexity, mutations of NER factors that are engaged to both branches of NER can lead to markedly different outcomes. For example, mutated XPB, XPD TFIIH subunits and XPG endonuclease result in the manifestation of a combined XP/CS phenotype, with co-existence of the XP skin abnormalities and the neurodevelopmental retardation of CS[88]. The fact that *XPB* and *XPD* mutations have been associated with the pathogenesis of all XP, CS and TTD syndromes as well as with combined XP/TTD, result from their dual role in NER and transcription[89]. While mutations in *XPG* nuclease domain give rise to XP, mutations that result in C-term truncation and/or loss of interaction with TFIIH result in combined XP/CS and even the most severe form of CS, COFS with the patients manifesting growth failure, progressive neurodevelopmental abnormalities and decreased lifespan[90]. COFS can also arise from mutations of the other NER endonuclease, ERCC1[91].

ERCC1-XPF endonuclease defects can lead to a constellation of clinical outcomes, underscoring its multifunctionality[92]. Most of *XPF* mutations present mild XP phenotypes, including UV sensitivity and skin freckling. Nevertheless, other mutations can lead to much more severe outcomes, for example XP/CS, with additional neurological symptoms[92], as well as combination of XP, CS and Fanconi Anemia (FA) features[93]. Another case of severe outcome due to *XPF* mutations is the distinct segmental progeria syndrome XFE, which is characterized, in addition to XP symptoms, by dwarfism, cachexia, microcephaly and accelerated ageing traits[11]. *ERCC1* mutations have identified in diagnosed case of COFS, with severe pre- and post-natal developmental defects, rapid neurological decline and severe post-natal growth failure[94]. CS type I and II patients have been reported with mutations in *ERCC1* and *XPF* genes, while they carried no alterations in *CSA* or *CSB* genes[93]. Finally, two patients diagnosed with FA were found to carry biallelic mutations in *XPF* gene, that abrogated XPF activity in ICL repair[95].

**NER mouse models**

Overall, it is clear that the complexity of NER mechanism (by means of the nature of the damage recognized, the sub-pathways and the multi-functionality of the proteins it comprises of) can be reflected on the complexity of the clinical outcomes and the outcome of its compromised function. The physiological consequences can vary from cancer (in the case of GG-NER defects, which primarily protects from potential mutagenic lesions) to developmental abnormalities and premature ageing (when TC-NER is not able to repair cytotoxic, transcription-blocking lesions). To uncover the mechanisms underlying the relationship of NER with those two extremes, mouse models with inborn defects in various NER factors have been generated. These models are a valuable tool in drawing links between certain gene mutations and the

consequent pathologies, as well as in gaining insight into the complex genotype- phenotype correlations.

Generation of *Xpc*$^{-/-}$ mice was conducted by two independent groups and in both cases, absence of XPC led to a phenotype very similar to that of XP-C patients, with marked UV sensitivity[96,97]. A CS mouse model was generated by mimicking the *CSB* gene truncation found in CS-B patient. These mice developed a much milder phenotype than this of the CS patients and, in contrast to human CS, the mice showed increased susceptibility to skin cancer[98]. Likewise, knocking out *Csa* in mice leads to mild CS phenotype, with elevated UV sensitivity, but no developmental or neurological abnormalities. Again, like *Csb*$^{m/m}$, *Csa*$^{-/-}$ mice had higher risk in UV-induced skin cancer development (Csa mice). *Xpa*$^{-/-}$ mice also display much milder phenotype than XPA patients, with no obvious neuropathologies being manifested[99]. Mice carrying mutations in TFIIH subunits *Xpb*, *Xpd*, *Ttda* genes recapitulate the human clinical diversity, developing XP, TTD, XP-CS or XP-TTD phenotypes. More specifically, *Xpd*$^{TTD}$ mice, which carry the same mutation found in TTD patients, develop the CS-like phenotypes and progeroid symptoms as their human counterparts. Further abrogation of NER activity by crossing these mice with the NER defective *Xpa*$^{-/-}$ mice accelerates the TTD pathology and shortens lifespan to approximately 3 weeks[100]. *Xpd*$^{XPCS}$ mice genocopy XP-CS patient, showing extremely elevated UV-induced skin cancer susceptibility. Similar to *Xpd*$^{TTD}$, crossing *Xpd*$^{XPCS}$ mice with *Xpa*$^{-/-}$ mice worsened the phenotype and lifespan expectance of the mice[101]. This is also the case for *Xpb*$^{XPCS}$/ *Xpa*$^{-/-}$ mice[102], *Csa*$^{-/-}$/ *Xpc*$^{-/-}$, *Csb*$^{m/m}$/ *Xpa*$^{-/-}$ and *Csb*$^{m/m}$/ *Xpc*$^{-/-}$ mice[89,90], highlighting the synergistic effect of simultaneous GG- and TC-NER defect. On the other hand, deletion of *Xpg* alone is sufficient to reproduce the phenotype of the above double mutants and develop the severe XP/CS phenotypes, including growth deficiency, progeroid features and shortened lifespan, while mice with point mutations in this gene resemble the phenotype of XP, showing severe UV-sensitivity, but unaffected lifespan[90]. The severe pathologies due to single mutations is also the case for the other endonucleases of NER, ERCC1 and XPF. *Xpf* mutant mice, generated by introduction of the same frameshift mutation (that leads to the generation of a premature stop codon) found in XPF patient, results in developmental delay, ageing phenotypes and reduced lifespan (up to 3 weeks)[103]. Deletion of *Ercc1* gene in mice results in severe multisystem degeneration and, almost identical to *Xpf*$^{-/-}$ mice, developmental and progeroid phenotypes and diminished lifespan, phenocopying the respective human condition with COFS and XFE[104], establishing this mouse model as a powerful tool in delineating the importance of genomic stability in development and the ageing process. However, due to the aggression and rapid progression of the pathology, together with limited lifespan of these mice, the use of strains with reduced levels of ERCC1, as well as conditional and tissue-specific knock-out strains has been of great importance in pursue of this knowledge. One such case is the hypomorphic *Ercc1*$^{\Delta/-}$ strain, which carries C-term truncated ERCC1 and recapitulates *Ercc1*$^{-/-}$ phenotype, but with a lifespan up to 6 months of age[105].

To shed light on the molecular connections between genome maintenance, development and longevity, progeroid mice were used in microarray transcriptional assays, where liver expression profiles were compared to those of mice with no accelerated ageing and of naturally aged mice. It was found that, in contrast to littermate controls, *Ercc1*$^{-/-}$ mice showed altered hormonal and metabolic patterns, including attenuated somatotroph axis, dampened oxidative metabolism and glycolysis, while upregulated glycogen and fatty acid synthesis pathways and pro-apoptotic gene expression[104]. These patterns of the growth hormone, carbohydrate and oxidative metabolism axes were also found in naturally aged mice, whereas the anti-oxidant responses were upregulated only in the short-lived NER and not in aged mice. In addition, the same alterations were observed in other NER progeria mouse models, such as *Csb*$^{m/m}$/ *Xpa*$^{-/-}$ and *Xpd*$^{TTD}$/*Xpa*$^{-/-}$ [106]. Interestingly, similar hormonal shifts and suppression of the somatotroph axis is also observed in long-lived mouse strains and calorie-restricted mice[107], leading to the proposal of the "survival response", where resources are shifted to maintenance at the expence of growth. It is known that during development, GH/IGF1 axis mitogenic effects promote oxidative metabolism required for growth and thus the production of free radicals. NER mice, which gradually accumulate DNA lesions due to their inherent defect, in an attempt to relieve the stress caused by these radicals on the genome, initiate an adaptive response by dampening the growth promoting GH/IGF1 axis. While this could be beneficial if the damage could be repaired, in the case of NER mice leads to arrested growth and eventually to developmental delay and accelerated ageing. Thus, NER mice are characterized by a reallocation of systemic responses from growth to somatic preservation and maintenance, which, in addition to the premature ageing, could act as a tumor-suppressive mechanism and explain the absence of cancer incidences in NER progeria.

Although these expression changes were shown to be the result of accumulating transcription-blocking lesions and therefore cell autonomous[108], they still cannot fully explain the complexity of the ageing phenotypes. Indeed, it is now evident that DNA damage and persistent DDR signaling trigger extensive systemic responses that gradually end up in tissue dysfunction, deterioration and ageing.

**DNA damage and inflammation: systemic responses and role in ageing**

Ageing is associated with a decline of cellular function. Immune cells gradually lose their ability to properly regulate the balance between pro- and anti-inflammatory responses and become "immuunosenescent", leading to persistent, low-grade inflammation, a phenomenon termed "inflammageing"[109]. At the same time, besides immune cells, non-immune cells accumulate damage, together with a reduction in repair capacity that comes with ageing. Under such stressful conditions, cells cease to divide, enter a state of permanent and irreversible cell cycle arrest and become senescent[110]. These senescent cells adopt a discrete phenotype, named SASP (Senescence-Associated Secretory Phenotype), which is characterized by secretion of a

battery of immune-related factors (e.g. cytokines and chemokines), extracellular matrix remodeling enzymes, cell surface proteins and growth factors[111]. Thus, damaged or stressed cells can alter their microenvironment and trigger an inflammatory response. This is a beneficial response, with a tumor-suppressive role, protecting from uncontrolled cellular proliferation and cancer. Nevertheless, increased senescent cell burden, long term SASP activation and persisting inflammation result in adverse effects.

One of the drivers of SASP is DNA damage and persistent DDR signaling. The immune response elicited by DNA damage-induced SASP reflects cellular attempt to eliminate the malfunctioning cells. However, failure to resolve this response and its long term activation (for example, due to accumulation of unrepaired damage and/or hyperactivation of the immune response) results in chronic inflammation, tissue degeneration and manifestation of age-associated pathologies[1] (**Figure 2**). Studies in DNA repair deficient progeroid mice lead to the formation of a link between DNA damage, chronic inflammation and age-related degenerative diseases. Additionally, mice with inborn defects in immune response-associated factors also show altered rates of ageing[112,113].

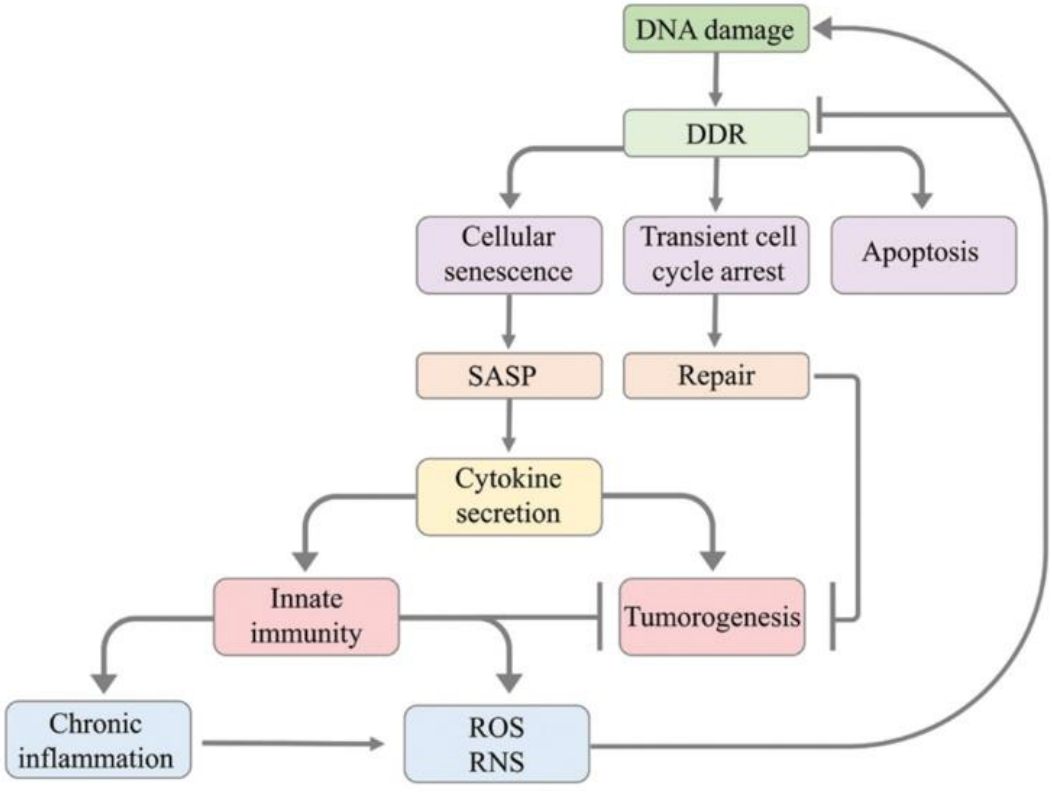


**Figure 2. The Innate immune and DNA damage response crosstalk.** DNA damage and the subsequent activation of DNA damage response (DDR) lead to apoptosis or cell cycle arrest, so as to allow for efficient repair and protect from tumorigenesis. In the case of unrepaired or accumulating damage, the result is permanent cell cycle arrest and senescence. Senescent cells adopt a distinct phenotype and affect their tissue environment by secreting various factors, including proinflammatory cytokines, a phenomenon termed senescence-associated secretory phenotype (SASP). The

activation of innate immune cells is a protective mechanism, by eliminating damaged cells and preventing tumorigenesis. Sustained immune activation can lead to adverse effects, including chronic inflammation, which is also accompanied by the production of reactive oxygen and nitrogen species, which further trigger DNA damage and results in a vicious circle (Adapted from [26]).

Evidence supporting DNA damage driven inflammation as contributing factors in ageing stemmed from studies in progeroid mouse models. For example, NFκB was found to be activated in tissues of the *Ercc1*$^{-/\Delta}$ mice, as well as in tissues of naturally aged mice[114]. The researchers showed that DNA damage and the subsequent inflammatory response can act as drivers of the accelerated ageing process, since inhibition of NFκB (either genetically or pharmacologically) delayed the manifestation and magnitude of the age-related symptoms. This was also observed in other mouse models of accelerated ageing, with inhibition of NFκB ameliorating the age-related pathologies and leading in lifespan extension[115]. In support of these findings, NFκB inhibition partially rescued osteoporosis in *Ercc1*$^{-/\Delta}$ mice, through reduction of cellular senescence and SASP. Due to the complex and segmental nature of the ageing process, tissue specific mouse models have been a valuable tool in the dissection of the cause and effect relation in these pathologies. For example, a direct link between DNA damage-induced inflammation and tissue degeneration was shown in a mouse model with absence of ERCC1 (and thus DNA repair defect) only in adipose tissue[116]. Adipose tissue of these mice accumulated DNA damage and exerted persistent DDR signaling activation. In addition, pro-inflammatory factors were upregulated and triggered the recruitment of activated macrophages. Due to the inability to repair the damage, DDR activation was continued and the immune response remained unresolved, ultimately leading to a chronic auto-inflammatory response, adipose tissue degeneration and fat depletion.

## Aim of the study

Accumulating body of evidence point to a functional interplay between the organism's defensive systems, those of DNA repair and immune response, in the regulation of tissue homeostasis and the control of the ageing process. Disruption of either pathway is associated with systemic responses that affect the metabolic status of the organism and contribute to the manifestation of age-related pathologies and cancer.

A study of a mouse model with defective immunotoxicity and thus immune function reported shorter lifespan and progeroid phenotypes, due to elevated SASP and chronic inflammation[117]. Thus, it seems that not only SASP acts as a trigger to chronic inflammation, but, *vice versa*, it can be the immune mechanism itself one of the regulators of SASP. This sets the proper immune function as crucial for the balance between the beneficial roles of senescence (such as in wound healing) and the detrimental, ageing-promoting SASP. In

addition, it is known that, apart from the traditional role of the immune system in anti-infectious protection, immune cells also interact with and regulate metabolic systems, promoting metabolic homeostasis and preventing from cancer and age-associated metabolic decline. Indeed, perturbed expression of multiple cytokines has been reported to affect systemic metabolic balance, e.g. by interfering in glucose and insulin signaling[118]. Finally, as with DNA damage, immune response is also found to be coupled to both the ageing process and decline as well as to cancer development.

In parallel, defects in DNA repair and the subsequent accumulation of irreparable DNA damage promote cellular responses, including the induction of cell death and senescence, which have been implicated in the development of age-related phenotypes. In addition to those cell-autonomous responses, DNA damage triggers non cell-autonomous systemic adaptive responses and metabolic alterations, such as altered glucose metabolism and dampening of anabolic signaling. Multiple progeroid mouse models, such as those of the WRN, AT and HGPS syndromes manifest disturbed metabolism and are at high risk of insulin resistance and type 2 diabetes development[119]. However, we are lacking mechanistic insight into how the DNA repair mechanism and the immune response impact the function of metabolic organs and impair the metabolic homeostasis. One step towards understanding the direct role of repair factors was taken in the study of Karakasilioti I. *et al*., where it was shown that *Ercc1* deficiency in adipose tissue led to progressive degeneration of the tissue and impaired systemic glucose metabolism, through the transcriptional activation of proinflammatory genes and the induction of chronic autoinflammatory response. Thus, this study confirmed a direct effect of DDR in the perturbation of systemic metabolic balance and the progression of age-associated degeneration[116].

Overall, it seems that the protective systems of DNA damage response and immune response are both crucial to cellular and organismal survival. Both are complex, multilayered and tightly regulated, regarding the magnitude and the timing of the response and their effect is a double-edged sword. More specifically, short term activation of both protects from excessive stress by restricting damage and potentially harmful, malfunctioning cells. However, long-term activation is associated with excessive cellular and tissue damage and systemic homeostatic loss. This sets both mechanisms at the crossroad of metabolic homeostasis, ageing and cancer. The fact that these pathways also interfere and regulate one another, makes it even more complex to delineate their role and contribution in the pathogenesis of all the above mentioned.

Here, we attempt to dissect the functional link between DNA damage and the immune response. To do so, we generated a tissue specific DNA repair defective mouse model, which lacks the ERCC1 endonuclease specifically in circulating macrophages, the key mediators of innate immune response with additional roles in the regulation of tissue homeostasis. Using this mouse model, we aim to identify molecular mechanisms underlying the effects of genomic instability in systemic, age-associated pathologies.

# Results

## Generation of *Er1$^{F/-}$* mice

To study the functional links between irreparable DNA damage and innate immune responses *in vivo*, we crossed mice homozygous for the floxed *Ercc1* allele (*Ercc1$^{F/F}$*)[120] with mice carrying the Lysozyme 2 (Lys2)-Cre[121] in an *Ercc1* heterozygous background (*Lys2-Cre; Ercc1$^{+/-}$*). The *Lys2-Cre* mice carry the Cre recombinase gene under the control of Lys2 promoter/ enhancer elements, which drives the expression of Cre in the myeloid lineage (monocytes, mature macrophages, neutrophils) and has been extensively used for the generation of conditional macrophage-specific knock out mouse models. To confirm the specificity of our system, we intercrossed the *Lys2-Cre* mice with Rosa26 YFP transgenic animals, so as to track Cre expression in multiple cell types and tissues. Immunofluorescence staining and Western blot of thioglycollate-elicited peritoneal macrophages (TEMs), primary pancreatic cells (PPCs) and primary hepatocytes from *Rosa26$^{LysCre}$* and control *Rosa26* mice confirmed the specificity of Lys2-driven Cre expression **(Figure 3A)**. In addition, Cre expression was also detected in infiltrating MACI-positive macrophages in the pancreas, white adipose tissue (WAT) **(Figure 3B)** and hypothalamus **(Figure 3C)** of *Rosa26$^{LysCre}$* mice. In the case of hypothalamus the majority of the CRE-positive cells were found to be macrophage-marker positive (Mac1$^{+}$) and not neuron-specific marker positive(NeuN$^{+}$).

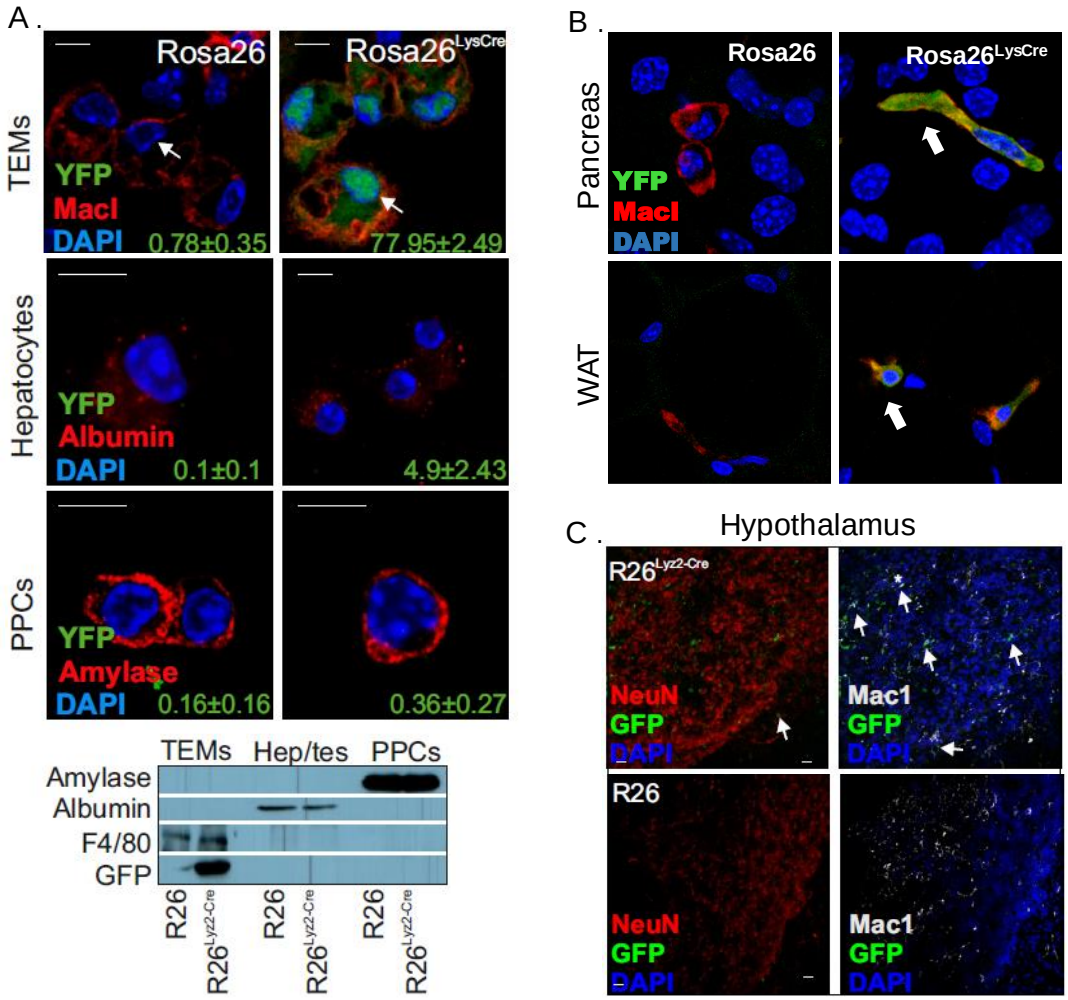


**Figure 3. Tissue specificity of Lys2-Cre expresision. (A)** Cofocal microscopy (upper panel) and Western blotting (Lower panel) of *Lys2-Cre*-driven Rosa-YFP expression in thioglycolate-elicited peritoneal macrophages (TEMs; n>500 cells counted per genotype), hepatocytes and primary pancreatic cells (PPCs) (n>100 cells counted per genotype). The numbers indicate the average % of GFP (+) cells +/- SEM). **(B)** Immunofluorescence staining of Lys2-Cre-driven Rosa-YFP expression in the *Rosa26* and *Lys2-Cre;Rosa26-YFP* pancreas and the white adipose tissue (WAT) that are infiltrated with MAC1-positive macrophages (indicated by the arrowheads). **(C)** Immunofluorescence detection of *Lys2-Cre*-driven YFP expression in the hypothalamus of *Rosa26* and *Lys2-Cre;Rosa26-YFP* animals. Co-staining with the neuronal marker NeuN and macrophage marker MAC-1.

To test the efficiency of *Ercc1* deletion, we performed Western blotting in various cell types. We confirmed the excision of the floxed *Ercc1* allele in *Lys2-Cre; Ercc1*$^{F/-}$ populations (referred from now on *Er1*$^{F/-}$) in peritoneal macrophages, neutrophils and monocytes, but not in neurons and the hypothalamus (**Figure 4A-C**). Further confocal microscopy revealed the absence of ERCC1 expression in *Er1*$^{F/-}$ bone marrow-derived macrophages (BMDMs), TEMs, monocytes and neutrophils, but similar expression levels in the hypothalamus (**Figure 4D**). Together, these findings verify the efficiency of our system and the absence of ERCC1 specifically in the targeted cell populations.

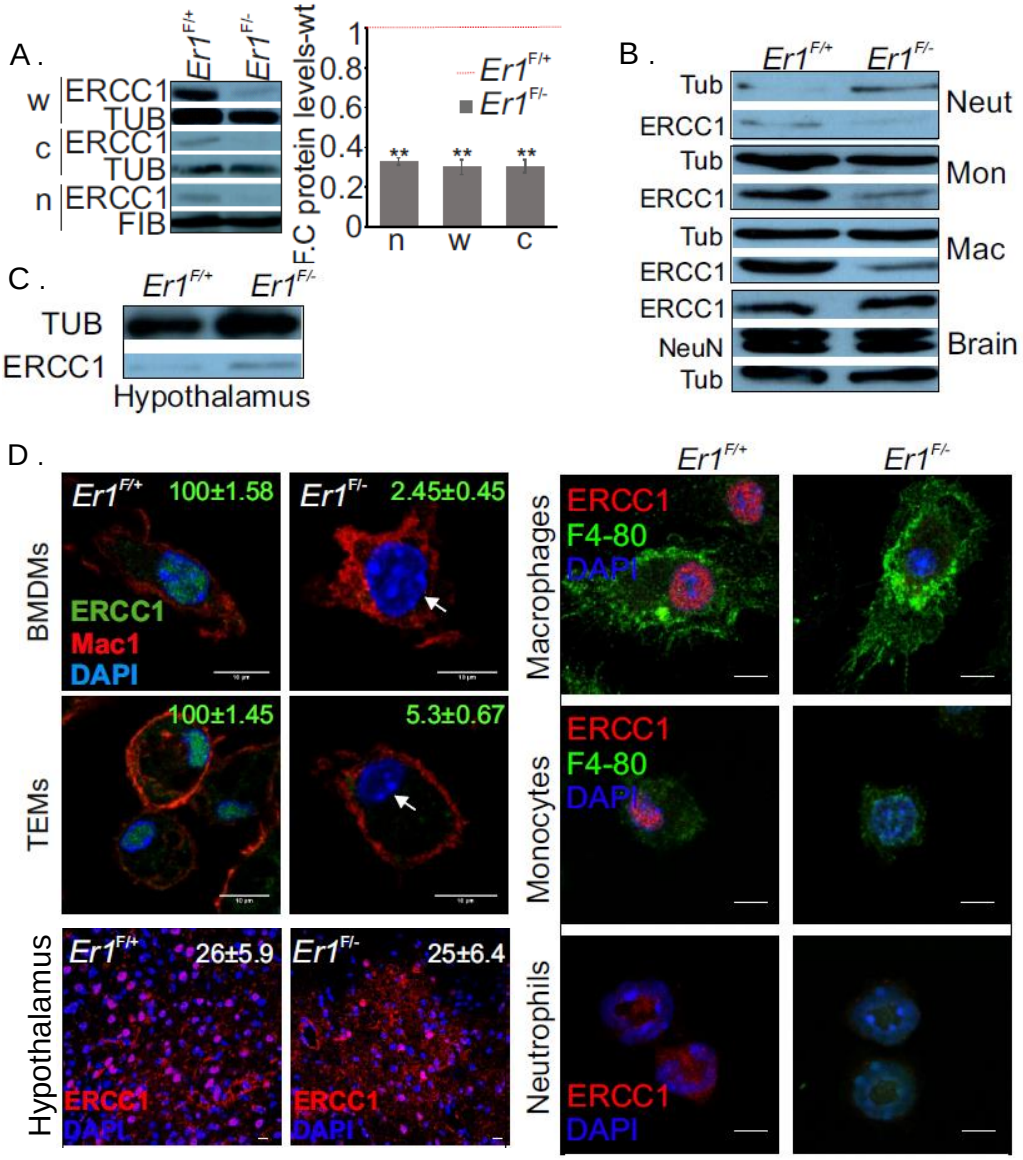


**Figure 4. Generation of thee macrophage-specific *Lys2-Cre;Ercc1$^{F/-}$* mice. (A)** Western blotting of ERCC1 protein in whole-cell (w) cytoplasmic (c) and nuclear (n) extracts. Tubulin (TUB) and Fibrillarin (FIB) were used as loading controls (as indicated). The graph represents the fold change (F.C.) of ERCC1 protein levels in *Er1$^{F/-}$* samples compared to corresponding *Er1$^{F/+}$* controls (n=3). **(B)** Western blotting of ERCC1 in neutrophils, monocytes, macrophages and brain tissue derived from *Er1$^{F/-}$* and *Er1$^{F/+}$* animals. **(C)** Western blotting of ERCC1 in the hypothalamus of *Er1$^{F/-}$* and *Er1$^{F/+}$* animals. **(D)** Immunofluorescence detection of ERCC1 in bone marrow-derived macrophages (BMDMs), Thioglycollate-elicited macrophages (TEMs), and hypothalamus of *Er1$^{F/-}$* and *Er1$^{F/+}$* mice. The numbers indicate the average % of ERCC1 (+) nuclei +/- SEM in *Er1$^{F/+}$*and *Er1$^{F/-}$* BMDMs, TEMs (n>150 cells were counted per genotype) and hypothalamic regions (Left panel). Immunofluorescence detection of ERCC1 and the macrophage marker F4-80 in *Er1$^{F/-}$* and *Er1$^{F/+}$* macrophages, monocytes and neutrophils. Grey line is set at 5μm scale. (Left panel).

To test if *Ercc1* deletion could affect the differentiation and viability of the cells, we counted the total number of $CD45^+CD11b^+$ macrophages during hematopoiesis (bone marrow). No decrease was reported in those macrophages and the same was the case for the $CD45^+CD11b^+$ macrophages numbers in peripheral tissues (blood, spleen and pancreas) from $Er1^{F/-}$ and *Lys2-Cre;* $Ercc1^{F/+}$ *(*referred from now on as $Er1^{F/+}$ or wild type; wt.) mice. However, a slight increase in the frequencies of $CD45^+CD11b^+$ cells was seen in $Er1^{F/-}$ counts (**Figure 5A**). In addition, forward scatter histograms of $CD45^+CD11b^+$ macrophages in the spleen of $Er1^{F/-}$ mice revealed the presence of a population with higher volume, indicative of an activated status of those macrophages, compared to those from $Er1^{F/+}$ mice (**Figure 5B**). Staining with caspase 3 showed few, if any, apoptotic cells in $Er1^{F/-}$ TEMs (**Figure 5C**) while senescence-associated (SA)-β-gal assay revealed increased expression of β-galactosidase in $Er1^{F/-}$ BMDMs (**Figure 5D**). Since the SA-β-gal assay is indicative of senescence, we further tested the senescence status with additional assays. Indeed, staining with a lipophilic, biotin-linked Sudan Black B analogue (GL13; commercially available SenTraGor®[122] in BMDMs revealed a uniform, >4-fold accumulation of lipofuscin (**Figure 5C**). Likewise, western blotting for Lamin B1 revealed a mild but consistent senescence-associated decrease in Lamin B1 levels in $Er1^{F/-}$ BMDMs (**Figure 5E**).

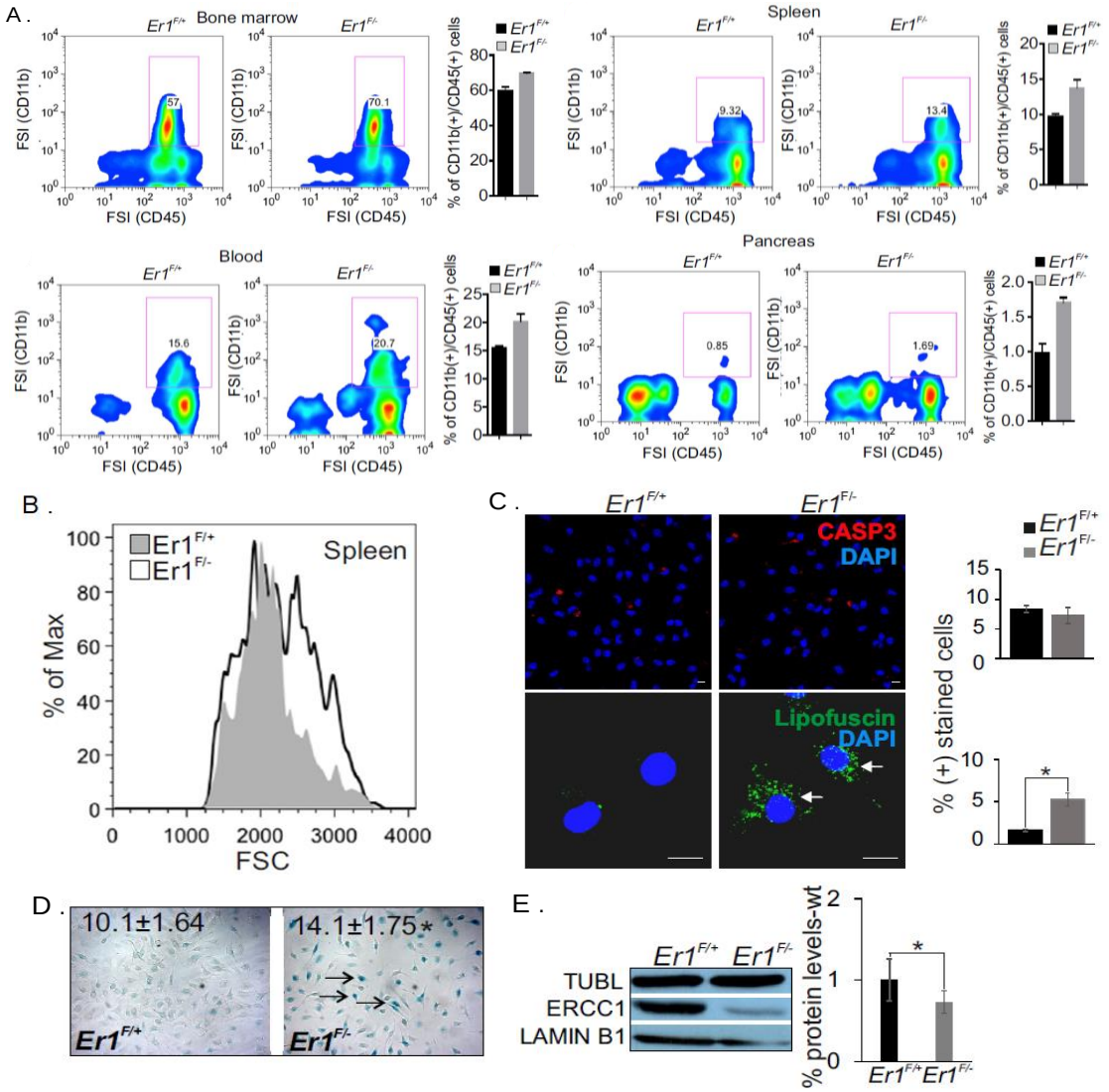


**Figure 5. Effects of ERCC1 deletion in macrophages. (A)** FACS representative plots and respective graphs of CD45+CD11b+ cells, in the bone marrow, blood, spleen and pancreas of 6-months old *Er1*$^{F/-}$ and *Er1*$^{F/+}$ animals (as indicated; n=6). All tissues are derived from the same Er1F/- and Er1F/+ animals. Significance is set at P<0.05 (unpaired t-test). Asterisk indicates the significance set at p-value: *≤0.05, **≤0.01 (two-tailed Student's t-test unless stated otherwise). **(B)** Representative forward scatter histograms of CD45+CD11b+ macrophages in the spleen of *Er1*$^{F/+}$ (grey-shaded peak) and *Er1*$^{F/-}$ (black-lined peak) mice (n=6) as measured by flow cytometry. The presence of a second FSC peak in *Er1*$^{F/-}$ histogram depicts the existence of a population of bone marrow derived monocytes/macrophages with higher volume, indicative of their activation/differentiation status. **(C)** Immunofluorescence detection of Caspase 3 (CASP3) (n>300 cells were counted per genotype) and GL13 (indicated by the arrowhead), commercially available SenTraGor®, in *Er1*$^{F/-}$ and *Er1*$^{F/+}$ BMDMs. Fluorescence intensity was calculated in n>50 cells per genotype. Grey line is set at 5μm scale. Error bars indicate S.E.M. among replicates (n ≥ 3). Asterisk indicates the significance set at p-value: *≤0.05, **≤0.01 (two-tailed Student's t-test). **(D)** SA-β-gal-staining in *Er1*$^{F/-}$ and *Er1*$^{F/+}$ BMDMs; n>500 cells were counted for each genotype from three independent experiments. **(E)** Western blotting of Lamin B1 in *Er1*$^{F/-}$ and *Er1*$^{F/+}$ BMDMs (n=5). Graphs represent data from Western blotting quantification; Asterisk indicates the significance set at p-value: *≤0.05, one-tailed Student's t-test.

Since ERCC1 is an endonuclease involved in NER and ICL repair, we performed confocal microscopy experiments to determine the presence of DNA lesions and DNA repair signaling in the targeted cells.The number of phosphorylated histone H2A.X (γH2AX) foci, a histone variant accumulated at sites of DNA breaks, was found to be elevated in the nuclei of *Er1*$^{F/-}$ BMDMs (upper panel) and TEMs (lower panel), compared to the respective *Er1*$^{F/+}$ controls (**Figure 6A**).The same was reported for markers of ICL repair (FANCI), HR-mediated DSB repair (RAD51) and activated DNA damage response (phosphorylated ATM) for BMDMs and for TEMs (**Figure 6B**, **Figure 6C,** respectively). Thus, tissue-specific ablation of *Ercc1* triggers the accumulation of cytotoxic DNA damage and the activation of DNA damage signaling and leads to an activated status and senescent-like phenotype in macrophages.

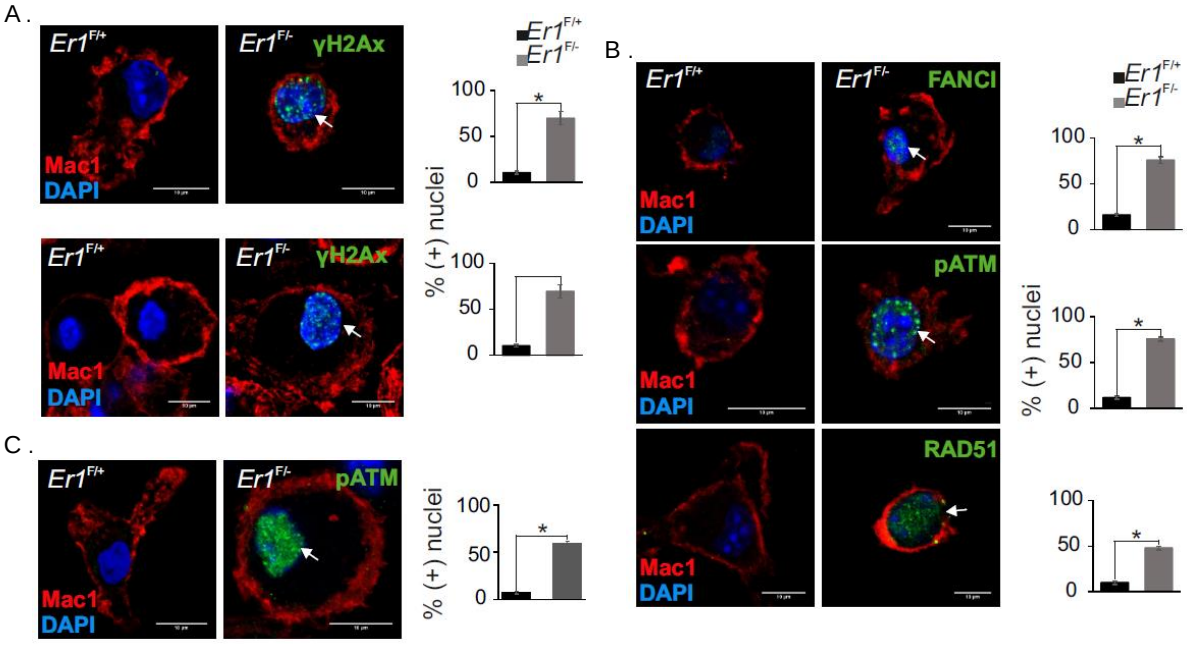


**Figure 6. DNA damage accumulation in *Er1*$^{F/-}$ macrophages.** Immunofluorescence detection of **(A)** γ-H2AX in *Er1*$^{F/-}$ and *Er1*$^{F/+}$ BMDMs (Upper panel) and TEMs (Lower panel). **(B)** FANCI, pATM and RAD51 in *Er1*$^{F/-}$ and *Er1*$^{F/+}$ BMDMs (in each case n>200 cells were counted per genotype). **(C)** pATM in *Er1*$^{F/-}$ and *Er1*$^{F/+}$ TEMs (n>150 cells were counted per genotype). Asterisk indicates the significance set at p-value: *≤0.05 (two-tailed Student's t-test).

## Abrogation of ERCC1 triggers cytoplasmic stress responses

Autophagy is a homeostatic process, which acts as a stress response pathway and interacts with multiple other signaling pathways, including this of the immune response, so as to protect cells from damage and stressful conditions[123]. In addition, endoplasmic reticulum (ER) is a metabolic compartment of a cell and is crucial for processes including protein translation, quality control, modifications and secretion. Various conditions that lead to homeostatic perturbations activate the ER stress response to benefit cell survival[124]. Among other pathways, both autophagy and ER stress response

have been linked to DNA damage response[125,126] as well as to immune cell and macrophage function[127]. To further evaluate the consequences of ERCC1 absence, we conducted a series of confocal microscopy studies in *Er1*$^{F/-}$ and *Er1*$^{F/+}$ macrophages to detect the HSP chaperone GRP78,P62, LC3β and GM130. GRP78 is known to be required for the ER membrane integrity and a marker for ER stress[128]. LC3β associates with all types of autophagic membranes, providing a good index of autophagy induction. In addition to LC3β, P62 is an adaptor protein that facilitates the degradation of the autophagosomes. Thus, P62 amount in the cell is considered to be inversely correlated to autophagic activity[129] and its accumulation is indicative of defective autophagy[130].Finally, GM130 is a membrane protein localized at the Golgi, with a role in the maintenance of the structure of Golgi apparatus[131]. The results revealed ER dilation, accumulation of autophagosomes and dispersed and fragmented Golgi apparatus in *Er1*$^{F/-}$ macrophages. (**Figure 7A**). These results were further confirmed by Western blotting (**Figure 7B**). As a positive control, *Er1*$^{F/+}$ BMDMs were treated with nocodazole (which is known to trigger Golgi dispersal), chloroquine (an inhibitor of lysosomal-dependent degradation of autophagosomes) and tunicamycin (an ER stress inducer). Confocal microscopy and Western blotting confirmed the validity of GRP78, P62, LC3 and GM130 as markers for the cytoplasmic stress responses observed in *Er1*$^{F/-}$ macrophages (**Figure 7C, 7D**). To test that these responses were not a secondary response, but rather a direct effect of the DNA repair deficiency of the macrophages, we exposed *Er1*$^{F/+}$ BMDMs to mitomycin C (MMC), an inducer of ICLs. Similar to *Er1*$^{F/-}$ macrophages, treatment with MMC led to dilated ER, autophagy and Golgi dispersal (**Figure 7E**). Exposure of the WT macrophages to lipopolysaccharide (LPS), a potent activator of macrophages, mimicked the MMC effects on autophagy and Golgi dispersal, but failed to increase GRP78 levels (**Figure 7F**). The direct cause-effect relationship between DNA damage and the cytoplasmic responses was further verified after treatment of the MMC-exposed macrophages to the ATM inhibitor KU55933 (ATMi) or the ATR inhibitor NU6027 (ATRi). Upon inhibition of the DDR signaling, we observed reversal of the MMC-induced Golgi dispersal (**Figure 7G**), as well as dampening of LC3 and GRP78 protein levels (**Figure 7H**). Thus, DNA damage and the subsequent DDR signaling are direct drivers of cytoplasmic responses in macrophages, including autophagy and morphological alterations of ER and Golgi. To gain further insight into morphological changes in *Er1*$^{F/-}$ macrophages, we conducted transmission electron microscopy (TEM) in *Er1*$^{F/+}$ (**Figure 7I I and II**) and *Er1*$^{F/-}$ macrophages (**Figure 7I III-VIII**). In accordance to the previously observed dilation of ER and Golgi, which have central role in the regulation of cellular secretion processes, TEM revealed accumulation of intracellular vesicles (**Figure 7I III**), organized into larger vacuolar structures (**Figure 7I IV**). In addition, *Er1*$^{F/-}$ macrophages extensively showed higher numbers of cytoplasm-filled projections (**Figure 7I V**) that formed a complex network of pseudopodia-like structures (**Figure 7I VI**), containing vesicles (**Figure 7I VII, VIII**). These findings, together with the increased cell volume observed by Flow cytometry (**Figure 5B**) support the phenotype of activated macrophages, which includes an increase in size, formation of membrane projections and accumulation of intracellular vacuoles[132]. In addition, all of these morphological alterations together point to altered endocytic/exocytic pathways and the enhanced formation of

intraluminal vesicles (ILVs) and multivesicular bodies (MVBs), as well as secretion of extracellular vesicles (EVs) by *Er1*$^{F/-}$ macrophages[133].

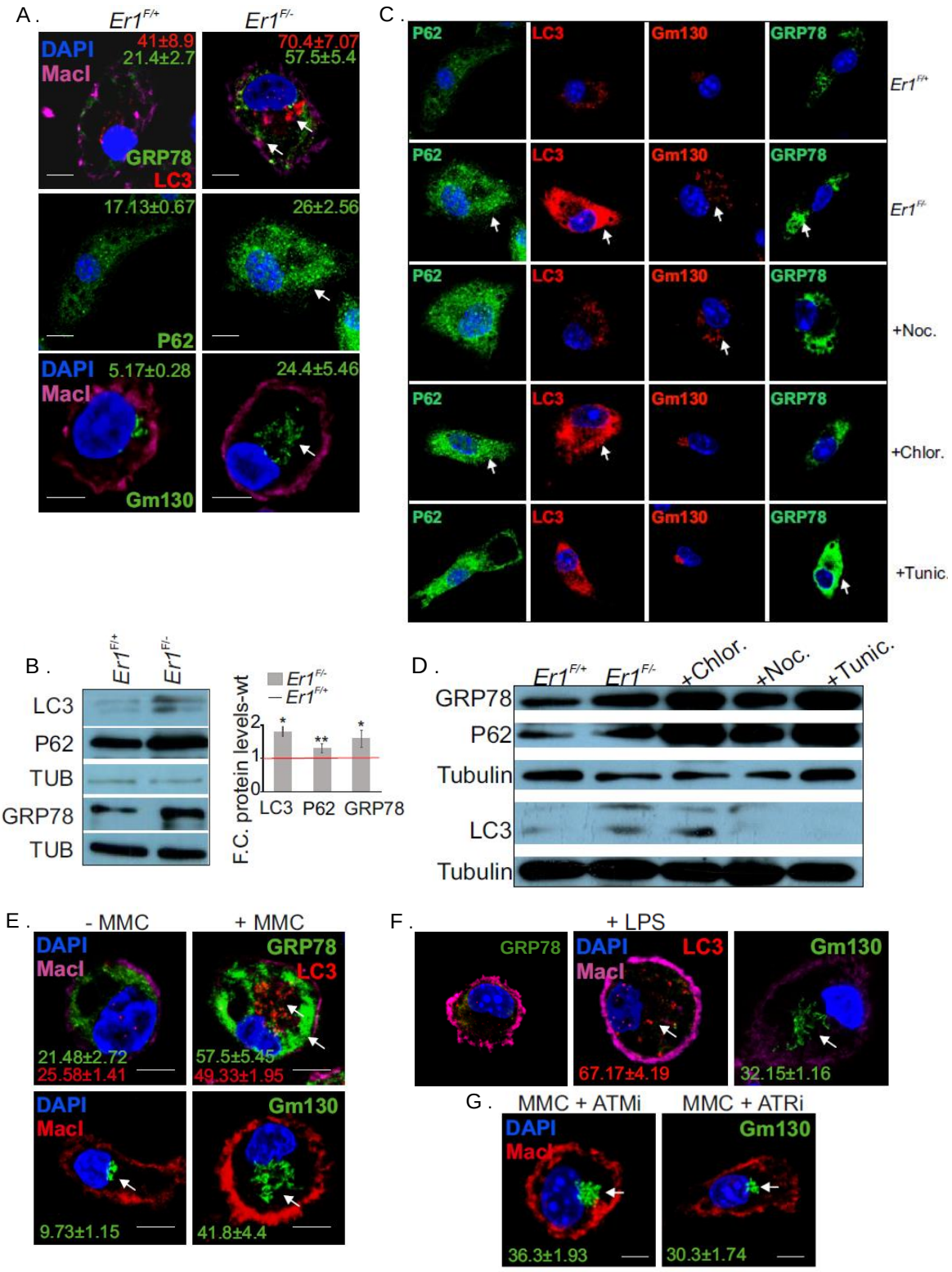

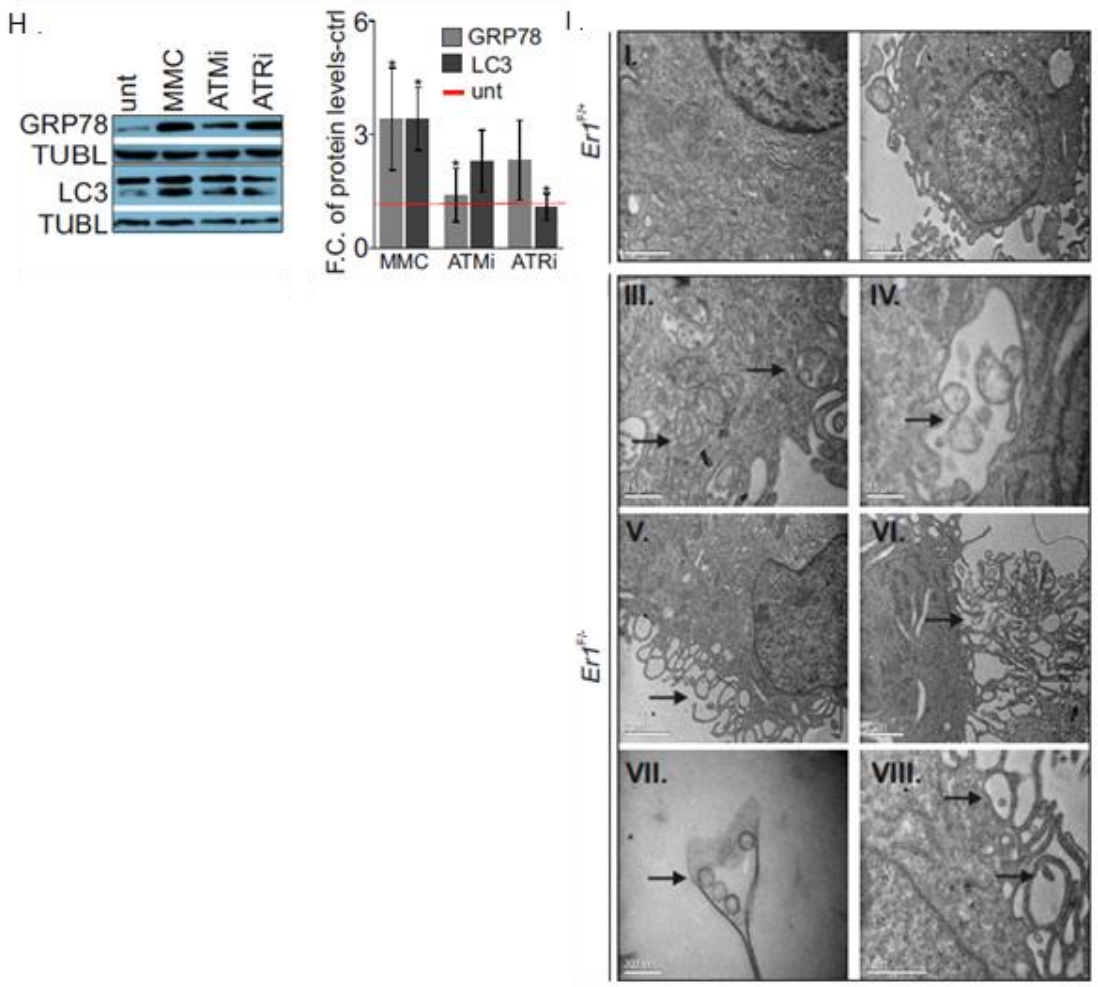


**Figure 7. Abrogation of ERCC1 triggers cytoplasmic stress responses in *Er1*$^{F/-}$ macrophages. (A)** Immunofluorescence detection of GRP78 (n>250 cells counted per genotype) marking the dilation of ER, LC3 (n>40 cells counted per genotype) for autophagy, P62 for autophagic activity (n>15 optical fields per genotype, ~150 cells per field) and Gm130 for Golgi dispersal (~500 cells per genotype); (as indicated by the arrowhead, respectively) in *Er1*$^{F/-}$ and *Er1*$^{F/+}$ BMDMs. For GRP78 and LC3, the colored numbers indicate the average % of (+) stained cells +/-SEM for the indicated, color-matched protein. For p62, the colored numbers indicate the average mean fluorescence intensity +/-SEM of p62 signal. For Gm130, the green-colored numbers indicate the average % of (+) stained cells +/-SEM showing Golgi dispersal. **(B)** Western blot levels of GRP78, P62, LC3 and Tubulin in *Er1*$^{F/-}$ and *Er1*$^{F/+}$ BMDMs. The graph shows the fold change of indicated protein levels in *Er1*$^{F/-}$ BMDMs compared to *Er1*$^{F/+}$ (red line) corresponding controls (n = 3 per group) Error bars indicate S.E.M. among replicates (n ≥ 3). Significance set at p-value: *≤0.05, **≤0.01 (two-tailed Student's t-test). **(C)** Confocal studies of P62, LC3, Gm130, and GRP78 in *Er1*$^{F/-}$ and *Er1*$^{F/+}$ BMDMs and *Er1*$^{F/+}$ BMDMs treated with nocodazole (noc.; known to trigger Golgi dispersal), chloroquine (Chlor.; known to inhibit the degradation of autophagosomes in lysosomes) and tunicamycin (Tunic.; known to trigger ER stress.). **(D)** Western blotting of GRP78, P62, LC3 and Tubulin in *Er1*$^{F/-}$ and *Er1*$^{F/+}$ BMDMs and *Er1*$^{F/+}$ BMDMs treated with nocodazole (noc.), chloroquine (Chlor.) and tunicamycin (Tunic.). **(E)** Immunofluorescence detection of GRP78 (for ER stress) (n>500 cells counted per genotype), LC3 (for autophagy) (n>750 cells counted per genotype) and Gm130 (for

Golgi dispersal) in MMC-treated BMDMs (shown by the arrowhead, respectively; n> 500 cells counted per genotype). The colored numbers indicate the average % of (+) stained cells +/-SEM for the indicated, color-matched protein. For Gm130, the green-colored numbers indicate the average % of (+) stained cells +/-SEM showing Golgi dispersal. **(F)** Immunofluorescence detection of LC3 (for autophagy) (~250 cells counted per genotype) and Gm130 (for Golgi dispersal) (~950 cells counted per genotype) in LPS-stimulated BMDMs. **(G)** Immunofluorescence detection of Gm130 (for Golgi dispersal) in MMC-treated and control BMDMs exposed to ATM (ATMi) (~200 cells counted) or ATR (ATRi) (500 cells counted) inhibitor (as indicated). The green-colored numbers indicate the average % of (+) stained cells +/-SEM showing Golgi dispersal. **(H)** Western blot levels of GRP78 and LC3 in MMC-treated and control (ctrl) macrophages exposed to ATM (ATMi) or ATR (ATRi) inhibitor (as indicated; Tubl.: tubulin). The graph represents the fold change in indicated protein levels in MMC-treated macrophages exposed to ATM (ATMi) or ATR (ATRi) inhibitor compared to corresponding controls (red line) (n = 4 per group). **(I)** Representative transmission electron micrographs of Er1F+ (I, II) and Er1F/- (III-VIII) BMDMs. Black-colored arrowheads depict the presence of intracellular vesicles (III), organized in larger vacuolar structures (IV), the appearance of cytoplasm-filled projections (V), the convoluted network of pseudopodia-like structures (VI) containing vesicles (VII) and pseudopodia-associated extracellular vesicles (VIII). Scale bars are shown separately for each micrograph. Asterisk indicates the significance set at p-value: *≤0.05, **≤0.01 (two-tailed Student's t-test). Grey line is set at 5μm scale.

## The ERCC1 defect in macrophages trigger systemic metabolic alterations in *Er1$^{F/-}$* mice

*Er1$^{F/-}$* mice were born at the expected Mendelian frequency and showed no developmental defects or other pathological phenotypes. Despite their similar body size (**Figure 8A**), compared to their littermate controls, *Er1$^{F/-}$* mice maintained a lower body weight over a period of 22 weeks (**Figure 8B**) and lower epididymal fat (**Figure 8C**). To exclude the possibility of reduced food intake, we monitored food consumption on a daily basis for a period of 14 days and observed no differences between *Er1$^{F/+}$* and *Er1$^{F/-}$* mice (**Figure 8D**). In addition, we observed minimal expression of Lys2-Cre in the hypothalamus (**Figure 3C**) and normal ERCC1 expression in the same area (**Figure 4C, 4D**), further supporting that the reduced bodyweight is not the result of loss of appetite (which is regulated by the hypothalamic region). We also observed mild, yet noticeable, lower serum glucose levels in *Er1$^{F/-}$* mice (**Figure 8E**), although serum insulin levels were similar between *Er1$^{F/+}$* and *Er1$^{F/-}$* mice (**Figure 8F**).

Macrophages are known to infiltrate and reside in most tissues, including the metabolic ones (e.g. WAT, liver), affecting local and systemic metabolic cues[134]. To investigate whether the ERCC1 defect in macrophages could trigger the onset of metabolic alterations in *Er1$^{F/-}$* mice, we performed glucose tolerance tests (GTT) in 2-months old *Er1$^{F/+}$* and *Er1$^{F/-}$* mice fed *ad libitum* on a normal diet (ND) over a period of 2, 4 and 6 months. After a 16-hour fasting, mice were injected with a single dose of glucose, and blood glucose was measured at consecutive time points for a period of 3 hours. After 2 months on ND, there was no difference in the response to glucose between *Er1$^{F/+}$* and *Er1$^{F/-}$* mice. However, after 4 and 6 months, *Er1$^{F/-}$* mice progressively became more glucose tolerant than the WT controls (**Figure 8G**). On the other hand, 8-

month old *Er1*$^{F/+}$ and *Er1*$^{F/-}$ mice (fed an ND for 6 months) showed no difference in insulin sensitivity (**Figure 8H**) during insulin tolerance test (ITT), and comparable insulin-stimulated glucose uptake, as seen by 2-Deoxy-D-glucose (2-DG) levels in liver and muscle protein extracts (**Figure 8I, 8J**).

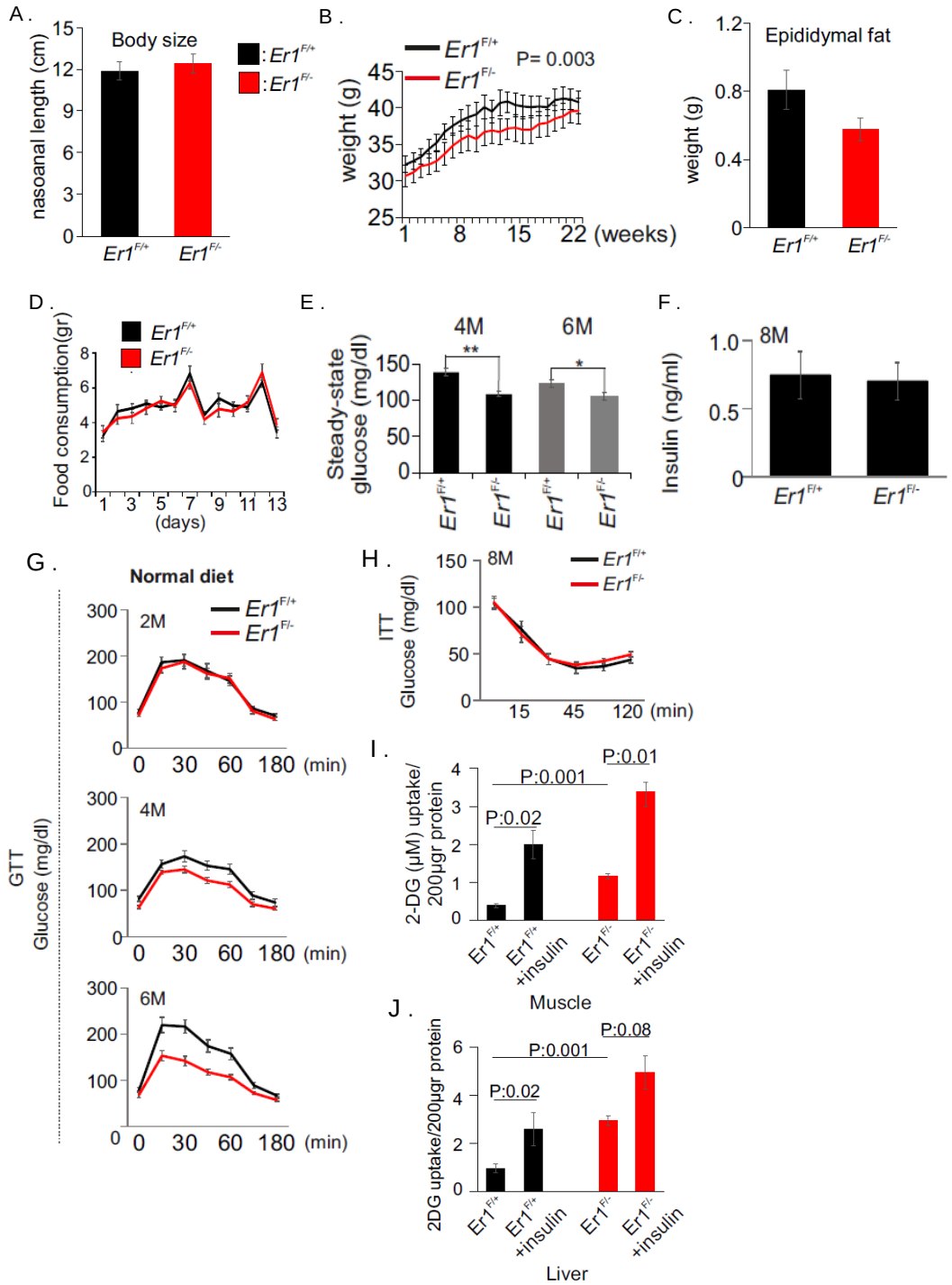


**Figure 8. The ERCC1 defect in macrophages triggers metabolic alterations in *Er1*$^{F/-}$ mice. (A)** Nasoanal length of 2-months old *Er1*$^{F/-}$ (n=10) and *Er1*$^{F/+}$ (n=11) animals. **(B)** Weights curves of 2-months old *Er1*$^{F/-}$ and *Er1*$^{F/+}$ animals (n=8) over a period of 22 weeks. **(C)** Weighs of epididymal fat depots of 2-months old *Er1*$^{F/-}$ (n=10)

and *Er1*$^{F/+}$ (n=11) animals. **(D)** Food intake (g) for 7months old males *Er1*$^{F/-}$ and *Er1*$^{F/+}$ animals (n=7) over a period of 14 days. **(E)** Steady-state glucose serum levels of 4- and 6-months (M) old *Er1*$^{F/-}$ and *Er1*$^{F/+}$ mice after 2 hours of fasting (n=8). **(F)** Serum insulin levels of 8-months (M) old *Er1*$^{F/-}$ (n=10) and *Er1*$^{F/+}$ (n=7) mice. **(G)** Glucose tolerance test (GTT) graphs of 2-months old *Er1*$^{F/-}$ and *Er1*$^{F/+}$ mice fed on a normal diet for a period of 2-, 4- and 6-months (M), as indicated. **(H)** Insulin tolerance test (ITT) graphs of 8-months (M) old *Er1*$^{F/-}$ and *Er1*$^{F/+}$ mice (n=8). **(I)** 2-Deoxy-D-glucose (2-DG) uptake (μM) in muscle and **(J)** liver protein extracts derived from overnight starved *Er1*$^{F/-}$ and *Er1*$^{F/+}$ animals injected with insulin (as indicated).

Administration of high fat diet (HFD) is known to trigger systemic metabolic abnormalities, as well as inflammation[135]. 2-months old *Er1*$^{F/+}$ and *Er1*$^{F/-}$ mice were fed a HFD for 4 months. In contrast to ND, upon HFD feeding, *Er1*$^{F/+}$ and *Er1*$^{F/-}$ mice showed no significant differences in body weight (**Figure 9A**). Nevertheless, HFD further enhanced the glucose tolerance of *Er1*$^{F/-}$ mice (**Figure 9B**) which also uncouples leanness of *Er1*$^{F/-}$ mice from the hypoglycemia and increased glucose tolerance observed in those mice compared to the WT controls. Finally, HFD led to insulin resistance to both *Er1*$^{F/+}$ and *Er1*$^{F/-}$ mice, compared to the respective ND fed mice, although no significant differences were reported between the two genotypes (**Figure 9C**). Together, these findings indicate that the enhanced glucose tolerance observed in *Er1*$^{F/-}$ mice is mediated through an insulin-independent pathway.

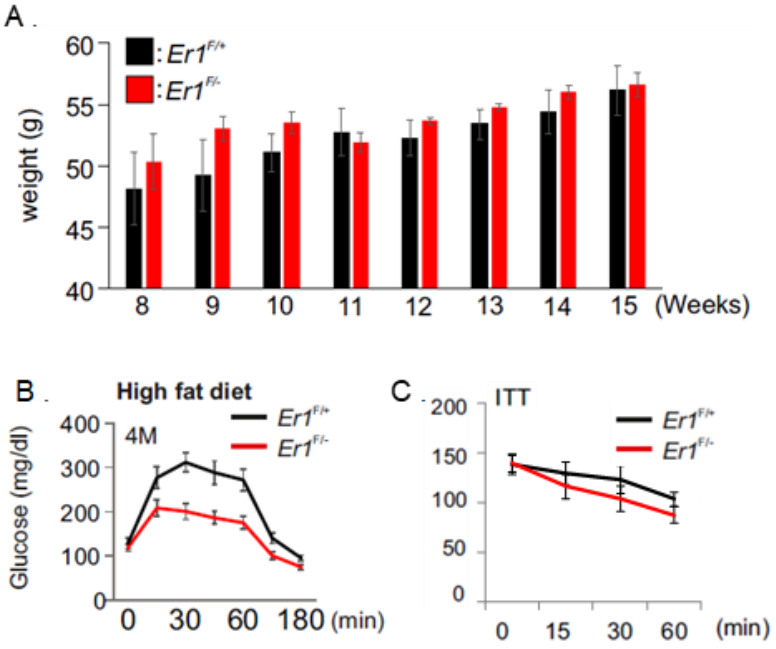


**Figure 9. High fat diet further enhances the glucose tolerance of *Er1*$^{F/-}$ mice. (A)** Weights of *Er1*$^{F/-}$ and *Er1*$^{F/+}$ animals (n=4) fed on a high fat diet for a period of 8-15 weeks (as indicated). **(B)** GTT graphs of 2-months old *Er1*$^{F/-}$ and *Er1*$^{F/+}$ mice (n=10) fed on a high-fat diet for a period of 4 months (M). **(C)** Insulin tolerance test (ITT) graphs of 8-months old *Er1*$^{F/-}$ and *Er1*$^{F/+}$ mice fed in a high-fat diet.

To gain further insight into the metabolic alterations of *Er1*$^{F/-}$ mice, we performed periodic acid-Schiff (PAS) and Red-oil staining in *Er1*$^{F/+}$ and *Er1*$^{F/-}$ livers, to detect glycogen and triglycerides (Tgs), respectively. We observed glycogen accumulation (**Figure 10A**) and lower triglyceride deposition (**Figure 10B**) in the livers of *Er1*$^{F/-}$ mice. The lower triglyceride deposition was also seen in the livers of *Er1*$^{F/+}$ and *Er1*$^{F/-}$ mice fed a HFD (**Figure 10B,** lower panel). Furthermore, we detected increased mRNA levels of genes involved in initiation of glycogen synthesis (glycogenin-1; *Gyg-1*, glycogen synthase; *Gys*), while reduced mRNA levels in genes associated with glycogen synthesis and breakdown (glycogen synthase kinase 3; *Gsk3*, glycogen phosphorylase; *Pygl*) in the livers of 6-monthls old *Er1*$^{F/-}$ mice (**Figure 10C**). Overall, we notice that ERCC1 defect in macrophages can lead to an altered metabolic profile in *Er1*$^{F/-}$ mice.

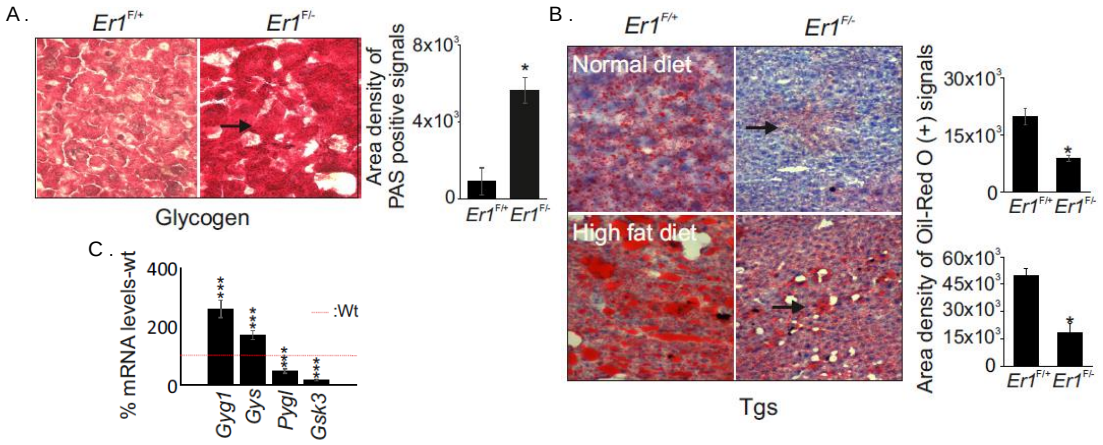


**Figure 10. Metabolic changes in *Er1*$^{F/-}$ mice. (A)** Representative periodic acid–Schiff (PAS) staining and quantification (3 optical fields per animal) of glycogen in *Er1*$^{F/+}$ and *Er1*$^{F/-}$ livers (n=4 animals per genotype). **(B)** Representative Red-oil staining and quantification (3 optical fields per animal) of triglycerides in the liver of *Er1*$^{F/+}$ and *Er1*$^{F/-}$ mice (n=3) fed on normal or high fat diet (as indicated); arrowhead indicates the decrease in fat deposition in the livers of *Er1*$^{F/-}$ animals fed on normal or high fat diet (as indicated). **(C)** *Gyg1, Gys, Pygl* and *Gsk3* mRNA levels in *Er1*$^{F/+}$ (red dotted line) and *Er1*$^{F/-}$ livers. Error bars indicate S.E.M. among replicates (n ≥ 3). Asterisk indicates the significance set at p-value: *≤0.05, **≤0.01 (two-tailed Student's t-test). Grey line is set at 5μm scale.

## ERCC1 defect in macrophages instigates a chronic inflammatory response in mice

Histological examination of various 8-months old *Er1*$^{F/+}$ and *Er1*$^{F/-}$ tissues, revealed the accumulation of monocytes and/or lymphocytes in perirenal fat, kidney, lung and liver of *Er1*$^{F/-}$ mice (**Figure 11A**). In addition, we detected the presence of GL13, lipofuscin-accumulating macrophages in the WAT of *Er1*$^{F/-}$ mice (**Figure 11B**). Confocal microscopy studies in the liver, pancreas and WAT of *Er1*$^{F/+}$ and *Er1*$^{F/-}$ mice showed accumulation of CD45$^{+}$ leukocytes and MacI$^{+}$ macrophages in the above-mentioned tissues of *Er1*$^{F/-}$ mice (**Figure**

**11C**). Together with the accumulation of immune cells, we also observed increased expression of the adhesion molecules PECAM-1, ICAM-1 and VCAM-1, all of which are associated with immune cell recruitment during an inflammatory response[136,137]. These data are in line with the reported increased frequencies of $CD45^+CD11b^+$ cells (**Figure 5A**) and with the presence of higher volume macrophages (**Figure 5B**), implicating the presence of activated macrophages and tissue inflammation. FACS analysis in 8-months old $Er1^{F/+}$ and $Er1^{F/-}$ as well as of $Er1^{F/+}$ HFD epididymal fat revealed similar increase in the infiltration of $F4/80^+$ cells (**Figure 11D**). $Er1^{F/+}$ HFD mice developed insulin resistance (**Figure 9C**), which is in line with the fact that HFD-induced obesity and expansion of adipose tissue leads to macrophage accumulation with subsequent tissue inflammation and insulin resistance[138]. However, $Er1^{F/-}$ mice, despite the macrophage accumulation and the signs of tissue inflammation, did not manifest increase of adipose tissue mass nor became insulin resistant (**Figure 11E, Figure 8C**). FACS analysis of $Er1^{F/+}$, $Er1^{F/-}$ and $Er1^{F/+}$ HFD WAT revealed, as expected from previous findings, increased presence of proinflammatory (M1 polarized) $CD11c^{high}$ macrophages in $Er1^{F/+}$ HFD mice. In contrast, we detected significantly higher number of alternatively activated (M2 polarized) macrophages in WAT of $Er1^{F/-}$ mice (**Figure 11F**). Although M1 macrophages have been linked to HFD-induced obesity and insulin resistance, M2 macrophages have been suggested to mediate tissue remodeling and protection from insulin resistance as well as cancer progression[139–142].

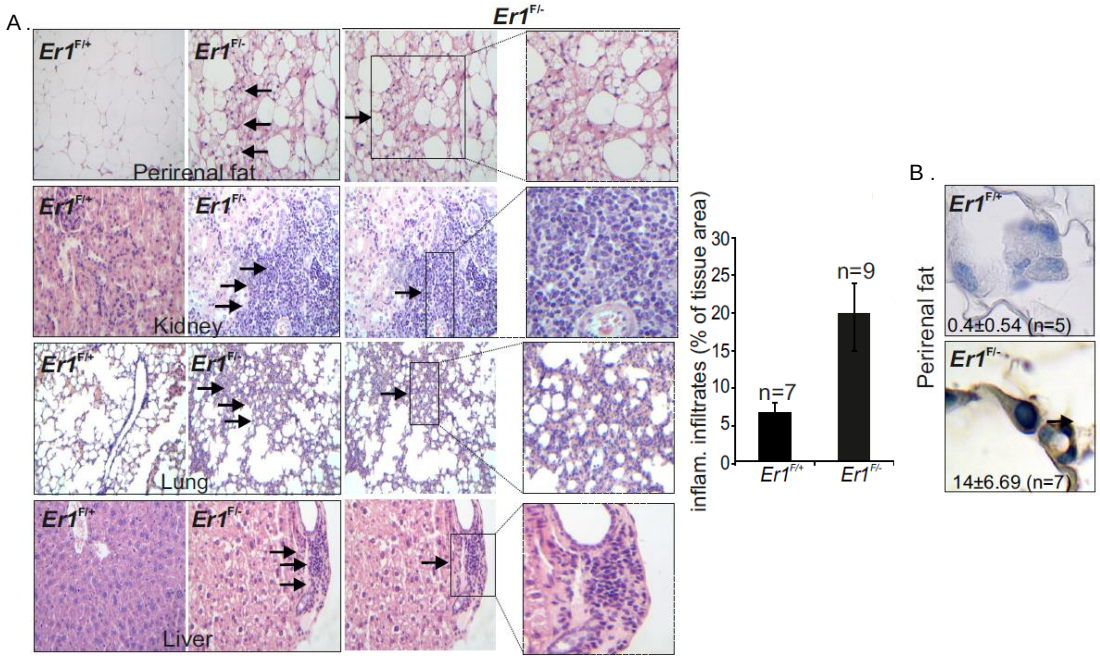

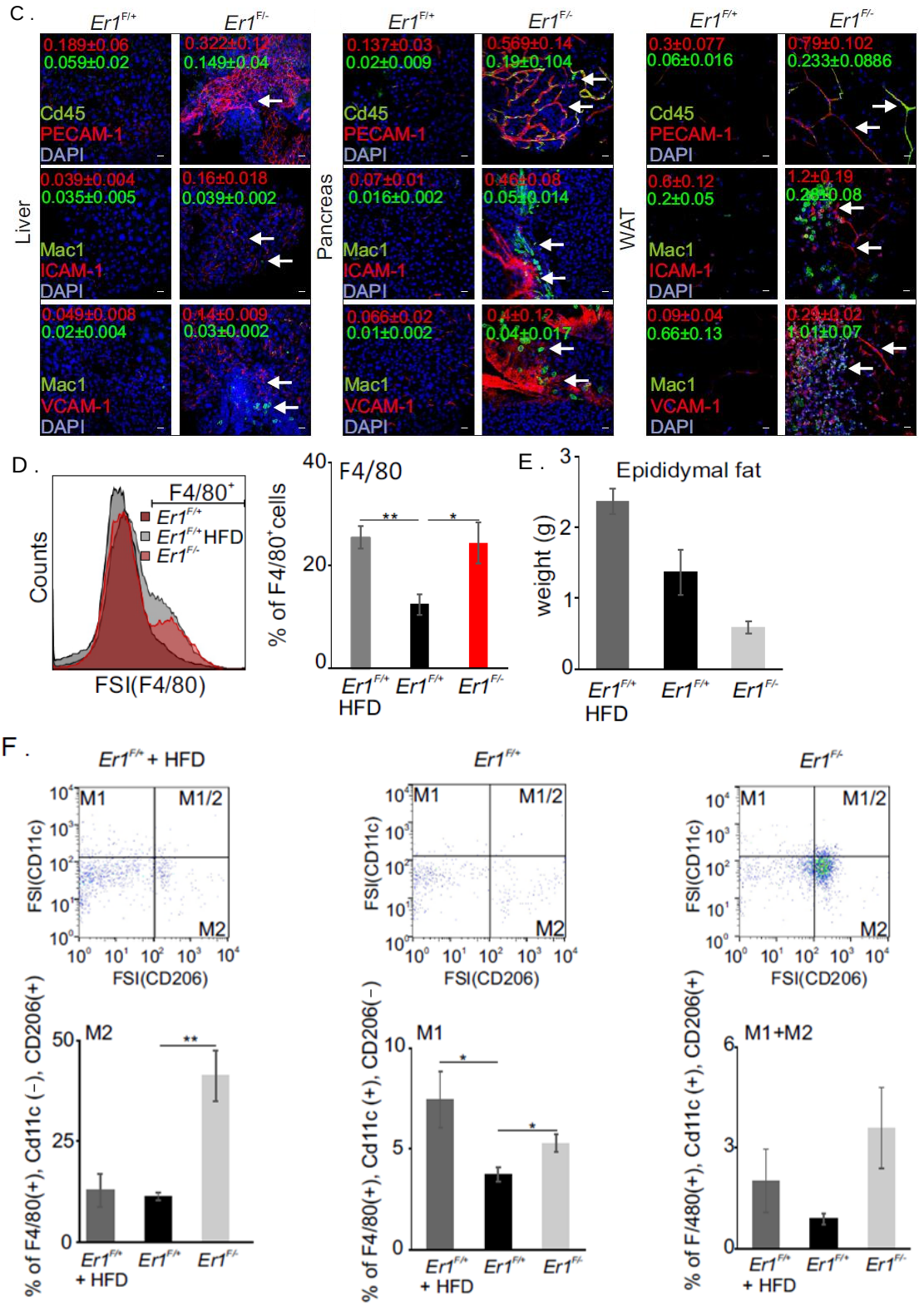


**Figure 11. Systemic, chronic inflammation in *Er1$^{F/-}$* mice. (A)** Infiltration of foamy cells (macrophages) in a region of lipogranuloma in *Er1$^{F/-}$* perirenal fat (as indicated) and inflammatory infiltration of lymphocytes and monocytes in *Er1$^{F/-}$* kidneys, lungs and livers. The third column represents magnified inlays showing the infiltration of f macrophages in the corresponding tissues of *Er1$^{F/-}$* mice. Dashed boxes indicate magnified inlays. **(B)** Detection of GL13 (+) macrophages in perirenal fat of *Er1$^{F/-}$* (n=7) and *Er1$^{F/+}$* (n=5) mice. **(C)** Immunofluorescence detection of the adhesion

moleculesPECAM-1, ICAM-1 and VCAM-1 along with CD45 and MAC1 (shown by the arrows) in the liver (n=4; 4-6 optical fields per animal), pancreas (n =3; 3 optical fields per animal) and white adipose tissue (WAT) (n =3; 2 optical fields per animal) of *Er1*$^{F/-}$ and *Er1*$^{F/+}$ mice indicating the expression of cell adhesion molecules and the presence of monocytic/lymphocytic infiltrates in *Er1*$^{F/-}$ tissues. Colored numbers indicate the average mean fluorescence intensity +/-SEM for the color-matched protein (as indicated). **(D)** Representative histograms of F4/80$^{+}$ macrophages in the epididymal fat of Er1$^{F/+}$, Er1$^{F/+}$ HFD and *Er1*$^{F/-}$ mice (n=3, 8-months old) as measured by flow cytometry. **(E)** Weighs of epididymal fat depots of *Er1*$^{F/+}$, *Er1*$^{F/+}$ HFD and *Er1*$^{F/-}$ mice. **(F)** FACS representative plots and respective graphs of F480$^{+}$/CD11c$^{+}$(M1), F480$^{+}$/CD206$^{+}$(M2) and F480$^{+}$/CD11c$^{+}$/CD206$^{+}$ double M1/M2 cells, in the white adipose tissue of *Er1*$^{F/+}$ , *Er1*$^{F/+}$ HFD and *Er1*$^{F/-}$ mice. Significance is set at P<0.05 (unpaired t-test). Asterisk indicates the significance set at p-value: *≤0.05, **≤0.01 (two-tailed Student's t-test).

To further understand the phenotypic alterations in macrophages due to the ERCC1 defect, we performed RNA-seq profiling of *Er1*$^{F/+}$ and *Er1*$^{F/-}$ BMDMs. The analysis revealed 1756 differentially expressed genes [meta-FDR≤0.005, fold change ≥ ±1.5, 1090 upregulated genes; 665 downregulated genes] (**Figure 12A**). Within this gene set, the gene ontology (GO)-classified biological processes associated with innate immune or GTPase-mediated signaling, membrane-bound projection and pathways associated with endosomal/vascular and ER-phagosome interactions and senescence in *Er1*$^{F/-}$ macrophages have a significantly disproportionate number of responsive genes relative to those mapped in the murine genome (false detection rate ≤0.05) (**Figure 12B-D**). In order to verify the RNA-seq results, we tested by qPCR the expression pattern of a set of inflammatory cytokine and chemokine genes in *Er1*$^{F/+}$ and *Er1*$^{F/-}$ BMDMs (**Figure 12E**). These results, together with our previous findings (increased inflammation, ER stress, autophagy, senescence and vesicle transport), confirmed the validity of the gene expression changes.

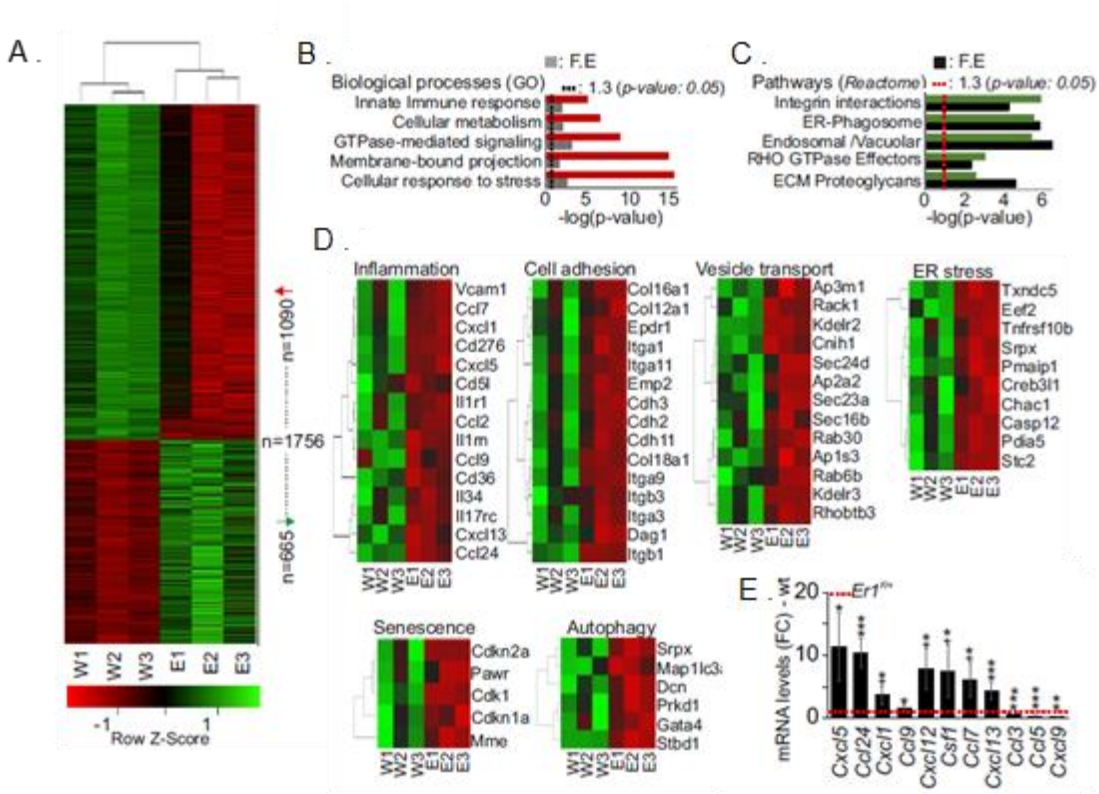


**Figure 12. Gene expression changes in *Er1*$^{F/-}$ mice. (A)** Heat-map representation of significant gene expression changes (n=1756 genes) in *Er1*$^{F/-}$ BMDMs compared to corresponding control cells. **(B)** Over-represented GO biological processes and **(C)** pathways (Reactome) of *Er1*$^{F/-}$ BMDMs compared to corresponding control cells; p: -log of p-value which is calculated by Fisher's exact test right-tailed, R: ratio of number of genes in the indicated pathway divided by the total number of genes that make up that pathway. **(D)** Heat-map representation of gene expression changes associated with significantly over-represented biological processes in *Er1*$^{F/-}$ BMDMs compared to corresponding control cells (as indicated). **(E)** Interleukin and chemokine mRNA levels in *Er1*$^{F/-}$ compared to *Er1*$^{F/+}$ (red dotted line) BMDMs. Error bars indicate S.E.M. among replicates (n ≥ 3). Asterisk indicates the significance set at p-value: *≤0.05, **≤0.01 and ***≤0.005 (two-tailed Student's t-test), "+": one-tailed-t-test. F. E.: fold enrichment, W: *Er1*$^{F/+}$, E: *Er1*$^{F/-}$. Grey line is set at 10μm scale.

## DNA damage triggers the generation and release of extracellular vesicles from ERCC1 defective macrophages

This far, we detected the activation of innate immune signaling and inflammatory response in peripheral tissues of *Er1*$^{F/-}$ mice, together with altered systemic metabolic profile (eg increased glucose tolerance). Thus, we hypothesized that ERCC1 defective macrophages activate signaling cascades to communicate with the tissues and trigger the systemic pro-inflammatory and metabolic responses observed in *Er1*$^{F/-}$ mice. To test our hypothesis, we first employed a high-throughput mass spectrometry approach in isolated culture media of *Er1*$^{F/+}$ and *Er1*$^{F/-}$ BMDMs (**Figure 13A**). This strategy led to the identification of 329 proteins with 211 proteins (64%) being shared by two independent measurements under stringent selection criteria (**Figure 13B**). At the confidence interval used (p-value: 5x10-11), we find that proteins associated with the presence of (membrane-bound) extracellular vesicles (EVs) and membrane-bound organelles are significantly over-represented (**Figure 13C**) and present with a significantly higher number of known protein interactions (i.e. 178 interactions) than expected by chance (i.e. 109 interactions; P≤8.23x1023; **Figure 13D**) indicating a functionally relevant and interconnected protein network. We identified multiple members of the Ras GTPase superfamily. These low molecular weight proteins are divided into 5 subfamilies, namely Ras, Rab, Rho/Rac, Ran and Arf. They act as molecular switches that integrate extracellular to intracellular signaling and participate in a wide range of cellular processes, including cytoskeletal organization, cell cycle progression, cellular migration and polarity, cell differentiation, survival and apoptosis[143]. The most over-represented protein complex in our results involved several members of the Rab and Rho/Rac subfamilies. The main functions of the Rab proteins involve the regulation of endocytic and secretory pathways, membrane transport and fusion processes, while Rho/Rac GTPases mediate cytoskeletal rearrangement, cellular morphology, migration and cell cycle, as well as transcription and redox signaling[144,145]. Due to their involvement in such diverse and fundamental processes, they have been implicated in many physiological and pathological conditions, including senescence, cancer[146] and inflammatory response[147]. Since those proteins are master regulators of endocytic trafficking, they impact other cellular functions, such as intercellular communication, cellular metabolism and immune response. More specifically, they are involved in vesicle endocytosis and secretion[148], transport and docking of GLUT transporters on plasma membrane[149,150], immune cell differentiation, migration and polarity, as well as cytokine secretion[151,152].

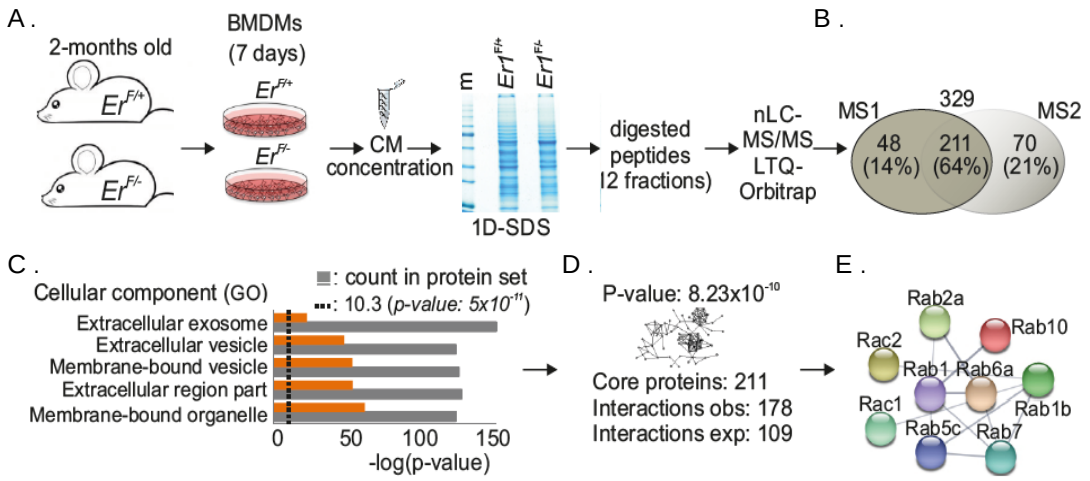


**Figure 13. Proteomic analysis of *Er1*$^{F/-}$ macrophages secretome. (A)** Schematic representation of the high-throughput MS analysis in *Er1*$^{F/-}$ compared to *Er1*$^{F/+}$ BMDMs media. **(B)** Venn's diagram of proteins identified in *Er1*$^{F/-}$ media from two independent biological replicates. **(C)** List of significantly over-represented GO terms associated with Cellular Component. **(D)** Number of observed (obs.) and expected (exp.) known protein interactions within the core 211 shared proteins set. **(E)** Schematic representation of the major protein complex identified in BMDM media.

The central role of the identified proteins in vesicular formation and secretion, together with our previous observations of increased numbers of intracellular vesicles and MVBs in *Er1*$^{F/-}$ BMDMs (**Figure 7I I-VIII**) point to secretion of extracellular vesicles (EVs) by ERCC1 defective macrophages. EVs include a variety of membrane-enclosed structures that, based on their size, biogenesis and secretion mechanism, can be distinguished in exosomes (which originate from the endocytic pathway after fusion of MVBs with cellular membrane, ranging from 30 to 150nm in diameter), microvesicles and apoptotic bodies (both larger, up to 1μm and 5μm, respectively, generated by direct budding of the plasma membrane)[153]. Although at first considered as cellular waste, EVs have emerged as important mediators of intercellular communication. They act as packets of information, conveying a broad variety of biomolecules from one cell to another, either in a paracrine or, through the bloodstream, endocrine manner, thus facilitating systemic crosstalk between distant cell types[154]. Once taken up, EVs can affect the function and fate of the recipient cells. For this reason, they have been endowed with physiological (e.g. developmental processes) and pathological roles (e.g. cancer). For example, senescence, triggered by various stresses (DNA damage, ER stress, hypoxia) has been found to increase EVs secretion[133,155]. Senescent cell-derived EVs act similarly to SASP factors and contribute to the spreading of "protective signals" to neighbouring cells or trigger senescence to bystander cells, inflammation, stem cell dysfunction and cancer progression[156]. In addition, EVs can modulate angiogenesis, tissue repair and immune stimulation or inhibition[157–159]. Finally, circulating EVs levels are enhanced in various metabolic disorders[160] and multiple evidence support a role of EVs (including macrophage-derived EVs) in obesity-associated metabolic disturbances and inflammation[160,161]. To validate our findings, we isolated intact EVs from *Er1*$^{F/+}$ and *Er1*$^{F/-}$ sera and confirmed

our method by detection of the EVs markers CD9 and Alix. We observed increased levels of both proteins in *Er1*$^{F/-}$ sera, together with higher levels of the GTPases RAB10 and RAC1 (**Figure 14A**). The same results were obtained after Western blot of the EVs fraction from *Er1*$^{F/+}$ and *Er1*$^{F/-}$ BMDMs culture media (**Figure 14B**). To further confirm the presence of EVs in the *Er1*$^{F/-}$ BMDMs media, the isolated fraction was processed for electron microscopy. We observed membranous vesicles of size ranging between 30-80nm, which corresponds to that of exosomes, although the presence of larger (≥200nm) cannot be excluded (**Figure 14C**). Further work revealed a similar accumulation of CD9 and Alix in the EV fraction of *Er1*$^{F/-}$ monocytes and neutrophils and a mild to negligible accumulation in the EV fraction of *Ercc1*$^{-/-}$ (designated from now on as *Er1*$^{-/-}$) primary mouse embryonic fibroblasts (MEFs) or the adipocytes, respectively (**Figure 14D**). Confocal microscopy analysis of *Er1*$^{F/+}$ and *Er1*$^{F/-}$ TEMs revealed the accumulation of CD9, as well as of the GTPases RAB10, RAC1 and RAC2 (**Figure 14E**). Finally, we transfected *Er1*$^{F/+}$ and *Er1*$^{F/-}$ macrophages with GFP-tagged CD9. Transiently CD9-GFP macrophages were monitored by live confocal imaging. While *Er1*$^{F/+}$ BMDMs showed static appearance, we observed formation of newly synthesized vesicles and fusion of these vesicular structures with plasma membrane in *Er1*$^{F/-}$ BMDMs (**Figure 14F**). In addition, unlike the sedentary appearance of *Er1*$^{F/+}$ BMDMs, we evidenced, in the case of *Er1*$^{F/-}$ BMDMs, the appearance of protruded pseudopodia (**Figure 14G**).

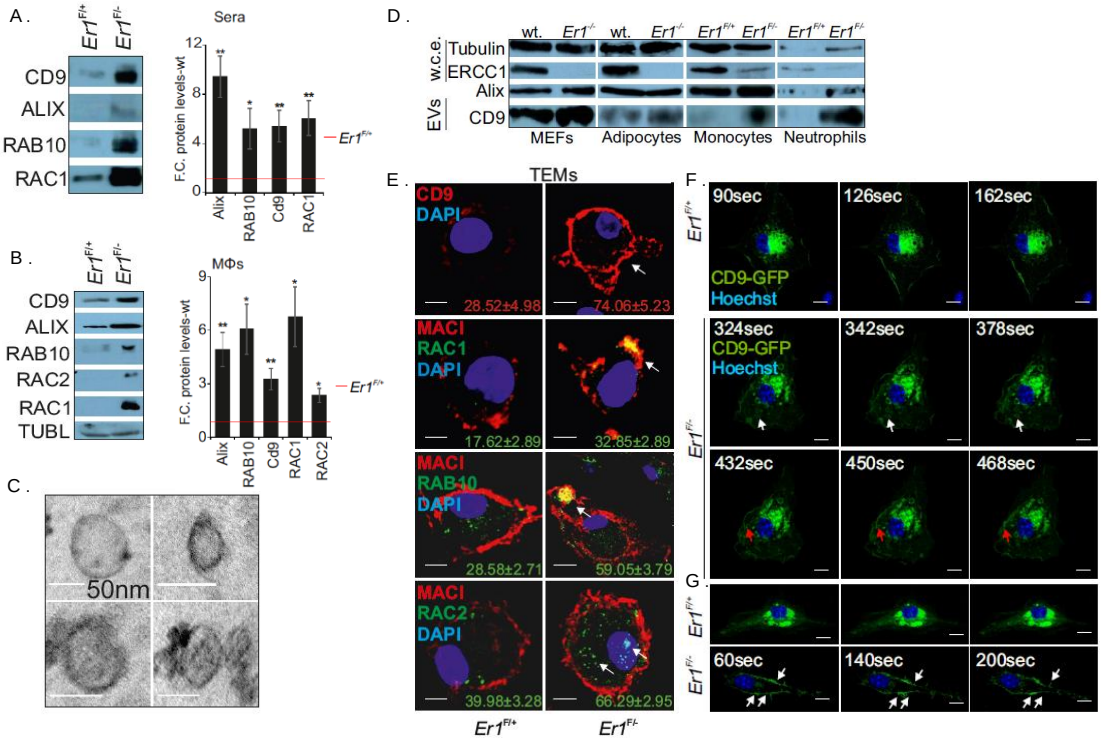

**Figure 14. ERCC1 defect promotes the generation and secretion of extracellular vesicles (EVs). (A)** Western blot analysis of CD9, ALIX, RAB10 and RAC1 proteins levels in the EV fraction of $Er1^{F/-}$ and $Er1^{F/+}$ sera (n=6). The graph shows the western blot fold changes (F.C.) of the indicated proteins (x-axis) in the $Er1^{F/-}$ compared to $Er1^{F/+}$ sera (n=6). **(B)** Western blot analysis of CD9, ALIX, RAB10, RAC2 and RAC1 proteins levels in $Er1^{F/-}$ compared to $Er1^{F/+}$ EV fraction of BMDM media (n=5). The graph shows the western blot fold changes (F.C) of the indicated proteins (x-axis) in the EV fraction of the culture media from $Er1^{F/-}$ macrophages compared to the corresponding fraction of culture media from $Er1^{F/+}$ macrophages (n=5). **(C)** Transmission electron microscopy of EVs marking the presence of exosomes with a size 30-80nm in $Er1^{F/-}$ TEM media. **(D)** Western blotting of ERCC1, Alix , CD9 and tubulin in the EV fraction or in whole cell extracts (w.c.e) of $Ercc1^{-/-}$ ($Er1^{-/-}$ and wt. MEFs or adipocytes and of $Er1^{F/-}$ or $Er1^{F/+}$ monocytes and neutrophils (as indicated). **(E)** Immunofluorescence detection of CD9, RAC1, RAB10 and RAC2 in $Er1^{F/-}$ and $Er1^{F/+}$ thioglycolate-elicited macrophages (TEMs) (n>500 cells per genotype). Colored numbers indicate the average % of positively stained cells +/-SEM for the indicated, color-matched protein. Grey line is set at 5μm scale. **(F)** Live confocal imaging of $Er1^{F/+}$ BMDMs and $Er1^{F/-}$ BMDMs transiently expressing CD9-GFP. The images depict the static appearance of $Er1^{F/+}$ BMDM (upper panel; as indicated), the formation of a newly generated vesicle-like structure in the cytoplasm (white arrowhead) and a fusion event between a vesicle-like structure in the cytoplasm and the cell membrane (red arrowhead) in $Er1^{F/-}$ BMDMs. **(G)** Live confocal imaging of $Er1^{F/+}$ BMDMs and $Er1^{F/-}$ BMDMs transiently expressing CD9-GFP. The images depict the static appearance of $Er1^{F/+}$ BMDM (upper panel; as indicated) and the progressive formation of a protruded pseudopodium in the membrane of $Er1^{F/-}$ BMDMs. Images are generated every 18-20 sec for 10-12 minutes yielding a total of 20-30 frames per movie. Images are representative of a total of at least 20 cells per genotype recorded in 4 independent experiments. Grey line is set at 5μm scale.

To test whether DNA damage is the primary instigator of the EV secretion by $Er1^{F/-}$ macrophages, we exposed $Er1^{F/+}$ macrophages to the genotoxin MMC. In agreement with $Er1^{F/-}$ sera and the EV fraction of $Er1^{F/-}$ macrophage media, the EVs markers and the GTPases levels were enriched in MMC-treated EVs fraction compared to that of the untreated BMDMs (**Figure 15A**). Inactivation of DDR by inhibition of ATM or ATR in MMC-treated macrophages dampened the MMC-induced increase of CD9, Alix and the GTPases RAB10, RAC1 and RAC2 protein levels (**Figure 15A-B**). The direct correlation between DNA damage and EV secretion was further supported by the parallel increase of γH2AX, CD9 and Alix protein levels in $Er1^{+/+}$, $Er1^{+/-}$ and $Er1^{-/-}$ BMDMs, both in WCE and the EVs fraction, as seen by Western blotting (**Figure 15C**). Finally, we employed an ELISA-based immunoassay, to detect low abundance proteins (<100ng/ml) in $Er1^{F/+}$ and $Er1^{F/-}$ sera and culture media of macrophages, since such low concentrations cannot be efficiently identified with current mass spectrometry protocols. The results showed increased levels of the proinflammatory cytokines IL6 and IL8, while the protein levels of other factors tested (IL1, MCP-1, IFN-γ) were either undetectable or similar between the two genotypes (**Figure 15D**). Altogether, our results show that ERCC1 defect in macrophages and the subsequent activation of DDR lead to increased levels of GTPases, formation and secretion of EVs, together with secretion of proinflammatory cytokines. To test whether the increase in GTPases levels are functionally related to increased biogenesis and secretion of EVs by $Er1^{F/-}$

macrophages, we transfected *Er1*$^{F/+}$ macrophages with GFP-tagged RAB10 (R10) and GFP-tagged RAC1 or GFP alone. Western blot analysis of *Er1*$^{F/+}$, *Er1*$^{F/-}$ and transfected *Er1*$^{F/+}$ macrophages verified the expression of the GFP-tagged proteins, together with the increased expression levels of the EVs markers CD9 and Alix (**Figure 15E**). Furthermore, treatment of the *Er1*$^{F/-}$ macrophages with the RAC1 inhibitor NSC 23766 for 16h resulted in the reduction of CD9 to the levels detected in *Er1*$^{F/+}$ macrophages (**Figure 15F**). Thus, in accordance to published data on the role of GTPases in vesicular trafficking and secretion, the increased levels of GTPases in DNA repair deficient macrophages facilitate the induction of EVs secretion.

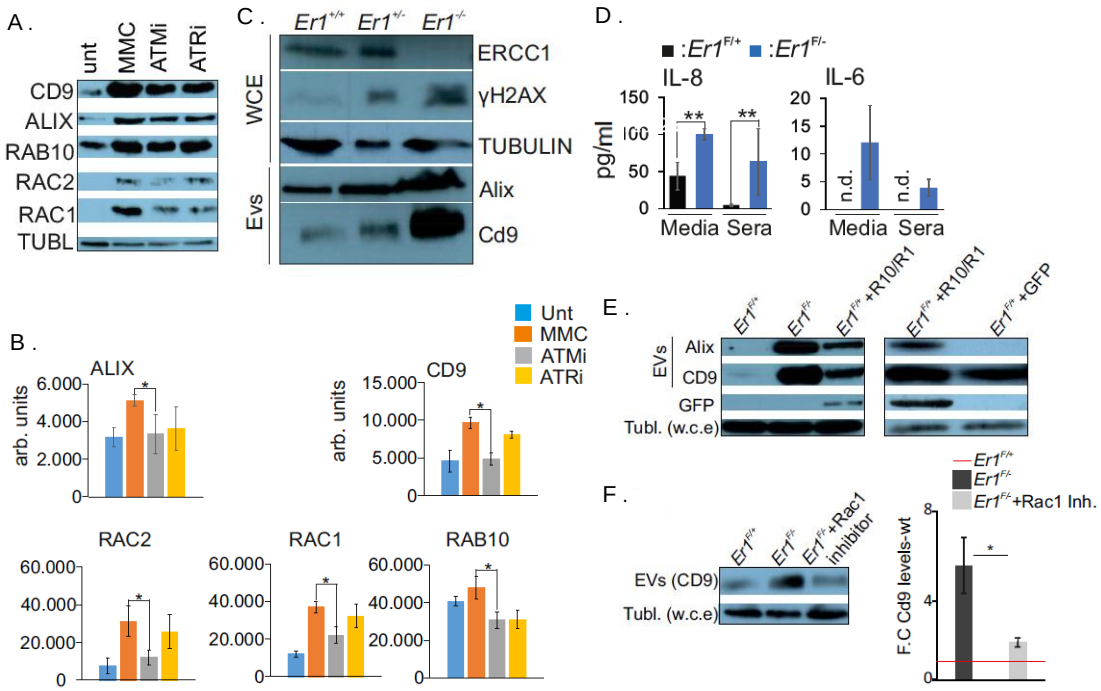


**Figure 15. DNA damage promotes the generation and secretion of extracellular vesicles (EVs) in *Er1*$^{F/-}$ macrophages. (A)** Western blot analysis of CD9, ALIX, RAB10, RAC2 and RAC1 proteins levels in the EV fraction of media derived from the MMC-treated and control BMDMs exposed to ATM (ATMi) or ATR (ATRi) inhibitors (as indicated; n=3 independent experiments). **(B)** Quantitative measurement (arbitrary; arb. units) of ALIX, CD9, RAC2, RAC1 and RAB10 protein levels as measured in the EV fraction of MMC-treated and control BMDMs exposed to ATM (ATMi) or ATR (ATRi) inhibitors (n=3). **(C)** Western blotting of γH2Ax, ERCC1 and tubulin in whole cell extracts (WCE) or ALIX and CD9 in the EV fraction of Er1$^{+/+}$, Er1$^{+/-}$ and *Er1*$^{-/-}$ BMDMs or culture media, respectively. **(D)** IL8 and IL6 protein levels in *Er1*$^{F/-}$ and *Er1*$^{F/+}$ sera and BMDM media (as indicated). **(E)** Western blotting of Alix, CD9 and the GFP in EVs and tubulin (Tubl.) in whole cell extracts (w.c.e.) of *Er1*$^{F/-}$, *Er1*$^{F/+}$ and *Er1*$^{F/+}$ macrophages transfected with GFP-tagged RAC1 (R1) and GFP-tagged RAB10 (R10) or GFP alone (as indicated). **(F)** Western blotting of CD9 in the EV fraction and tubulin in whole cell extracts of *Er1*$^{F/+}$, *Er1*$^{F/-}$ and *Er1*$^{F/-}$ treated with NSC23766, 16hrs (50μM Rac1 inhibitor). Graph shows quantification of western blot (n=3).

### *Er1*$^{F/-}$ macrophage-derived EVs trigger the glucose uptake in recipient cells

Next, we aimed to investigate the fate of the macrophage-secreted EVs. Confocal microscopy studies revealed increased GTPases protein levels in primary pancreatic cells (PPCs) and hepatocytes from *Er1*$^{F/-}$ mice (**Figure 16A**). To verify the macrophage origin of these GTPases, we performed a series of *in vitro* assays. First, we isolated EVs from *Er1*$^{F/-}$ macrophage culture media (*Er1*$^{F/-}$ EVs) and labeled them with the lipophilic green fluorescent dye PKH67. The labeled EVs were added in the culture media of PPCs. We then conducted confocal imaging of the cells and detected the presence of green-fluorescent EVs in the cytoplasm of PPCs (**Figure 16B**). To further confirm that macrophage-derived EVs deliver their cargo in the recipient cells, we transfected *Er1*$^{F/-}$ macrophages with GFP-tagged RAB10 or RAC1 (**Figure 16C**) and isolated the EVs from their media. Those *Er1*$^{F/-}$ EVs carrying the GFP-tagged GTPases were then added in the culture media of PPCs and the cells were observed with confocal microscopy. The results showed the presence of GFP fluorescence, and thus of the tagged GTPases, in the cytoplasm of the PPCs (**Figure 16D**).

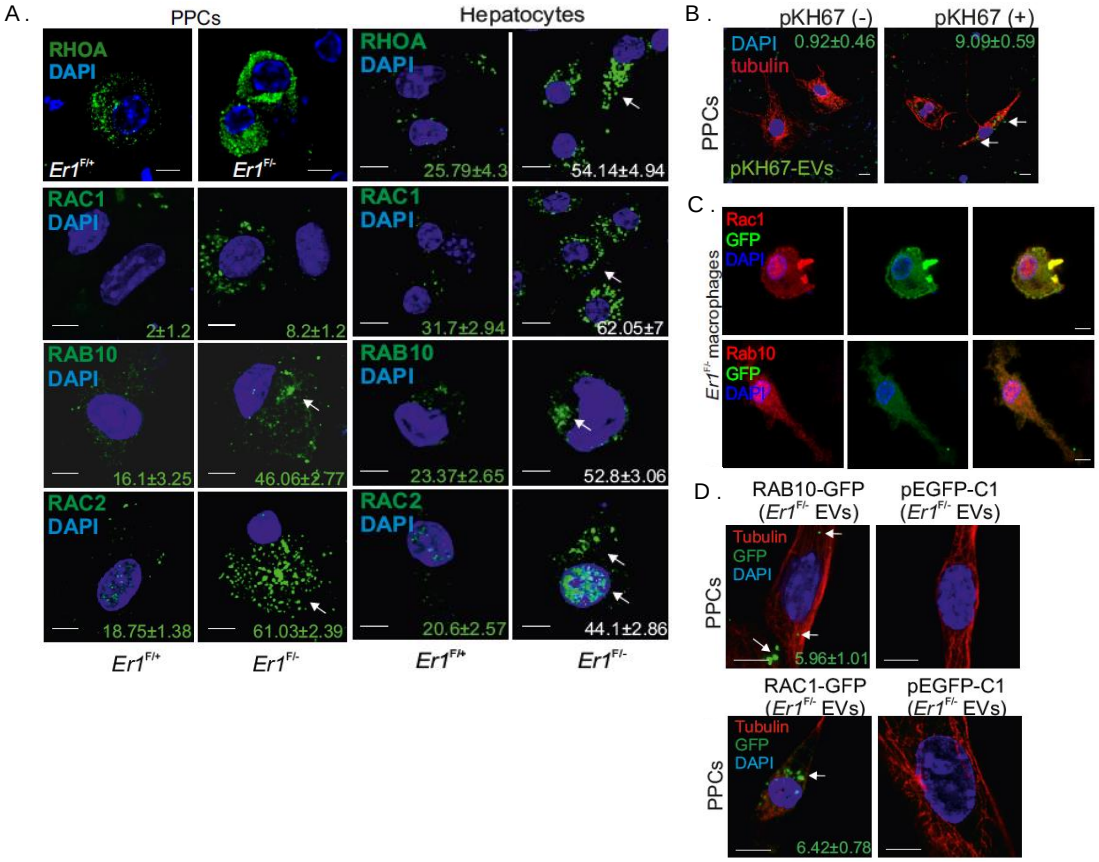


**Figure 16. *Er1*$^{F/-}$ macrophage-derived EVs efficiently deliver their cargo in the recipient cells. (A)** Immunofluorescence detection of RAC1 (~500 cells per genotype), RAB10 (~150 cells per genotype) and RAC2 (~150 cells per genotype) in *Er1*$^{F/-}$ and *Er1*$^{F/+}$ PPCs (n>400 cells per genotype) and hepatocytes (n>100 cells per genotype) The numbers indicate the average % of positively stained cells +/-SEM for the indicated protein. Grey line is set at 5μm scale. **(B)** Immunofluorescence detection of the lipophilic green fluorescent dye PKH67 in PPCs; the white-colored arrowhead

depicts the presence of pKH67-labelled EVs in PPCs. Numbers indicate the average % of positive cells +/- SEM (n>800 cells counted in three independent experiments). **(C)** Immunofluorescence detection of GFP-tagged RAC1 and GFP-tagged RAB10 in *Er1*$^{F/-}$ macrophages. **(D)** Immunofluorescence detection of RAB10-GFP (indicated by the white-colored arrowhead) and RAC1-GFP (indicated by the white-colored arrowhead) in PPCs treated with EVs from *Er1*$^{F/-}$ BMDMs transfected with RAB10-GFP or RAC1-GFP. Colored numbers indicate the average percentage of positively stained cells +/ SEM for the indicated, color-matched protein. (n> 700 cells counted in three independent experiments).

Since multiple members of the RAS GTPases superfamily have been also implicated in glucose uptake through the trafficking of GLUT transporters to plasma membrane[149,150], together with our findings of altered glucose homeostasis in *Er1*$^{F/-}$ mice, we reasoned that the *Er1*$^{F/-}$ macrophage-derived EVs could trigger the glucose uptake by the recipient cells. To monitor the uptake of glucose by macrophage EV-targeted cells, we employed the fluorescent glucose analogue 2-NBDG. More specifically, treatment of PPCs or hepatocytes with *Er1*$^{F/-}$ EVs resulted in noticeable uptake of 2-NBDG, compared to respective treatment with *Er1*$^{F/+}$ EVs (**Figure 17A**). We found similar findings when PPCs were incubated with the EV fraction of *Er1*$^{F/-}$ mouse serum (ser. *Er1*$^{F/-}$ EVs) (**Figure 17B**) or with EVs from MMC-treated *Er1*$^{F/-}$ macrophages media (**Figure 17C**).

Large polar molecules such as glucose cannot passively penetrate the plasma membrane. They can be transferred inside the cell through specialized transporters, in this case the GLUT transporters. Of the 14 different GLUTs, GLUT1-4 are the most well studied transporters. GLUT1 and 3 are expressed in most tissues, with GLUT1 being upregulated also in cancer cells and GLUT3 expressed in monocytes/macrophages[162]. In addition, GLUT1 has been shown to transfer glucose inside the cells independently of insulin[163]. To test if the glucose uptake triggered by *Er1*$^{F/-}$ EVs is mediated by GLUTs, we exposed PPCs to either *Er1*$^{F/+,}$ *Er1*$^{F/-}$ or MMC-treated macrophage EVs and measured the mRNA and protein levels of GLUTs. GLUT1 was undetectable 3 hours after the exposure of PPCs to the EVs, both at mRNA (**Figure 17D**) and protein levels (**Figure 17H**, upper panel). However, within 24 hours mRNA (**Figure 17E**) and protein levels of GLUT1 gradually accumulated in the PPCs exposed to *Er1*$^{F/-}$ and MMC-EVs (**Figure 17F-H**). GLUT3 protein levels were also increased 24 hours after the treatment of PPCs with *Er1*$^{F/-}$ EVs (**Figure 17F**). In addition, phosphorylated (S226) GLUT1, a modification that facilitates glucose transport[164], also accumulated in PPCs exposed to *Er1*$^{F/-}$ and MMC-EVs (**Figure 17I**). In contrast to GLUT1, RAB10 rapidly accumulated in PPCs within 3 hours of exposure of the cells to *Er1*$^{F/-}$ and MMC-EVs (**Figure 17J**) and it was still detectable, together with GLUT1, 24 hours after exposure to the same EVs (**Figure 17K**). Finally, we analyzed the metabolic state of PPCs exposed to macrophage-derived *Er1*$^{F/+,}$ *Er1*$^{F/-}$ or MMC EVs or *Er1*$^{F/+,}$ *Er1*$^{F/-}$ mouse sera EVs, by an oxygen consumption rate (OCR) protocol[165]. We detected a mild but reproducible increase in OCR in PPCs treated with *Er1*$^{F/-}$ EVs, MMC EVs and *Er1*$^{F/-}$ ser. EVs, compared to those exposed to (ser) *Er1*$^{F/+}$ EVs (**Figure 17L**). To test these effects *in vivo*, we detected GLUT levels in *Er1*$^{F/+}$ and *Er1*$^{F/-}$ mice tissues. Western blot analysis (**Figure 17M**) and confocal

microscopy studies (**Figure 17N**) revealed accumulation of GLUT1 and 3 in 6-months old *Er1*$^{F/-}$ pancreata and livers. In addition, co-staining of GLUT3 and PECAM revealed increased GLUT3 expression in pancreas, livers and WAT of *Er1*$^{F/-}$ animals, that was not restricted to endothelial cells, but also expanded to other cell types (**Figure 17O**). Overall, our data indicate that *Er1*$^{F/-}$ macrophages secrete EVs that transfer their cargo, including GTPases, in other cell types, leading to accumulation of GLUTs and glucose uptake, altering their metabolic status.

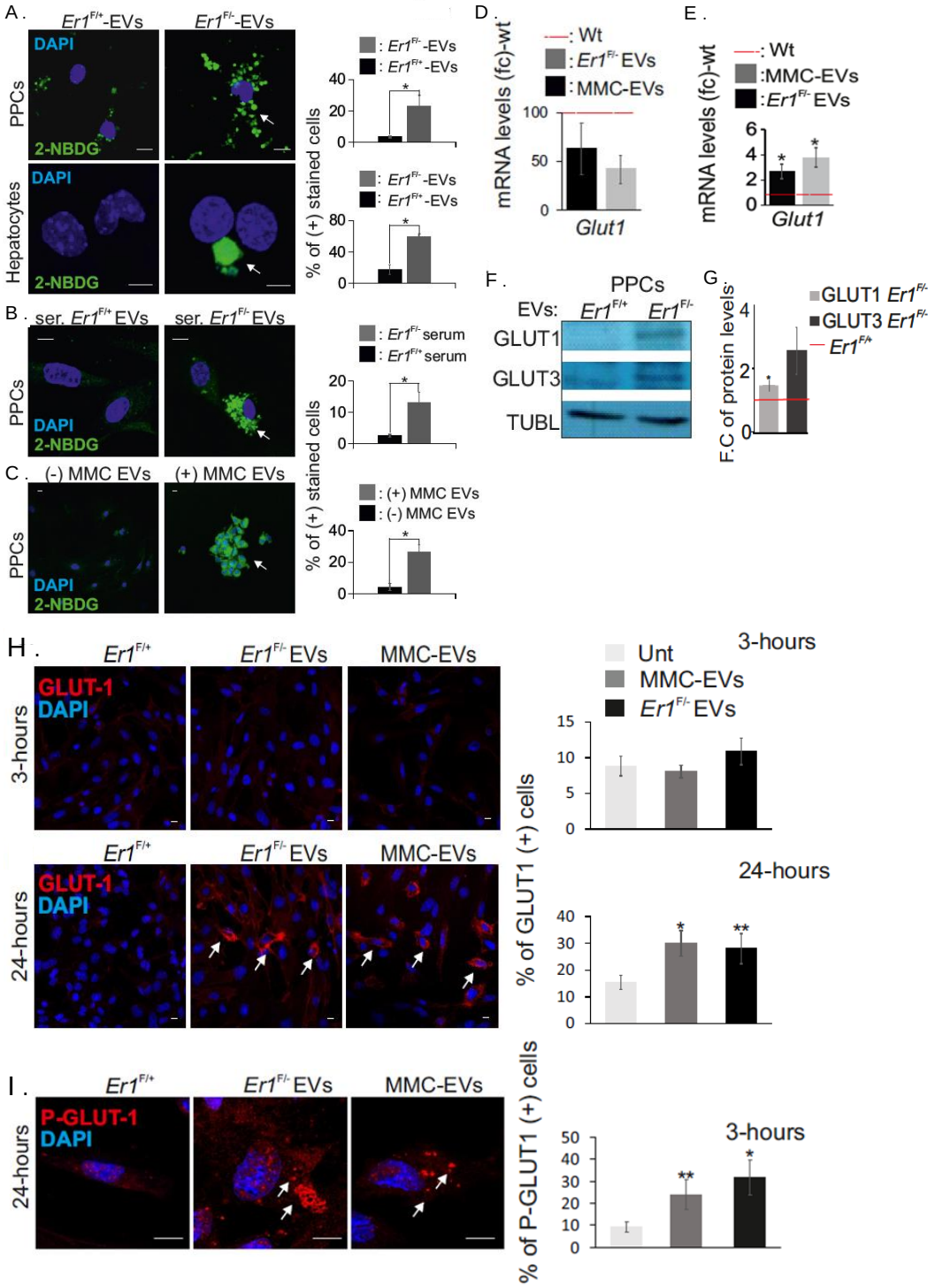

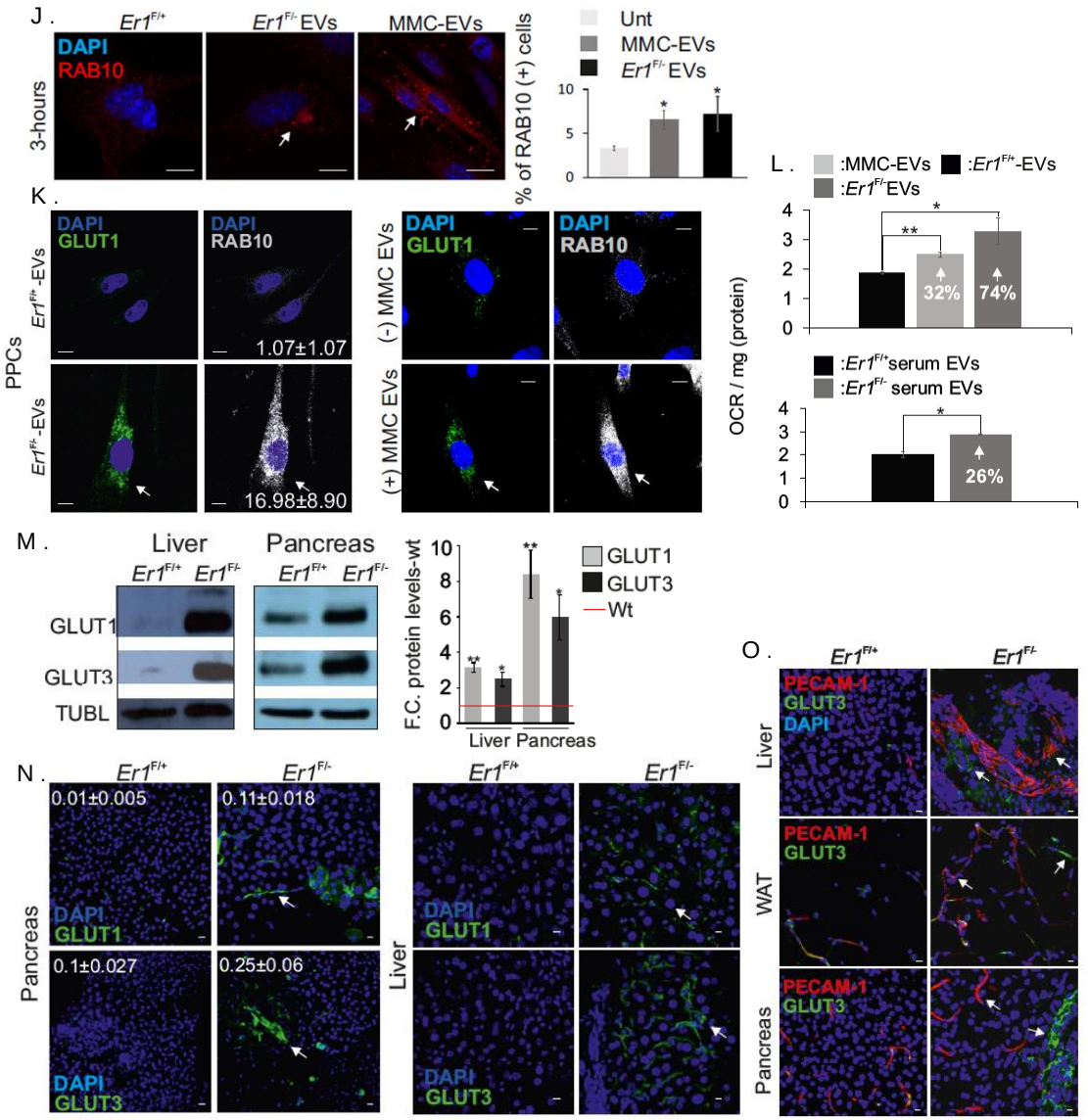


**Figure 17. *Er1*$^{F/-}$ macrophage-derived EVs trigger the uptake of glucose in recipient cells. (A)** Immunofluorescence detection of fluorescent tracer 2-NBDG for the monitoring of glucose uptake in PPCs (~2500 cells per genotype) and hepatocytes (~250 cells per genotype) exposed to *Er1*$^{F/-}$ and *Er1*$^{F/+}$-derived EVs (as indicated). **(B)** Immunofluorescence detection of fluorescent tracer 2-NBDG for the monitoring of glucose uptake in PPCs exposed to *Er1*$^{F/-}$ and *Er1*$^{F/+}$ EVs derived from animal sera (ser.; n>700 cells per genotype) or to **(C)** MMC EVs (as indicated, n>2000 cells per treatment). **(D)** *Glut1* mRNA levels (fc; fold change) in PPCs exposed to EVs derived from *Er1*$^{F/-}$ (*Er1*$^{F/-}$ EVs) or MMC-treated (MMC-EVs) macrophages compared to untreated wt. macrophages (red dotted line) for 3hrs. **(E)** *Glut1* mRNA levels in PPCs exposed to EVs derived from *Er1*$^{F/-}$ EVs or MMC-EVs macrophages compared to untreated wt. macrophages (red dotted line) for 24hrs. **(F)** Western blotting of GLUT1 and GLUT3 protein levels in PPCs exposed to *Er1*$^{F/-}$ and *Er1*$^{F/+}$-derived EVs (n=4). **(G)** Graph showing the fold change and statistical significance of GLUT1 and GLUT3 protein levels in primary pancreatic cells exposed to *Er1*$^{F/-}$ or *Er1*$^{F/+}$ EVs (n=4). **(H)** Immunofluorescence detection of GLUT1 in PPCs exposed to EVs derived from *Er1*$^{F/+}$ (*Er1*$^{F/+}$ EVs), *Er1*$^{F/-}$ (*Er1*$^{F/-}$ EVs) or MMC-treated EVs (MMC-EVs) for 3- or 24- hours (as indicated). **(I)** Immunofluorescence detection of P-GLUT1 in PPCs exposed to *Er1*$^{F/+}$ EVs, *Er1*$^{F/-}$ EVs or to MMC-EVs for 24hours. **(J)** Immunofluorescence detection

of RAB10 in PPCs exposed to *Er1*$^{F/+}$ EVs, *Er1*$^{F/-}$ EVs or to MMC-EVs for 3 hours. **(K)** Immunofluorescence detection of GLUT1 and RAB10 in PPCs exposed to *Er1*$^{F/-}$ and *Er1*$^{F/+}$-derived EVs. White colored numbers indicate the average % of GLUT1, RAB10 double positive cells in each experimental condition (n>200 cells counted in three independent experiments) (Left panel). Immunofluorescence detection of GLUT1 and RAB10 in PPCs exposed to MMC-EVs for 24hours (n> 200 cells were counted in at least 5 optical fields) (Left panel). The graph shown in Figure 15J shows the % of positively stained cells per condition. **(L)** Oxygen consumption rate (OCR) of PPCs maintained in the presence of 15mmol glucose that were exposed to *Er1*$^{F/+}$, *Er1*$^{F/-}$ or MMC-treated, macrophage-derived EVs (upper panel) and to *Er1*$^{F/+}$ or *Er1*$^{F/-}$ serum-derived EVs (lower panel); white colored numbers indicate the % increase in OCR compared to corresponding controls. **(M)** Western blotting of GLUT1 and GLUT3 protein levels in *Er1*$^{F/-}$ and *Er1*$^{F/+}$ liver and pancreata (n=3). The graph shows the corresponding fold change (F.C) and statistical significance of GLUT1 and GLUT3 protein levels. **(N)** Immunofluorescence detection of GLUT1 and GLUT3 in the pancreas of *Er1*$^{F/-}$ and *Er1*$^{F/+}$ mice (n=3, 2-3 optical fields per animal). White colored numbers indicate the average mean fluorescence intensity. Grey line is set at 10μm scale. **(O)** Immunofluorescence detection of PECAM-1 and GLUT3 (shown by the arrowhead) in *Er1*$^{F/-}$ and *Er1*$^{F/+}$ livers, white adipose tissue (WAT) and pancreata. Grey line is set at 10 scale.

## *Er1*$^{F/-}$ EVs-triggered glucose uptake activates innate immune signaling

We have shown that *Er1*$^{F/-}$ macrophages secrete EVs that stimulate the glucose uptake by recipient cells. In addition, they lead to systemic alterations of glucose metabolism, together with elevated levels of inflammation in *Er1*$^{F/-}$ mice. It is known that glucose and high-glycemic diets are associated with activation of inflammatory processes during metabolic abnormalities, through activation of NFκB[166–168]. In addition, high glucose has been shown to potentiate inflammatory gene expression[169]. We thus investigated whether the inflammatory responses seen in *Er1*$^{F/-}$ mice are mediated by the increased glucose uptake by various metabolically active tissues (e.g. pancreas). To discriminate between the effects triggered by EVs or by the additional proinflammatory factors in the media (IL6, IL8), we incubated PPCs with *Er1*$^{F/+}$, *Er1*$^{F/-}$ or MMC-treated conditioned media (CM) alone (devoid of EVs), EVs alone or unprocessed CM, containing the EV fraction and tested the cells for proinflammatory factors. We observed a combined effect of CM alone and EVs alone treatments, since combined CM and EVs from *Er1*$^{F/-}$ and MMC-treated macrophages could trigger accumulation of the proinflammatory factor iNOS in PPCs (**Figure 18A-C**). Similarly, translocation of NFκB to the nucleus, which stimulates the transcription of proinflammatory genes, is triggered after treatment of PPCs with *Er1*$^{F/-}$ and MMC CM containing the EVs (**Figure 18D-F**), although a substantial nuclear NFκB translocation was also triggered by exposure to *Er1*$^{F/-}$ and MMC CM or EVs alone. Thus, PPCs activate a proinflammatory signaling in response to the cytokines and EVs secreted by DNA repair deficient macrophages. To test if this response is mediated by the glucose uptake, PPCs exposed to *Er1*$^{F/-}$ and MMC CM containing the EVs were cultured under low (5mmol) or high (15mmol) glucose concentration. We found that both iNOS levels (**Figure 18G-H**) and NFκB nuclear accumulation (**Figure 18I-J**) were more profound in PPCs maintained at the higher glucose concentration (15mmol), upon *Er1*$^{F/-}$ and MMC CM+EVs exposure. Overall, we have shown that EVs from macrophages carrying DNA damage trigger the

glucose uptake by other cell types and this response potentiates inflammatory responses.

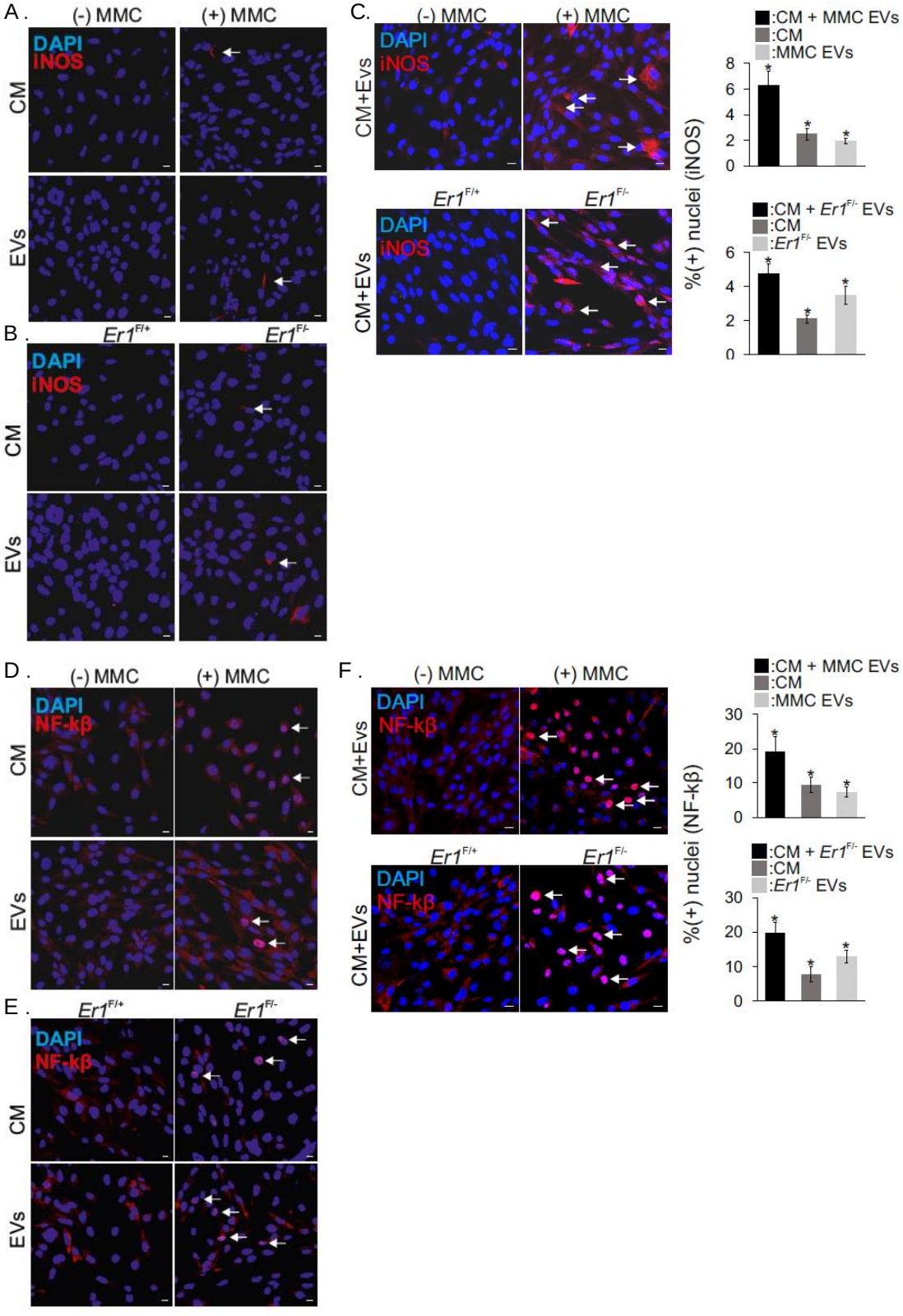

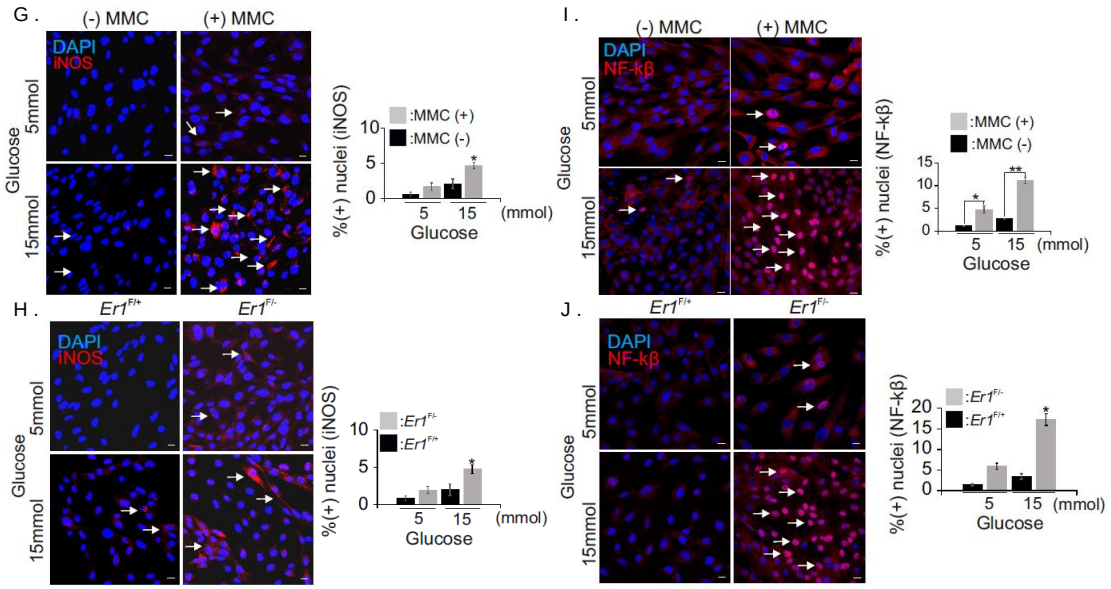


**Figure 18. Glucose uptake activates pro-inflammatory responses in EV-recipient cells. (A)** Immunofluorescence detection of iNOS in PPCs exposed to culture media (CM) devoid of EVs or only the EVs derived from MMC treated (MMC+) and untreated (MMC-) or **(B)** *Er1*$^{F/-}$ and *Er1*$^{F/+}$ BMDMs. **(C)** Immunofluorescence detection of iNOS accumulation (indicated by the arrowhead) in PPCs exposed to culture media (CM) and the EVs derived from MMC-treated and untreated control macrophages (n=3, >600 cells per treatment) or *Er1*$^{F/-}$ and *Er1*$^{F/+}$ macrophages (n=3, >1200 cells/treatment). **(D)** Immunofluorescence detection of NF-kβ in PPCs exposed to culture media (CM) devoid of EVs or only the EVs derived from MMC treated (MMC+) and untreated (MMC-) or **(E)** *Er1*$^{F/-}$ and *Er1*$^{F/+}$ BMDMs. **(F)** Immunofluorescence detection of NF-kβ nuclear translocation (indicated by the arrowhead) in PPCs exposed to CM and the EVs derived from MMC-treated and untreated control macrophages (n=3, >700 cells per treatment) or *Er1*$^{F/-}$ and *Er1*$^{F/+}$ macrophages (n=3, >500 cells per treatment). **(G)** Immunofluorescence detection of iNOS in PPCs exposed to culture media (CM) and EVs derived from MMC-treated and untreated BMDMs or **(H)** from *Er1*$^{F/-}$ and *Er1*$^{F/+}$ BMDMs upon low (5mmol) and high (15mmol) glucose concentration. **(I)** Immunofluorescence detection of NF-kβ (shown by the arrowhead) in PPCs exposed to CM supplemented with EVs from MMC-treated and control macrophages or **(J)** from *Er1*$^{F/-}$ and *Er1*$^{F/+}$ BMDMs upon low (5mmol) or high (15mmol) glucose concentration. The graphs show the % of positively stained cells per condition (>200 cells were counted in at least 5 optical fields in each condition). Error bars indicate S.E.M. (n ≥ 3). Asterisk indicates the significance set at p-value: *≤0.05, **≤0.01 (two-tailed Student's t-test). Grey line is set at 5μm scale.

We then studied the molecular mechanism that links the glucose uptake and the inflammatory response. The PI3K/AKT/mTOR network is a signaling pathway that integrates external cues and regulates the respective cellular responses, including the metabolic pathways and responses, such as glucose uptake[170]. In addition, mTOR pathway has been found to balance anabolism and catabolism in response to environmental signals, for example by regulating GLUT3 expression in an NFκB-dependent manner[171,172]. We detected increased levels of the phosphorylated eukaryotic translation initiation factor 4E (eIF4E)-binding protein 1 (p4E-BP1), a translational repressor and well-known target of mTOR pathway, in *Er1*$^{F/-}$ pancreata (**Figure 19A**). Inhibition of mTOR by rapamycin abrogated the increase of p4E-BP1 protein levels and iNOS

accumulation triggered by MMC treatment of macrophages (**Figure 19B**). Additionally, mTOR inhibition reduced the nuclear accumulation of NFκB in PPCs exposed to *Er1*$^{F/-}$ EVs, without affecting glucose uptake (**Figure 19C**). Hence, mTOR pathway is activated in *Er1*$^{F/-}$ or MMC EVs-recipient cells and acts downstream of glucose uptake so as to regulate the activation of immune signaling.

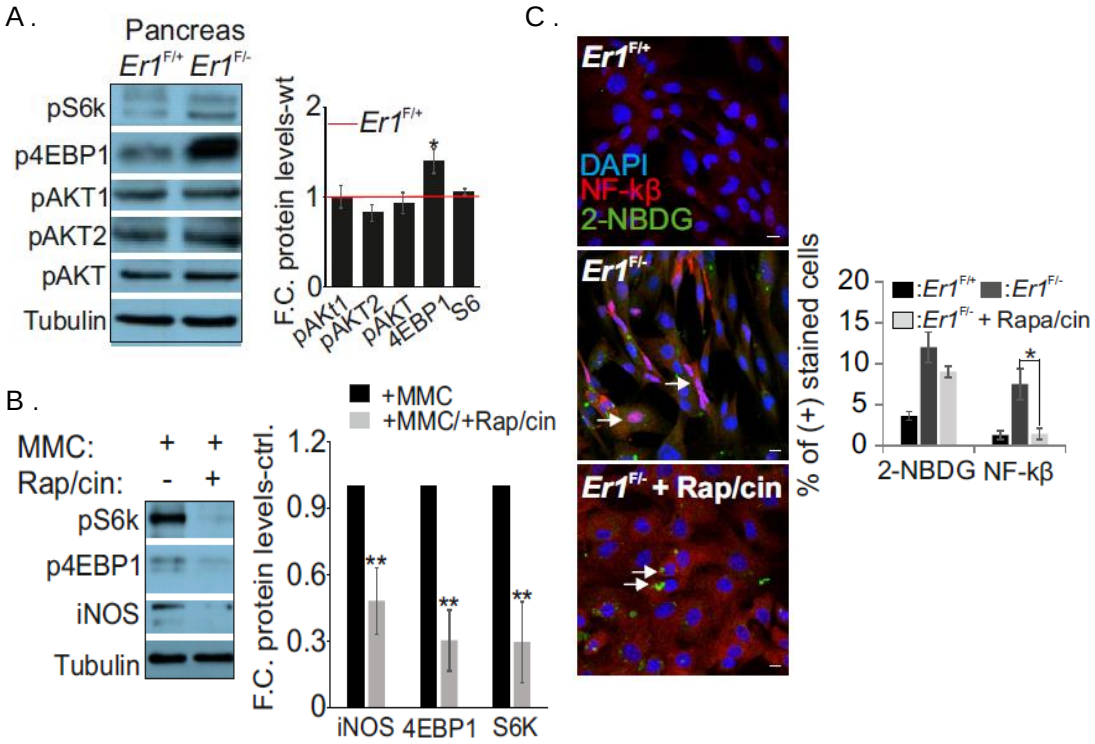


**Figure 19. EV-triggered pro-inflammatory responses in EV-recipient cells are rapamycin sensitive. (A)** Western blotting of phosphorylated pS6K, phosphorylated p4EBP1, phosphorylated pAKT1, phosphorylated pAKT2 and phosphorylated pAKT protein levels in *Er1*$^{F/-}$ and *Er1*$^{F/+}$ pancreata (n=4). The graph represents the fold change (F.C) of indicated protein levels in *Er1*$^{F/-}$ pancreata to wt. controls. **(B)** Western blotting of pS6K, p4EBP1 and iNOS protein levels in MMC-treated macrophages exposed to rapamycin (n=3, Rap/cin; as indicated). The graph represents the fold change of protein levels in MMC-treated macrophages exposed to rapamycin compared to MMC-treated macrophage control (ctrl.) cells. **(C)** Immunofluorescence detection of NF-kβ and 2-NBDG in PPCs (indicated by the arrowheads) exposed to CM supplemented with EVs derived from *Er1*$^{F/-}$ and *Er1*$^{F/+}$ BMDMs in the presence or absence of rapamycin (Rap/cin). (n=6, >1000 cells counted per treatment). The graph shows the % of positively stained cells. Error bars indicate S.E.M. among replicates (n ≥ 3). Asterisk indicates the significance set at p-value: *≤0.05, **≤0.01 (two-tailed Student's t-test). Grey line is set at 5μm scale.

## Effects of exogenous *Er1$^{F/-}$* EVs *in vivo*

So far, we have studied the effects of *Er1$^{F/-}$* macrophage-derived EVs on the immune and metabolic signaling in recipient cells. To test the *in vivo* relevance of our findings, we injected B6 C57BL/6 mice with EVs derived from either *Er1$^{-/-}$* and WT mouse embryonic fibroblasts (MEFs) or *Er1$^{F/+}$* and *Er1$^{F/-}$* macrophages. The injections were performed intravenously every 24 hours for a period of 10 days. In contrast to mice injected with *Er1$^{-/-}$* MEFs-, WT MEFs- or *Er1$^{F/+}$* macrophage-derived EVs, intravenous injection of mice with *Er1$^{F/-}$* macrophage-derived EVs resulted in pronounced accumulation of macrophages in the liver, together with an upregulation of GLUT1 levels (**Figure 20A**). Western blot analysis confirmed the increased GLUT protein levels in liver, as well as in muscle protein extracts from mice treated with *Er1$^{F/-}$* macrophage-derived EVs, but not with EVs from WT MEFs, *Er1$^{-/-}$* MEFs or *Er1$^{F/+}$* macrophage (**Figure 20B**). Furthermore, injection of *Er1$^{F/-}$* macrophage-derived EVs enhanced the glucose tolerance of the mice during GTT compared to the corresponding controls, while injection of *Er1$^{-/-}$* MEFs-derived EVs did not affect the response of the mice to glucose, which was almost identical to those of mice injected with WT MEFs-derived EVs (**Figure 20C**). Finally, to test the tissue-specificity of the responses observed, we treated WT PPCs with EVs derived from *Er1$^{F/+}$* or *Er1$^{F/-}$* macrophage or monocytes and EVs from WT or *Er1$^{-/-}$* adipocytes or MEFs. The results showed that only treatment with the *Er1$^{F/-}$* macrophage-derived EVs lead to GLUT1 and iNOS accumulation (*Er1$^{F/-}$* monocyte-derived EVs also triggered a slight increase in iNOS levels) (Figure 18D), as well as uptake of 2-NBDG (**Figure 20E**). Thus, the ERCC1 defect in macrophages triggers a cell-specific response in macrophages that, through the secretion of EVs, triggers increased glucose uptake by the recipient tissue cells and the upregulation of inflammatory signaling, ultimately leading to a systemic metabolic response and reprogramming.

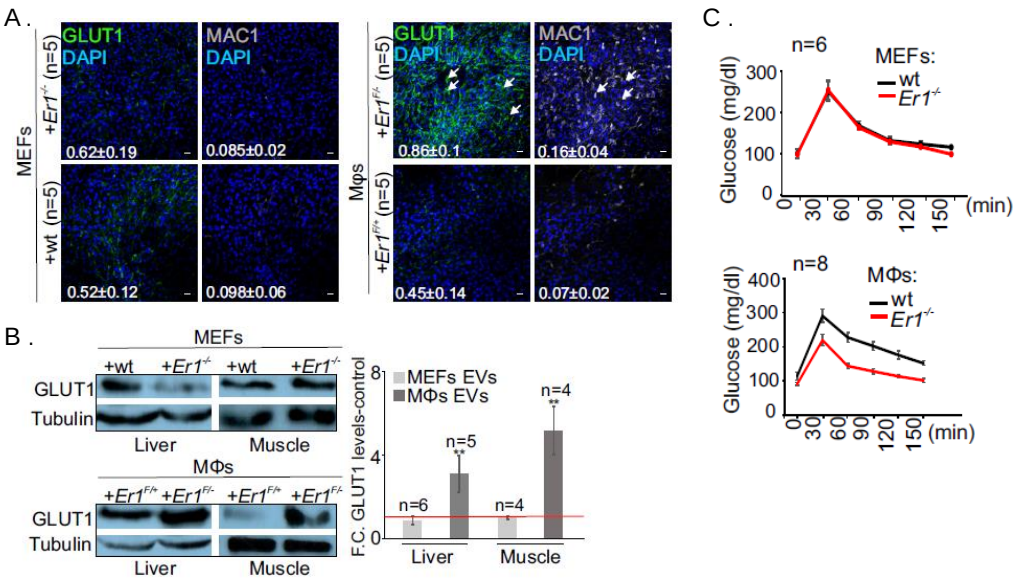

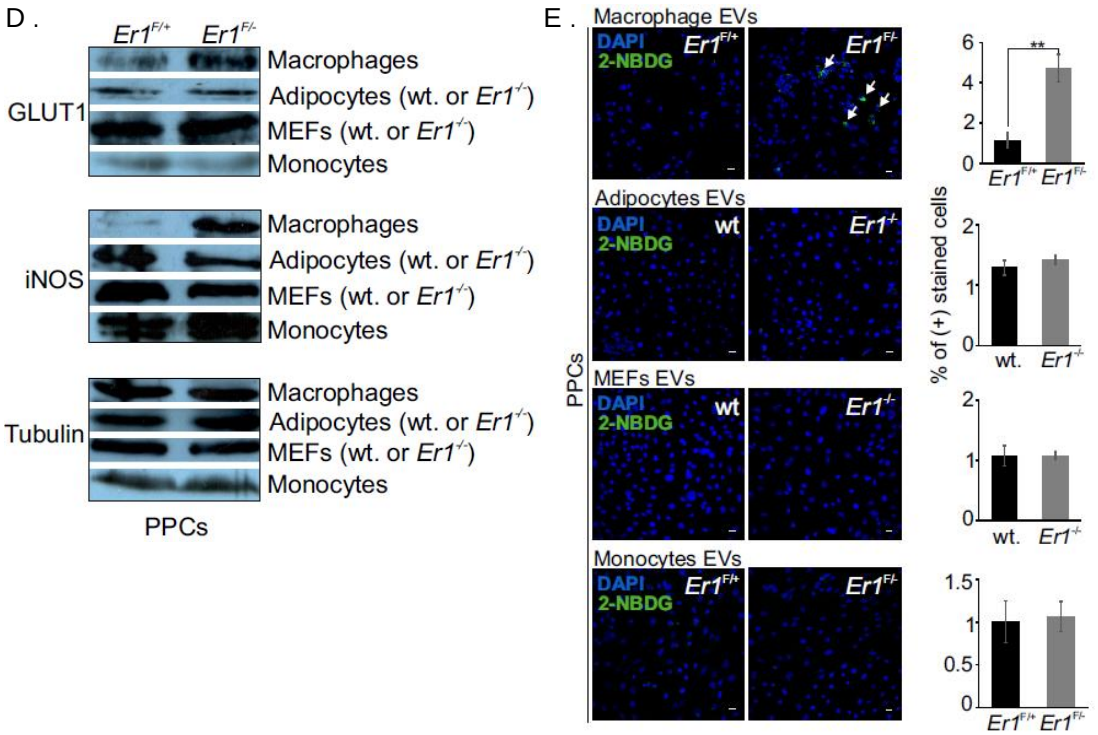


**Figure 20. Exogenous delivery of Er1F/- exosomes promote GLUT1 accumulation, glucose uptake and inflammation in vivo. (A)** Immunofluorescence detection of GLUT1 in the liver of 4-weeks old C57BL/6 animals intravenously injected with EVs derived from either *Er1*$^{-/-}$ or wt. MEFs (left panel) and *Er1*$^{F/+}$ or *Er1*$^{F/-}$ macrophages (right panel). Numbers show average mean fluorescence intensity +/- SEM, n=4 animals per genotype, >3 optical fields/animal. **(B)** Western blotting of GLUT1 in the muscle and liver of C57BL/6 animals intravenously injected with EVs derived from either *Er1*$^{-/-}$ or wt. MEFs (upper panel) and *Er1*$^{F/+}$ or *Er1*$^{F/-}$ macrophages (lower panel). The graph represents the fold change (F. C) of GLUT1 protein levels in the liver or muscle tissues of animals treated with *Er1*$^{-/-}$ MEF or *Er1*$^{F/-}$ macrophage–derived EVs as compared to corresponding tissues of animals treated with *Er1*$^{+/+}$ MEFs or *Er1*$^{F/+}$ macrophage-derived EVs. **(C)** Glucose tolerance test (GTT) graphs of C57BL/6 mice injected intraperitoneally every 24 hours for a period of 10 days with EVs derived from either *Er1*$^{-/-}$ or wt. MEFs (n=6) and *Er1*$^{F/+}$ or *Er1*$^{F/-}$ macrophages (n=8) (as indicated). **(D)** Western blotting of GLUT1, iNOS and Tubulin in PPCs exposed to EVs derived from *Er1*$^{F/-}$ and *Er1*$^{F/+}$ macrophages or monocytes and from *Ercc1*$^{-/-}$ (*Er1*$^{-/-}$) and wt. adipocytes or MEFs (as indicated). **(E)** Immunofluorescence detection of 2-NBDG in PPCs exposed to EVs derived from *Er1*$^{F/-}$ or *Er1*$^{F/+}$ macrophages or monocytes and from *Ercc1*$^{-/-}$ (*Er1*$^{-/-}$) and wt. MEFs or adipocytes (as indicated). The graphs show the percentage of positively stained cells per condition (>500 cells were counted in at least 5 optical fields in each condition). Error bars indicate S.E.M. (n ≥ 3). Asterisk indicates the significance set at p-value: **≤0.01 (two-tailed Student's t-test). Grey line is set at 5μm scale.

## Discussion

Preservation and efficient repair of genomic integrity is of utmost importance for cellular function and organismal development and viability. For this reason, multiple specialized and partially overlapping DNA repair mechanisms have evolved. Defects in any of these pathways and the subsequent accumulation of DNA damage have been associated with cellular death or senescence and tissue function decline, leading to complex pathological consequences that range from cancer susceptibility to developmental impairment and premature ageing[24,173]. The huge complexity of the DNA repair syndromes cannot be explained by the cell autonomous effects of DDR. Once the damage is detected, the DDR signaling is activated as a protective response and is directed inwards, by stalling cell cycle progress until the damage is repaired. Additionally, at the same time, it triggers a response directed outwards to alert the surrounding environment for the presence of threat and to maintain organismal homeostasis[1,24,46]. The systemic responses to cellular DNA damage interferes with many aspects of physiology, including stem cell dysfunction, metabolic alterations and immune deficiencies[174]. During normal ageing, both DNA repair and immune systems' efficiency gradually decline and have been associated with the manifestation of many ageing-associated pathologies[175,176]. Indeed, many DNA repair progeroid syndromes manifest perturbed inflammatory responses and, vice versa, mouse models with deficiencies in immune response mediators develop age-related characteristics and reduced lifespan[92].
In addition, accumulating evidence support the reciprocal connection between those two systems with each one regulating and interfering with one another[1,46,52] and both underlying the development of progeroid features, although we still lack a mechanistic insight into this process.

ERCC1 deficiency results in the development of a great heterogeneity of pathological symptoms in both human and the respective mouse models. However, the diversity of the clinical manifestations and the tissue-specific pathologies due to mutations in *Ercc1* cannot be fully explained, especially in view of the random nature of DNA damage events. One possible explanation could be the fact that ERCC1 is also involved in other repair mechanisms (ICL repair), as well as its role in other processes beyond repair (transcription). Previous studies have shown that the growth defect caused by ERCC1 malfunction (which is also seen in other progeroid NER mice and patients) is attributed to the transcriptional defect in genes that regulate key hormonal axes (somatotroph, lactotroph and thyrotroph axes)[72,108]. In addition, it has been shown that the age-associated characteristics of ERCC1 defective mice are mediated by the induction of inflammatory responses[114,116,177].

In the present study, we aim to gain functional insight into how genome maintenance is connected to inflammatory signaling and the manifestation of age-related pathology. Since *Ercc1*$^{-/-}$ full knock out mice fail to develop normally and die before weaning and to also exclude the contribution and indirect effects of systemic responses, we generated a tissue-specific *Ercc1*$^{-/-}$ knock out mouse model, by restricting *Ercc1* deletion in macrophages. Macrophages are key

players during the innate immune response. They are found in almost every tissue which enables them to respond immediately in the case of infection or any disturbance of homeostatic balance[178]. Besides their role in host defense, they also mediate the maintenance of tissue structural and functional integrity, contributing to the regulation of systemic metabolic status[109]. Due to their multifunctional roles, they have been implicated in the progression of age-associated pathologies. For these reasons and for the purpose of this study, they offer us a powerful tool to study the role of DNA damage in an immune context.

**The effect of ERCC1 ablation in macrophages**

*Er1*$^{F/-}$ mice were born at the expected rate, developed normally and had no defects in macrophage numbers, both during hematopoiesis and in tissues. Deletion of *Ercc1*, led to accumulation of DNA damage in macrophages and the activation of DNA damage response (**Figure 6**), together with indications of activated status (larger volume in comparison to WT macrophages, pseudopodia formation) (**Figure 5B, 7I, 14F**). Nuclear DNA damage can trigger nuclear to cytoplasmic signaling[26,179]. We observed a cytoplasmic stress response in *Er1*$^{F/-}$ macrophages, including autophagy, Golgi dispersal and ER stress (**Figure 7A**). The lack of apoptosis in *Er1*$^{F/-}$ macrophages indicated that these responses were not a side-effect of cell death, but rather a direct consequence of activated DDR signaling, as shown by their dependence on ATM and ATR signaling. Indeed, ATM signaling has been shown to act as a messenger linking the presence of nuclear DNA damage to the cytoplasm, where it triggers cytoplasmic signaling cascades. Thus it is considered to be the link between cell autonomous and non-cell autonomous, systemic responses[25,52].Observation of the *Er1*$^{F/-}$ macrophages with electron microscopy revealed the formation of cytoplasmic formation and the accumulation of vacuolar structures in the cytoplasm (**Figure 7I**) which, together with the ER and Golgi reorganization, pointed to altered secretory processes. Finally, we studied the cell-autonomous effects of DNA repair deficiency in macrophages by transcriptome analysis, which verified the pro-inflammatory state of these macrophages, the induction of apoptosis and ER stress, as well as the activation of vesicular transport pathways. it should be noted that ER stress and autophagic network imbalances have been associated with the activation of proinflammatory status of immune cells and the secretion of inflammatory effectors[123,124,180–183]. Thus, they could be the drivers of the activated phenotype of *Er1*$^{F/-}$ macrophages.

At a systemic level, we found accumulation of macrophages in various tissues, together with increased expression of adhesion molecules which are known to facilitate immune cell recruitment at sites of tissue damage (**Figure 11A, 11C**). Thus, *Er1*$^{F/-}$ mice presented signs of systemic inflammation. Further phenotypic analysis of these macrophages revealed overrepresentation of an alternatively activated (M2) population (**Figure 11F**). Classically activated (M1) macrophages are proinflammatory and associated with chronic inflammatory diseases, obesity and insulin resistance. In contrast, alternatively activated (M2) macrophages serve suppressive, anti-inflammatory functions with major roles in resolution of inflammation and tissue repair[178]. Increased M2 signaling

has been shown to eliminate the obesity-related metabolic abnormalities and to facilitate the maintenance of insulin sensitivity[184,185]. In addition, M2 polarized macrophages are the main macrophage subpopulation found in tumors. Together with the increased expression of adhesion molecules, we cannot exclude the formation of a pro-tumorigenic environment.

### *Er1$^{F/-}$* mice develop metabolic alterations

Due to their presence in almost every tissue, macrophages play a central role in the maintenance of homeostatic balance[134]. They receive signals from the surrounding environment and respond to them by eliminating the damaged or infected cells together with priming the adaptive immune response. To achieve proper regulation of these functions, they depend on the secretion of modulating factors[186,187]. They are also responsible for the resolution of inflammation. Indeed, inability to eliminate the immune response has been linked to chronic inflammation and the development of inflammatory and metabolic diseases[168,188]. These imbalances between pro- and anti-inflammatory networks have also been considered as a contributing factor in age-related diseases[109,127]. In addition, ERCC1 defects have been shown to trigger responses that cause metabolic alterations, both in full knock out and tissue specific mouse models[116,189]. We observed that *Er1$^{F/-}$* mice maintained a lower body-weight and fat mass than their littermate controls (**Figure 8B, 8C**). We verified that this was not the result of reduced food consumption, which was similar between *Er1$^{F/-}$* and WT mice. In addition, *Er1$^{F/-}$* mice presented lower steady-state glucose levels, without alterations in the respective insulin levels. Glucose uptake by liver and muscle tissue of *Er1$^{F/-}$* mice was enhanced and, in line, *Er1$^{F/-}$* mice presented improved glucose tolerance than WT mice, without any alteration in their sensitivity to insulin. The enhanced glucose tolerance developed progressively and was exacerbated under a high-fat diet (HFD) (**Figure 8G, 9B**). High-fat diet-induced obesity is a known trigger of macrophage activation. The excessive nutrient intake and the interaction between hypertrophic adipose tissue and macrophages lead to a gradual metabolic decline and the manifestation of systemic metabolic dysfunction and diseases[138]. In our system, the use of a HFD acted as an activating signal for macrophages that further enhanced the systemic effects of the ERCC1 defective macrophages. Importantly, we observed no differences in insulin sensitivity in HFD fed *Er1$^{F/-}$* mice, as well as similar weight gain with WT mice **(Figure 9)**. Thus, the effects of *Er1$^{F/-}$* macrophages were independent of leanness and also uncoupled from insulin signaling, pointing to an alternative pathway mediating the altered glucose metabolism. We also detected accumulation of glycogen and lower deposition of triglycerides in the livers of *Er1$^{F/-}$* mice (**Figure 10A, 10B**). Despite feeding a HFD, *Er1$^{F/-}$* mice retained the decreased triglyceride content in their livers. Increased glycogen accumulation has been shown to affect appetite, leading to decreased food consumption, lower body weight and fat mass, together with reduced triglyceride liver content (liver glycogen obesity). Nonetheless, appetite alterations were not observed in *Er1$^{F/-}$* mice, since food consumption was similar to that of *Er1$^{F/+}$* control mice. In addition, ERCC1 levels in hypothalamus, known to regulate appetite, were normal and no signs of DNA damage (γH2AX foci) were detected. Therefore, the altered glycogen and triglyceride liver content are a consequence of

deletion of *Ercc1* in macrophages, rather than a secondary effect due to hypothalamic dysfunction. In line with the increased glycogen, we detected increased mRNA levels of glycogen synthesis genes and a parallel downregulation of glycogen breakdown genes. These findings are in accordance to previous reported metabolic shifts in *Ercc1*$^{-/-}$ and *Csb*$^{m/m}$*/Xpa*$^{-/-}$ progeroid mice[104,189]. Furthermore, these mice exhibited lower serum glucose levels and triglyceride accumulation in their livers, similar to our findings. These metabolic alterations were also reported in naturally aged mice and were associated with the hypo-somatotrophism presented in the progeroid mice (as well as in aged mice). In contrast to *Ercc1*$^{-/-}$ mice, which were hypo-insulinemic, we did not report any alterations in insulin levels or sensitivity in *Er1*$^{F/-}$ mice. This could be attributed to the restricted lack of ERCC1 only in macrophages. Lower insulin levels in full knock outs could be an additive or secondary effect due to whole body deficiency in ERCC1. Further investigation proved that the metabolic shifts observed in the progeroid mice were cell-autonomous[108] and could be attributed to the role of ERCC1 in transcription of developmental genes in liver[75,83]. However, in *Er1*$^{F/-}$ mice the livers were DNA repair proficient and only the macrophages accumulated DNA damage. Thus, in our model, glycogen storage and triglyceride accumulation in liver is rather a non-cell autonomous response triggered by the ERCC1 deficient macrophages. The non-cell-autonomous effects of DNA damage have been shown in multiple studies. For example, genotoxic stress in *C. elegans* germline induced the secretion of putative pro-inflammatory peptides that triggered a systemic innate immune signaling, resulting in increased stress tolerance in the soma[190,191]. In addition, UV-induced DNA damage in *D. melanogaster* larval epidermis induced the secretion of cytokines and the activation of a systemic innate immune response. This systemic response was sufficient to inhibit insulin signaling and dampen larval growth[192]. In mammals, skin UV-induced local inflammation resulted in systemic immunosuppression[193]. Therefore, cells carrying nuclear DNA damage activate a response that is directed outwards, so as to alert the surrounding cells, leading to a systemic adaptive response. The inflammatory and metabolic systemic effects reported in our results, suggest that DNA repair deficient macrophages can communicate and send alarming signals to the surrounding tissues. To test this hypothesis, we performed high-throughput analysis of transcriptome and secretome of *Er1*$^{F/-}$ macrophages. RNA-seq analysis revealed the overrepresentation of innate immune response, as well as GTPase-mediated signaling and endosomal/vacuolar pathways in *Er1*$^{F/-}$ macrophages. The latter is also supportive of our electron microscopy findings of increased cytoplasmic projections and altered ER and Golgi organization. We then analyzed by mass spectrometry (MS) the cell-culture media of isolated *Er1*$^{F/+}$ and *Er1*$^{F/-}$ macrophages. In agreement, we observed the overrepresentation of proteins associated with membrane-bound organelles and extracellular vesicles (EVs), along with several RAB members of the RAS GTPase superfamily (**Figure 13**). Additional experiments verified our proteomic results. *Er1*$^{F/-}$ macrophages presented with elevated levels of both GTPases and exosomal markers. The upregulation of these proteins were DNA damage dependent and inhibition of DDR signaling restored their levels to those of WT macrophages (**Figure 15**). Similarly, the exosomal secretion was also dependent on DNA damage signaling, as well as on active GTPases. Multiple GTPases are known to coordinate multiple steps of exosomal

secretion, from MVB formation, maturation and fusion with the plasma membrane[133]. In addition, Rac1 has been implicated in DDR signaling at multiple steps[194,195]. Therefore, it is possible that DNA damage induces the expression and activation of GTPases, leading to increased biogenesis and secretion of EVs, in an attempt to shuttle protective signals and alert other cells of their compromised state. It has been shown that various stressful conditions trigger the secretion of EVs so as to promote protective and adaptive signals to bystander cells[156]. However, enhanced exosome secretion and constant presence of this exosomal signaling lead to adverse effects, for example senescence and inflammation[196]. In our system, due to lack of ERCC1, DNA damage is accumulated and DDR signaling persistent. Thus, the continuous secretion of EVs results in alterations in the physiological and metabolic status of the surrounding tissues, affecting systemic homeostatic balance.

### *Er1*$^{F/-}$ macrophage-derived EVs trigger metabolic reprogramming and immune response in recipient cells

EVs can orchestrate the communication of different tissues, so as to preserve metabolic homeostasis[197,198]. In addition, through their immunomodulatory effects, they can modify systemic responses to glucose and insulin and promote metabolic pathologies[160,199]. We noticed that *Er1*$^{F/-}$ macrophage-derived EVs were loaded with GTPases which were efficiently delivered to various metabolically active tissues, including pancreas and liver. Among their divergent functions, Rab and Rho GTPase members have emerged as regulators of metabolic homeostasis[200]. For example, several GTPases mediate the trafficking and dicking of glucose transporters on cell surface. Compromised Rho GTPase signaling has been associated with insulin resistance, while overexpression of constitutively active Rac1 resulted in increased GLUT4 levels even in the absence of insulin[149,150]. *Er1*$^{F/-}$ EVs, as well as EVs from MMC-treated macrophages, along with their cargo, were uptaken by recipient cells and triggered glucose uptake. This was accomplished by upregulation of GLUT levels, both at mRNA and protein levels (**Figure 17**). One possible mechanism underlying the increased GLUT levels could be the effect of the newly imported GTPases. For example, apart from its role in GLUT trafficking, Rac1 has been attributed with additional roles, including transcription and NADPH activity[201,202]. Through the later, it mediates ROS production, therefore the oxidative status the cells[146,203]. Since oxidative stress-induced signaling has been implicated in the upregulation of GLUT1 transcription[204], we cannot exclude the possibility that accumulated RAC1 mediates the increased levels of *Glut1* mRNA. This is also supported by our findings that GTPases are directly transferred to recipient cells, while GLUT upregulation is subsequently observed at mRNA (3h post EV exposure) and protein (24h post EV exposure) levels. The accumulation of GLUTs were observed in various tissues (liver, pancreas, WAT) and could mediate the reduced blood glucose levels and the increased rate of glucose absorption during GTT. Collectively, this could be a new mechanism by which DNA damage elicits systemic responses and metabolic alterations of glucose metabolism.

**EV-triggered glucose uptake mediates the activation of innate immune signaling in recipient cells**

Cellular metabolism can affect the function of immune cells and, vice versa, immune cell function can impact the metabolic status of the cells. Glucose is one factor bridging immune and metabolic responses. Diets high in carbohydrates exacerbate inflammatory responses through hyperactivation of NFκB[166]. In addition, exposure to high glucose primes macrophages for an aggravated inflammatory response[205] and also induces an M1 proinflammatory polarization[206]. Except for immune cells, glucose impacts the inflammatory state of non-immune cells as well. For example, exposure of pancreatic islets to high glucose levels resulted in NFκB activation and IL1b proinflammatory cytokine production[207]. Finally, elevated glucose levels are sufficient to upregulate multiple proinflammatory genes, many of which in an NFκB-dependent manner[208]. *Er1*$^{F/-}$ mice manifested signs of inflammation systemically and *Er1*$^{F/-}$ EVs lead to upregulation of GLUTs levels and enhanced glucose uptake by recipient cells. These findings prompted us to investigate if increased glucose uptake was able to trigger inflammatory signaling in the *Er1*$^{F/-}$ EVs-receiving cells and could be the underlying mechanism of the systemic inflammatory status of *Er1*$^{F/-}$ mice. EVs from macrophages carrying DNA damage (either due to ERCC1 deficiency or to MMC exposure) were able to trigger NFκB translocation to the nucleus. However, this was exacerbated and accompanied by increased iNOS levels only in the presence of EVs and the soluble fraction of macrophage secretome, which we found to contain proinflammatory factors (IL6, Il8). This is in agreement with previous studies showing that preconditioning with proinflammatory factors sensitizes the cells to the inflammatory effects of glucose[209]. Indeed, when the EVs recipient cells were exposed to high glucose concentrations, both nuclear NFκB and iNOS levels were further increased, compared to lower glucose concentrations (**Figure 18**). The metabolic and inflammatory effects of the *Er1*$^{F/-}$ EVs were also observed in vivo. Intravenous delivery of *Er1*$^{F/-}$ EVs recapitulated our in vitro data, including the upregulation of GLUTs, the increased glucose uptake and iNOS levels, as well as the systemic tolerance to glucose **(Figure 20)**. It is worth noting that these effects were cell-type specific, since EVs from *Er1*$^{-/-}$ MEFs and adipocytes failed to trigger the aforementioned responses.

The PI3K/AKT/mTOR is a multi-functional complex signaling pathway with established role in nutrient sensing and in the regulation of metabolism. Due to its function the balance between anabolic and catabolic status of the cells, this pathway has also been implicated in the ageing process[170]. For example, enhanced mTOR signaling has been shown to contribute to the pathologies observed in DNA damage-induced progeroid mouse models, including those deficient in ERCC1[210,211]. In addition to nutrients (such as glucose), mTOR is activated by inflammatory cytokines and various members of the RAS GTPase superfamily, including Rac1[212]. We found increased levels of phosphorylated Eukaryotic translation initiation factor 4E (eIF4E)-binding protein 1 (P4E-BP1), a protein translation repressor and known target of mTORC1 in PPCs exposed to either *Er1*$^{F/-}$ EVs or MMC-EVs. Inhibition of mTOR signaling in these PPCs with rapamycin, reduced the levels of P4E-BP1, iNOS and NFκB (**Figure 19**).

However, rapamycin treatment did not reverse the glucose uptake by PPCs, pointing that mTOR signaling acts downstream of glucose uptake and upstream of proinflammatory signaling activation. Previous studies have shown a role of PI3K singaling in GLUT1 regulation and the activation of GLUT3 by mTORC1 in an NFκB-dependent manner[172]. Therefore, there could be a partial contribution of the mTOR-NFκB axis in the upregulation of GLUTs. In addition, the fact that prior activation of a proinflammatory state exacerbates the effects of glucose, together with the reverse observations that high glucose primes cells for an inflammatory response, could point to a positive feedback loop. More specifically, continuous exposure to EVs from DNA damaged cells triggers the sustained glucose uptake by recipient cells. Intracellular glucose, together with a possible contribution of the GTPases transferred directly to EV-recipient cells, stimulates the mTOR signaling cascade which activates a proinflammatory response. In turn, the development of a proinflammatory environment further sensitizes the cells to the effects of glucose. Hence, the secretion of EVs by DNA repair deficient macrophages could be a beneficial response short-term, so as to trigger metabolic adaptations to surrounding cells to cope until the DNA damage threat is resolved the accumulation of DNA damage in macrophages. Nonetheless, due to macrophage incapacity to repair DNA damage, the signaling becomes sustained, resulting in gradual deterioration of the metabolic status of the organism.

## Concluding remarks

Multiple evidence have shown an intertwined relationship between DNA damage, metabolic disturbances and inflammatory responses. Each node of this complex network contributes to the onset of premature diseases, but the underlying mechanisms remain poorly understood. In the present study, we provide a mechanistic link between genomic instability and systemic inflammatory and metabolic alterations. *Ercc1*$^{-/-}$ mice display severe progeroid phenotypes that have been shown to be mediated by systemic endocrine and metabolic alterations, as well as immune responses[104,114,116,177]. However, due to the segmental nature of the progeroid features, how distinct cell types adapt and contribute to these alterations remains ambiguous. We show that deletion of *Ercc1* in macrophages triggers an EV-mediated glucose-based metabolic reprogramming and chronic inflammation. *Er1*$^{F/-}$ mice are presented with systemic inflammation and increased sensitivity to glucose, independently of insulin. These phenotypes develop progressively and are aggravated upon a high fat diet. The mediating mechanism linking the macrophage-specific DNA repair defect to the systemic responses involves the secretion of EVs. We show that EV secretion is a direct consequence of DNA damage, as inhibition of DDR signaling blunts this response. Uptake of these EVs by metabolically active tissues, such as pancreas induces the uptake of glucose and triggers an mTOR-depedent proinflammatory signaling. Importantly, we provide evidence that the EV-mediated systemic alterations are tissue-specific and are elicited only by macrophage-derived EVs, since EVs from other DNA repair defective cell-types fail to trigger such responses. The field of EV research is continuously expanding, gaining an increasing interest in clinical application[213–215]. Further research on the effect of healthy donor-derived or of artificially-constructed EVs in ageing or progeroid mice would be of great importance in the development

of therapeutic approaches. In addition, the specificity of the macrophage-derived EVs effects is intriguing. Absence of ERCC1 only in macrophages elicited the EV mediated responses described in the present study, while EVs from other cell types failed to trigger this response, despite their defect in the same protein. Thus, further studies on the macrophage-specific roles of ERCC1 will enlighten us on this cell-type specificity observed. Recently, we developed a knock-in mouse model of XPF, the heterodimeric partner of ERCC1. In this mouse model, XPF carries a tag that is efficiently biotinylated, allowing us to efficiently isolate its protein partners and chromatin-bound loci[75]. Using such approaches we will be able to gain further insight into the specific roles of ERCC1 in macrophages, but also in other immune cells and metabolically active tissues, upon various conditions and treatments. Collectively, we describe a new mechanism underlying the chronic inflammatory and degenerative features of NER progeroid mice, providing new insight into tissue-specific pathologies and systemic responses in progeria and natural ageing. This knowledge could help us towards the development of new interventions for age-related pathologies and a healthier lifespan.

## Methods

### Mice

*Lys2-Cre* mice were crossed with *Ercc1*$^{+/-}$ mice. The *Lys2-Cre;Ercc1*$^{+/-}$ progenies were crossed with *Ercc1*$^{F/F}$ mice to obtain the *Lys2-Cre;Ercc1*$^{F/-}$ (*Er*$^{F/-}$) mice or the controls *Lys2-Cre;Ercc1*$^{F/+}$ (WT) mice. To generate the reporter mice, Lys2-Cre mice were crossed to *Rosa26-YFP*$^{st/st}$ mice. All pups were genotypes for the respective alleles, using standard PCR with the primer sets outlined in Table 1.

**Table 1.** Genotyping primers sequences

| Primer | Sequence (5´-3´) | Allele |
|---|---|---|
| **F25732** | TCAAAGTATGGTAGCCAAGGCAGC | Ercc1 |
| **432E** | TGCAGAGCCTGGGGAAGAACTTCGC | Ercc1 |
| **Cre F** | GCGGTCTGGCAGTAAAACTATC | Cre |
| **Cre R** | GTGAAACAGCATTGCTGTCACTT | Cre |
| **LysF** | CTTGGGCTGCCAGAATTTCTC | Lysozyme |
| **LysR** | TTACAGTCGGCCAGGCTGAC | Lysozyme |
| **Lys-Cre R** | TCAGCTACACCAGAGACGG | Lysozyme-Cre junction |
| **Rosa LC** | GCTCTGAGTTGTTATCAGTAAGG | YFP |
| **Rosa R2** | GCGAAGAGTTTGTCCTCAACC | YFP |
| **Rosa R3** | GGAGCGGGAGAAATGGATATG | YFP |

### Animal studies

Mice were maintained in grouped cages in a temperature-controlled virus-free facility on a 12-hrs light/dark cycle and fed either a high-fat diet (60% energy from fat, 20.3% carbohydrate, and 18.41% protein, 58Y1-58126, TestDiet) or a normal diet (Lactamin, Stockholm, Sweden). Mice had access to water ad

libitum. Body weight was measured weekly. For food intake experiments, mice were kept individually in separate cages. Defined food quantity was added daily in each cage and food consumption was measured every 24hrs. For glucose tolerance tests (GTT), mice were fasted for 16h and subsequently were injected intraperitoneally with 1 mg/gr of body weight 35% dextrose solution. Blood glucose levels were measured using CONTOUR® meter, at the indicated time points. To determine steady state glucose levels, 4- and 6-months old animals were fasted for 2h and glucose was determined as described previously. Serum insulin and triglyceride levels were measured with specialized kits (ALPCO and LabAssay triglyceride, Wako Chemicals, respectively). For the *in vivo* 2-DG uptake assay 6months old male mice were used (three in each group). Animals were fasted O/N and 2-DG (200 μmol/kg) was injected into the tail vein 15min after intraperitoneal insulin administration (1 Units/kg of body weight). Liver, soleus and rectus femoris muscle samples were collected 15 min after 2-DG injection. Tissues were digested with collagenase (2,5mgr/ml) and dispase II (2,4units/ml) at 37°C for 15 min. Collagenase was neutralized with 10%FBS and samples were further washed with 1xPBS/1%BSA. Homogenized tissues were passed through a 100μM wire mesh. Cells were resuspended in 10mM Tris-HCl pH 8.0 and disrupted with a microtip sonicator and heat treatment at 80$^{o}$C for 15min. Protein extracts were measured with Bradford and equal amounts of protein extracts (200μgr) were used to determine intracellular 2-DG–6-phosphate levels with a 2-DG uptake measurement kit (Cosmo Bio Co., Ltd.) according to manufacturer instructions. For the exogenous delivery of EVs, 4 weeks-old B6 mice were injected intravenously every 24 hours for 10 days with EVs isolated from media of 10x10$^{6}$ cells (*Er1*$^{-/-}$ or wt. MEFs and *Er1*$^{F/+}$ and *Er1*$^{F/-}$ BMDMs) as described in the section EV isolation. On day 10 mice were starved O/N and GTT was performed as described above. Mice were sacrificed and liver and muscle tissues were isolated and analyzed with Western blotting and Immunofluorescence. An independent Animal Ethical Committee at the IMBB-FORTH approved the animal studies.

**Primary cell cultures, transfection and cell assays**

*Er1*$^{F/+}$ and *Er1*$^{F/-}$ BMDMs were differentiated from bone marrow precursors. Briefly, bone marrow cells were isolated from mouse femurs and tibias and cultured for 7 days in DMEM containing 10% FBS, 30% L929 conditioned media, 50μg/ml streptomycin, 50 U/ml penicillin (Sigma) and 2mM L glutamine (Gibco). For TEM isolation, mice were injected intraperitoneally with 2ml 4% thioglycolate medium (Brewer). Three days later, mice were sacrificed and peritoneal cells were collected isolated by peritoneal lavage with 10 ml dMEM per mouse. Primary hepatocytes and PPCs were obtained from 20-days old mice. Briefly, liver and pancreas were excised, minced and incubated in 2mg/ml collagenase type IV at 37°C for 15 min. After centrifugation, cells were resuspended in DMEM containing 10% FBS, 50μg/ml streptomycin, 50 U/ml penicillin (Sigma) and 2mM L glutamine (Gibco). Before any experiment, primary hepatocytes were cultured overnight and PPCs for 4 days with medium replacement daily. Monocytes were isolated as previously described[216]. Mouse bone marrow neutrophils were isolated from femurs and tibias by flushing from the bones with ice cold DMEM. Neutrophils were isolated from the cell suspension by density gradient centrifugation on Percoll. The Percoll density gradient was prepared in a 15 ml tube by layering 2 ml of 67% and 52% Percoll

solution on top of 2 ml 75% Percoll solution. Cells were resuspended in 2 ml of PBS and loaded on top of the Percoll density gradient. Neutrophils were separated by centrifugation at 400 g for 30 min at 4°C in a swinging bucket rotor. The cell band formed between the 75 and 67% layer was harvested, cells were diluted with PBS, washed, and diluted in standard medium. Monocytes and neutrophils were cultured for 15hrs in low oxygen incubator prior to EV isolation. Primary MEFs and adipocytes were derived from *Ercc1*$^{-/-}$ animals. Adipocytes were prepared as previously described[116].

BL/6, *Er1*$^{F/+}$ BMDMs or *Er1*$^{F/-}$ were treated with 2.5 μg/μl mitomycin C (MMC; AppliChem) or tunicamycin (1μgr/ml), chloroquine (10μM), nocodazole (5μM) and NSC23766 (50μM Rac1 inhibitor), for ~15 hours in standard medium. For ATM or ATR kinase inhibitor assays (ATMi; ATRi), cells were incubated with 0.66 μM ATMi or ATRi (Millipore) for 1h, prior to MMC addition.

For glucose uptake assay, primary hepatocytes or PPCs were starved in low glucose medium in the presence of EVs for 24 hrs prior to incubation with 100μM 2-NBDG (Cat. No.6065, Tocris) for 15-20min. Cells were washed three times with PBS, fixed and counterstained with DAPI.

For mTOR inhibition, PPCs were incubated with the indicated medium and EVs, together with 2μM Rapamycin (Cat. No 1292, Tocris Bioscience) for 24hrs. For SA-β-gal activity a Beta-galactosidase (β-gal) assay kit was used (Abcam Inc. ab65351) according to manufacturer instructions. Briefly differentiated *Er1*$^{F/+}$ and *Er1*$^{F/-}$ BMDMs were fixed, washed with PBS and stained in β-galactosidase fixative solution at 37°C until β-gal staining became visible in either experimental or control plates (3hrs). Cells were washed in PBS, and the numbers of β-gal-positive cells (blue staining) in at least 350 cells were counted in random fields in each of the triplicate wells.

For Sentragor staining, cells were incubated with Sentragor reagent according to manufacturer instructions (Arriani pharmaceuticals, AR8850020). Briefly fixed differentiated BMDMS and TEMs were washed with 50 and 70% EtOH incubated with Sentragor reagent at RT, washed in EtOH and incubated with primary anti-biotin Ab and fluorochrome-labelled secondary antibody. Cells were washed in PBS, and the mean intensity of lipofuscin-positive cells in at least 100 cells were counted in random fields in each of the 6 individual repeats using Fiji software.

**Plasmid Transfection**

To generate the RAB10-GFP and RAC1-GFP and CD9-GFP, the cDNA encoding the whole open reading frame (ORF) of *Rab10 Rac1* and *CD9* genes were amplified by PCR using appropriately designed primers and were incorporated in pEGFP-N1 plasmid fused at the 3′ end with a sequence encoding EGFP, respectively. The primers used were as follows (restriction sites are underlined):

Rac1_pEGFPN1_For:5’-GATCTCGAGATGCAGGCCATC-3’,
Rac1_pEGFPN1_Rev:5’-AGTGGATCCCCCAACAGCAGG-3’,
Rab10_pEGFPN1_For:5’-GATCTCGAGATGGCGAAGAAG-3’,
Rab10_pEGFPN1_Rev:5’-AGTGGATCCCCGCAGCACTTG-3’,
CD9_pEGFPN1_For:5’GGCTCGAGATGCCGGTCAAAGGA-3’
CD9_pEGFPN1_Rev:5’-GGGGATCCCCGACCATTTCTCG-3’.

For plasmid transfections, approximately 1 × $10^6$ differentiated BMDMs were transfected with 5μg of total plasmid DNA using Amaxa mouse macrophage

nucleofector kit according to the manufacturer's instructions (Lonza, VPA1009). BMDMs were incubated for 24hrs and their media were used for EV isolation, as described below.

**Oxygen consumption rate measurement**

For the oxygen consumption rate (OCR) analysis, PPCs (~1,5x$10^6$) were treated with EVs for 24 hrs and were harvested with trypsin/EDTA, rinsed with phosphate-buffered saline (PBS) (with 10 % FBS), and centrifuged at 1,200×g for 3 min. Cells were re-suspended in 1.5ml of PBS. The OCR (nmoles O2/min) was measured for 20min at 37°C using a Clark-type electrode (Hansatech). The average OCR was determined from 1 min measurements deriving from 4 different time points (3, 6, 9, 12min) as previously described[165]. OCR data were normalized to total protein content using the Bradford method.

**EV isolation and labelling**

Exosomes were purified using the differential ultracentrifugation protocol[217]. Briefly, culture medium was centrifuged sequentially at 300g, (10min), 2000g (10min) and 10000g (30min) to remove dead cells and cell debris. Extracellular vesicles were purified with the final step of ultracentrifugation at 100000g for 2hrs. For functional experiments, macrophage-derived EVs were purified 5 times the number of recipient cells. For PKH67 staining, EVs were incubated with PKH67 (500 mL 0.2 mM) for 5 min at room temperature. Labelled EVs were diluted in 500 mL 1% BSA, and then pelleted at 100,000 g, washed with 1 mL PBS to remove excess dye, re-suspended in 1 mL PBS and then pelleted at 100,000 g before final re-suspension. The same protocol was followed in the absence of EVs (dye alone) to ensure lack of fluorescence. For functional experiments, macrophage-derived EVs were purified 5 times the number of recipient cells and then added in the medium of PPCs or hepatocytes for 3 or 24 hrs. For SDS-PAGE analysis, EVs derived from 20-25x$10^6$ macrophages were used.

**Electron microscopy**

For transmission electron microscopy, primary macrophages were washed in PBS followed by fixation in 2% paraformaldehyde, 2% glutaraldehyde in 0.1 M sodium cacodylate buffer (pH 7.42) with 0.1% magnesium chloride and 0.05% calcium chloride. After washes with sodium cacodylate buffer, cells were fixed in 1% osmium tetroxide in sodium cacodylate buffer and samples were dehydrated in ethanol gradient. Samples were then treated with propylene oxide and embedded in Epon/Araldite resin mix. Ultrathin-sections (50-100nm) were taken on a Leica LKB2088 ultramicrotome and were examined under JEM 100C/JEOL/Japan Transmission Electron Microscope. Microphotographs were obtained with an ES500W Erlangshen camera and processed with the Digital Micrograph software (Gatan, Germany). Electron microscopy (EM) analysis of whole-mount exosome preparations was performed as previously described[217]. Briefly, fixed EVs were deposited on EM grids and were further fixed with glutaraldehyde. Samples were first contrasted in a solution of uranyl oxalate and then contrasted and embedded in a mixture of 4% uranyl acetate and 2% methyl cellulose.

**Histology**
*Er1$^{F/+}$* and *Er1$^{F/-}$* livers were OCT-embedded, cryosectioned, fixed in 10% formalin, stained with oil red O or Periodic acid–Schiff (PAS), counterstained with Harris's hematoxylin and visualized with DAB chromogen (Sigma). For histological analysis of *Er1$^{F/+}$* and *Er1$^{F/-}$*tissues, samples were fixed in 4% formaldehyde, paraffin embedded, sectioned and stained with Harris's Hematoxylin and Sudan Black B (SBB)-Analogue (GL13).

**Immunofluorescence**
For immunofluorescence experiments of mouse tissues, minced tissues (liver, pancreas and hypothalamus) and BMDMs, TEMs, PPCs and primary hepatocytes seeded on coverslips were fixed in 4% formaldehyde and permeabilized with 0.5% Triton-X. Non-specific binding was blocked with the addition of 3% normal calf serum and 1% BSA in the permeabilization buffer. After overnight incubation with primary antibodies, secondary fluorescent antibodies were added for 1 hour and DAPI was used for nuclear counterstaining. Samples were imaged with SP8 confocal microscope (Leica)

**Live cell imaging**
Rapid time-lapse imaging was performed using SP8 confocal microscope (Leica) with a stage-top incubation system creating a 37°C environment. Z-stacks of 3-4 sections with two-channel detection were acquired every. For live cell experiments, *in vitro* differentiated Er1$^{F/+}$ and Er1$^{F/-}$ BMDMs were transfected with 5μg of total plasmid DNA (pEGFP-CD9, described previously). Transfected cells were seeded on a Mattek culture dish and imaged 24hrs post transfection. Time-lapse stacks were analyzed with Fiji. At least 20 cells from each genotype were recorded in total in three independent replicates.

**ELISA**
Macrophages were cultured as mentioned before. Subsequently, the medium was removed, and cells were washed with sterile phosphate-buffered saline (PBS). Then, the medium was replaced with fresh DMEM serum-free medium and incubated for 24 h in the same conditions as before. Subsequently, cell cultures were centrifuged at 1000 × g for 10 min and the supernatants were recovered. Serum from *Er1$^{F/+}$* and *Er1$^{F/-}$* blood was isolated after centrifugation at 1,000–2,000 x g for 10 minutes and frozen. Culture supernatants and serum were evaluated for the production of cytokines or chemokines by a Multi-Analyte ELISArray panel. For this, chemokines (IL1B IL6 IFNg MCP1 KC SDF-1) were determined by Common Chemokines Multi-Analyte ELISArray kit (Cat No./ID: 336161;QIAGEN) and performed according to the manufacturer's instructions. The absorbance of the products was measured at 450 nm in a microplate reader and cytokine or chemokine levels were determined in relation to the standard curve of the given chemokines.

**Protein extraction and Immunoblot analysis**

For western blot analysis, cells were pelleted and tissues from *Er1*$^{F/-}$ and *Er1*$^{F/+}$ animals were homogenized in Sucrose buffer (0.32M Sucrose, 15mM HEPES-KOH, 60mM KCl, 2mM EDTA, 0.5mM EGTA, 0.5%BSA, 0.1%NP-40, pH-7.9 and protease inhibitors). Cell pellets were washed three times with 1x PBS. Cytoplasmic and nuclear protein extracts were prepared as previously described[75] using a high-salt extraction method (10 mM HEPES–KOH pH 7.9, 380 mM KCl, 3 mM $MgCl_2$, 0.2 mM EDTA, 20% glycerol and protease inhibitors). For whole cell extract preparations, cells pellets were resuspended in 150mM NaCl, 50mM Tris pH=7.5, 5% Glycerol, 1% NP-40, 1mM MgCl and incubated on ice for 30 min. For western blot analysis of EVs, EV pellets were resuspended in 2x Laemli buffer. Protein extracts were analysed in SDS-polyacrylamide gels, blotted on nitrocellulose membranes and incubated with the corresponding primary and HRP-conjugated secondary antibodies (see Table 2).

**Table2.** Antibodies list

| **Antibody** | **Clone** | **WB dilution** | **IF dilution** | |
|---|---|---|---|---|
| Rac2 | C-11 | 1/500 | 1/100 | SantaCruz Biotechnology |
| RhoA | 26C4 | 1/500 | 1/100 | SantaCruz Biotechnology |
| CD9 | C-4 | 1/500 | 1/100 | SantaCruz Biotechnology |
| Glut2 | H-67 | 1/500 | 1/100 | SantaCruz Biotechnology |
| Glut3 | B-6 | 1/500 | 1/100 | SantaCruz Biotechnology |
| LC3 | C-9 | 1/500 | 1/500 | SantaCruz Biotechnology |
| FancI | H102 | - | 1/50 | SantaCruz Biotechnology |
| Ercc1 | D-10 | 1/500 | 1/50 | SantaCruz Biotechnology |
| Albumin | P-20 | 1/500 | 1/200 | SantaCruz Biotechnology |
| Amylase | G-10 | 1/500 | 1/100 | SantaCruz Biotechnology |
| Biotin | 600-401-098 | - | 1/500 | Rockland |
| LaminB1 | ab16048 | - | 1/1000 | Abcam |
| Glut1 | ab40084 | 1/300 | 1/150 | Abcam |
| Grp78/BiP | ab21685 | 1/500 | 1/200 | Abcam |
| F4/80 | ab6640 | 1/500 | - | Abcam |
| b-Tubulin | ab6046 | 1/1000 | - | Abcam |
| iNOS | ab15323 | 1/500 | 1/100 | Abcam |
| p62 | SQSTM1/PM045 | 1/5000 | 1/1000 | MBL |
| γH2AX | 05-636 | - | 1/12000 | Millipore |
| pATM | 05-740 | - | 1/100 | Millipore |

| | | | | |
|---|---|---|---|---|
| Rad51 | ABE257 | - | 1/100 | Millipore |
| Caspase 3 | AB3623 | - | 1/200 | Millipore |
| pGlut(Ser226) | ABN991 | - | 1/500 | Millipore |
| GM130 | 35 | 1/500 | 1/200 | BD Transduction Laboratories |
| Alix | #2171 | 1/500 | - | Cell Signaling |
| Rab10 | #81272 | 1/500 | 1/100 | Cell Signaling |
| NFκB p65 | #8242 | - | 1/100 | Cell Signaling |
| p4EBP1 | #2855 | 1/500 | - | Cell Signaling |
| Phospho-p70 S6 Kinase(Ser371) | #9208 | 1/500 | - | Cell Signaling |
| VCAM | P8B1 | - | 1/200 | Developmental Studies Hybridoma Bank (DSHB) |
| CD45 | H5A5 | - | 1/200 | Developmental Studies Hybridoma Bank (DSHB) |
| ICAM | P2A4 | - | 1/100 | Developmental Studies Hybridoma Bank (DSHB) |
| PECAM | 2H8 | - | 1/200 | Developmental Studies Hybridoma Bank (DSHB) |
| MacI | M1/70.15.11.5.2 | - | 1/200 | Developmental Studies Hybridoma Bank (DSHB) |
| RacI | ARC03 | 1/500 | 1/50 | Cytoskeleton |
| PKH67 Greeen Fluorescent Cell Linker Midi Kit | MIDI67 | - | - | Sigma Aldrich |
| Goat anti-rat IgG-CFL 647 | sc-362293 | - | 1/1000 | SantaCruz Biotechnology |
| Donkey anti-goat IgG-HRP | sc-2020 | 1/5000 | - | |
| Goat anti-rabbit IgG, Peroxidase Conjugated | AP132P | 1/10000 | - | Millipore |
| Goat anti-mouse IgG, Peroxidase | AP124P | 1/10000 | - | Millipore |

| | | | | |
|---|---|---|---|---|
| Conjugated, H+L | | | | |
| Goat anti-Mouse IgG (H+L) Cross-Adsorbed Secondary Antibody, Alexa Fluor 488 | A-11001 | - | 1/2000 | ThermoFisher |
| Goat anti-Mouse IgG (H+L) Cross-Adsorbed Secondary Antibody, Alexa Fluor 555 | A-21422 | - | 1/2000 | ThermoFisher |
| Donkey anti-Rabbit IgG (H+L) Highly Cross-Adsorbed Secondary Antibody, Alexa Fluor 488 | A-21206 | - | 1/2000 | ThermoFisher |
| Donkey anti-Rabbit IgG (H+L) Highly Cross-Adsorbed Secondary Antibody, Alexa Fluor 555 | A-31572 | - | 1/2000 | ThermoFisher |
| Goat anti-Rat IgG (H+L) Cross-Adsorbed Secondary Antibody, Alexa Fluor 555 | A-21434 | - | 1/2000 | ThermoFisher |
| DAPI | 62247 | - | 1/20000 | ThermoFisher |

**FACS analysis**

Cohorts of 6-8 months old, male *Er1*$^{F/+}$, *Er1*$^{F/+}$ fed on a high fat diet and *Er1*$^{F/-}$ animals (n=3) were used. Pancreas, spleen and epididymal fat tissues were minced and digested in 1xPBS/1%BSA/0.1%$NaN_3$/collagenase (2.5mgr/ml) and further processed with a Dounce homogenizer. Red blood cells were lysed in ice cold red blood cell lysis buffer (1.5M $NH_4Cl$, 0.1M $KHCO_3$, 0.01M EDTA). Homogenized tissue was further washed in PBS-BSA buffer and passed through a 100μM wire mesh. Peripheral blood was isolated with heart puncture

and bone marrow was isolated from femurs and tibias. Erythrocytes were lysed as previously mentioned. Samples were further washed in PBS-BSA buffer. Cells were stained with fluorochrome conjugated antibodies (CD45, CD11b, F4/80, CD11c and CD206, Biolegend) for 20 min at 4°C in PBS/5% FBS. Samples were acquired on a FACS Calibur (BD Biosciences) and analyzed using the FlowJo software (Tree Star).

**Mass Spectrometry studies**

*Er1*$^{F/+}$ and *Er1*$^{F/-}$ BMDMs were cultured for 24h in serum-free medium. The medium was then concentrated using Amicon Ultra-15 Centrifugal Filter Units, resolved on 10% SDS-PAGE gel and stained with Colloidal blue silver (ThermoFisher Scientific, USA). The entire lane was cut out and divided into at least 12 gel plugs, which were each further reduced to 1 $mm^3$ gel pieces and placed in low-bind tubes (Eppendorf UK). Proteins were in-gel-digested by using modified trypsin (Roche Diagnostics) in 50 mM ammonium bicarbonate. Peptide mixtures were analyzed by nLC-ESI-MS/MS on a LTQ-Orbitrap XL coupled to an Easy nLC (Thermo Scientific). The sample preparation and the nLC-ESI-MS/MS analysis were performed as previously described[218] with minor modifications. Briefly, the dried peptides were dissolved in 0.5% formic acid aqueous solution, and the tryptic peptide mixtures were separated on a reversed-phase column (Reprosil Pur C18 AQ, Dr. Maisch GmbH), fused silica emitters 100 mm long with a 75μm internal diameter (ThermoFisher Scientific, USA) packed in-house using a packing bomb (Loader kit SP035, Proxeon). Tryptic peptides were separated and eluted in a linear water-acetonitrile gradient and injected into the MS.

**RNA-Seq and Quantitative PCR studies**

Total RNA was isolated from *Er1*$^{F/+}$ and *Er1*$^{F/-}$ BMDMs using a Total RNA isolation kit (Qiagen) as described by the manufacturer. For RNA-Seq studies, libraries were prepared using the Illumina® TruSeq® mRNA stranded sample preparation Kit. Library preparation started with 1μg total RNA. After poly-A selection (using poly-T oligo-attached magnetic beads), mRNA was purified and fragmented using divalent cations under elevated temperature. The RNA fragments underwent reverse transcription using random primers. This is followed by second strand cDNA synthesis with DNA polymerase I and RNase H. After end repair and A-tailing, indexing adapters were ligated. The products were then purified and amplified to create the final cDNA libraries. After library validation and quantification (Agilent 2100 Bioanalyzer), equimolar amounts of all 12 libraries were pooled. The pool was quantified by using the Peqlab KAPA Library Quantification Kit and the Applied Biosystems 7900HT Sequence Detection System. The pool was sequenced by using an Illumina HiSeq 4000 sequencer with a paired-end (2x 75 cycles) protocol. Quantitative PCR (Q-PCR) was performed with a DNA Engine Opticon device according to the instructions of the manufacturer (MJ Research). The generation of specific PCR products was confirmed by melting curve analysis and gel electrophoresis. Each primer pair was tested with a logarithmic dilution of a cDNA mix to generate a linear standard curve (crossing point (CP) plotted versus log of template concentration), which was used to calculate the primer pair efficiency ($E=10^{(-1/slope)}$). Hypoxanthine guanine phosphoribosyltransferase1 (*Hprt-1*) mRNA was used as an external standard. For data analysis, the second

derivative maximum method was applied: ($E1_{\text{gene of interest}}^{\Delta CP\ (\text{cDNA of wt. mice - cDNA of } \textit{Ercc1F/-}) \text{ gene of interest}}$/ ($E_{\text{hprt-1}}^{\Delta CP\ (\text{cDNA wt. mice- cDNA}) \text{ hprt-1}}$).

**Data analysis**

For Q-PCR data, a two-way t-test was used to extract the statistically significant gene expression data (unless noted otherwise) by means of the IBM SPSS Statistics 19 (IBM, NY, USA), Spotfire (Tibco, CA, USA), Partek (Partek INCoR1porated, MO, USA) and R-statistical package (www.r-project.org/). For mass spectrometry (MS), the MS/MS raw data were loaded in Proteome Discoverer 1.3.0.339 (Thermo Scientific) and run using Mascot 2.3.02 (Matrix Science, London, UK) search algorithm against the *Mus musculus* theoretical proteome (Last modified July 6, 2015) containing 46,470 entries[219]. A list of common contaminants was included in the database[220]. For protein identification, the following search parameters were used: precursor error tolerance 10ppm, fragment ion tolerance 0.8Da, trypsin full specificity, maximum number of missed cleavages 3 and cysteine alkylation as a fixed modification. The resulting .dat and .msf files were subsequently loaded and merged in Scaffold (version 3.04.05, Proteome Software) for further processing and validation of the assigned MS/MS spectra employing PeptideProphet and ProteinProphet algorithms for the identification of protein[221–223]. Thresholds for protein and peptide identification were set to 99% and 95% accordingly, for proteins with minimum 1 different peptides identified, resulting in a protein false discovery rate (FDR) of <0.1%. For single peptide identifications, we applied the same criteria in addition to manual validation. Protein lists were constructed from the respective peptide lists. For label-free relative quantitation of proteins, we applied a label-free relative quantitation method between the different samples (control versus bait) in order to determine unspecific binders during the affinity purification. All .dat and .msf files created by Proteome Discoverer were merged in Scaffold where label-free relative quantification was performed using the total ion current (TIC) from each identified MS/MS spectra. The TIC is the sum of the areas under all the peaks contained in a MS/MS spectrum and total TIC value results by summing the intensity of the peaks contained in the peak list associated to a MS/MS sample. This approach has advantages in comparison to other label-free methods, such as increased dynamic range and quantification for low spectral counts[224]. Protein lists containing the calculated by Scaffold total TIC quantitative value for each protein ware exported from to Microsoft Excel for further processing. The fold change of protein levels was calculated by dividing the mean total TIC quantitative value in bait samples with the mean value of the control samples for each of the proteins. Proteins having ≥80% protein coverage, ≥1 peptide in each sample (*Er1*$^{F/-}$ BMDMs) and a fold change ≥1.55 were selected as being significantly enriched in *Er1*$^{F/-}$ BMDMs compared to *Er1*$^{F/+}$ BMDM controls. Significant overrepresentation of pathways, protein-protein interactions and protein complexes were derived by STRING[225] (http://string-db.org/). For RNA-Seq data analysis, the data were downloaded as FASTQ files and their quality was checked with FASTQC, a quality control tool for high throughput sequence data: http://www.bioinformatics.babraham.ac.uk/projects/fastqc). The data were aligned to mm10 genome assembly available from UCSC via Bowtie2. The differentially expressed genes were identified with metaseqR. Count normalization was performed based on edaseq algorithm. In parallel, cufflinks

pipeline (version 2). Significant overrepresentation of pathways and gene networks was determined by Gene Ontology and DAVID (http://david.abcc.ncifcrf.gov/summary.jsp; through BBID, BIOCARTA and KEGG annotations). All experiments were repeated ≥3 times. The data exhibited normal distribution (where applicable). For animal studies, each biological replicate consists of 3-5 mouse tissues or cell cultures per genotype per time point or treatment (unless stated otherwise). None of the samples or animals was excluded from the experiment. The animals or the experiments were not randomized. The investigators were not blinded to allocation during animal experiments and outcome assessment.

## REFERENCES

1. Ioannidou, A., Goulielmaki, E. & Garinis, G. A. DNA damage: From chronic inflammation to age-related deterioration. *Frontiers in Genetics* **7**, (2016).

2. Hoeijmakers, J. H. J. DNA Damage, Aging, and Cancer. *N. Engl. J. Med.* **361**, 1475–1485 (2009).

3. Hoeijmakers, J. H. J. Genome maintenance mechanisms are critical for preventing cancer as well as other aging-associated diseases. *Mech. Ageing Dev.* **128**, 460–462 (2007).

4. Shrivastav, M., De Haro, L. P. & Nickoloff, J. A. Regulation of DNA double-strand break repair pathway choice. *Cell Res.* **18**, 134–147 (2008).

5. Hashimoto, S., Anai, H. & Hanada, K. Mechanisms of interstrand DNA crosslink repair and human disorders. *Genes Environ.* **38**, 9 (2016).

6. Kunkel, T. A. & Erie, D. A. DNA MISMATCH REPAIR. *Annu. Rev. Biochem.* **74**, 681–710 (2005).

7. David, S. S., O'Shea, V. L. & Kundu, S. Base-excision repair of oxidative DNA damage. *Nature* **447**, 941–950 (2007).

8. Costa, R. M. A., Chiganças, V., da Silva Galhardo, R., Carvalho, H. & Menck, C. F. M. The eukaryotic nucleotide excision repair pathway. *Biochimie* **85**, 1083–1099 (2003).

9. Maréchal, A. & Zou, L. DNA damage sensing by the ATM and ATR kinases. *Cold Spring Harb. Perspect. Biol.* **5**, 1–17 (2013).

10. Burgess, R. C. & Misteli, T. Not All DDRs Are Created Equal: Non-Canonical DNA Damage Responses. *Cell* **162**, 944–947 (2015).

11. Garinis, G. A., van der Horst, G. T. J., Vijg, J. & Hoeijmakers, J. H. J. DNA damage and ageing: New-age ideas for an age-old problem. *Nature Cell Biology* **10**, 1241–1247 (2008).

12. O'Driscoll, M. Diseases associated with defective responses to DNA damage. *Cold Spring Harb. Perspect. Biol.* **4**, (2012).

13. Danilova, N. The evolution of immune mechanisms. *Journal of Experimental Zoology Part B: Molecular and Developmental Evolution* **306**, 496–520 (2006).

14. Weissman, I. L. & Shizuru, J. A. The origins of the identification and isolation of hematopoietic stem cells, and their capability to induce donor-specific transplantation tolerance and treat autoimmune diseases. *Blood* **112**, 3543–3553 (2008).

15. Gasteiger, G. *et al.* Cellular Innate Immunity: An Old Game with New Players. *J. Innate Immun.* **9**, 111–125 (2017).

16. De Kleer, I., Willems, F., Lambrecht, B. & Goriely, S. Ontogeny of myeloid cells. *Front. Immunol.* **5**, 1–11 (2014).

17. Midwood, K. S. & Piccinini, A. M. DAMPening inflammation by modulating TLR signalling. *Mediators of Inflammation* **2010**, (2010).

18. Methot, S. P. & Di Noia, J. M. Molecular Mechanisms of Somatic Hypermutation and Class Switch Recombination. in *Advances in Immunology* **133**, 37–87 (Academic Press Inc., 2017).

19. Chaplin, D. D. Overview of the immune response. *J. Allergy Clin. Immunol.* **125**, S3–S23 (2010).

20. Raje, N. & Dinakar, C. Overview of Immunodeficiency Disorders. *Immunol. Allergy Clin. North Am.* **35**, 599–623 (2015).

21. Terabayashi, T. & Hanada, K. Genome instability syndromes caused by impaired DNA repair and aberrant DNA damage responses. *Cell Biology and Toxicology* **34**, 337–350 (2018).

22. Vermeij, W. P., Hoeijmakers, J. H. J. & Pothof, J. Aging: Not all DNA damage is equal. *Curr. Opin. Genet. Dev.* **26**, 124–130 (2014).

23. Ribezzo, F., Shiloh, Y. & Schumacher, B. Systemic DNA damage responses in aging and diseases. *Semin. Cancer Biol.* **37**–**38**, 26–35 (2016).

24. Ermolaeva, M. A., Dakhovnik, A. & Schumacher, B. Quality control mechanisms in cellular and systemic DNA damage responses. *Ageing Res. Rev.* **23**, 3–11 (2015).

25. Pateras, I. S. *et al.* The DNA damage response and immune signaling alliance: Is it good or bad? Nature decides when and where. *Pharmacol. Ther.* **154**, 36–56 (2015).

26. Nakad, R. & Schumacher, B. DNA damage response and immune defense: Links and mechanisms. *Front. Genet.* **7**, 1–10 (2016).

27. Prochazkova, J. & Loizou, J. I. Programmed DNA breaks in lymphoid cells: Repair mechanisms and consequences in human disease. *Immunology* **147**, 11–20 (2016).

28. Bednarski, J. J. & Sleckman, B. P. Lymphocyte development: integration of DNA damage response signaling. *Adv. Immunol.* **116**,

175–204 (2012).

29. Zha, S. *et al.* Ataxia telangiectasia-mutated protein and DNA-dependent protein kinase have complementary V(D)J recombination functions. *Proc. Natl. Acad. Sci. U. S. A.* **108**, 2028–2033 (2011).

30. Ma, Y., Pannicke, U., Schwarz, K. & Lieber, M. R. Hairpin opening and overhang processing by an Artemis/DNA-dependent protein kinase complex in nonhomologous end joining and V(D)J recombination. *Cell* **108**, 781–794 (2002).

31. Goodarzi, A. A. *et al.* DNA-PK autophosphorylation facilitates Artemis endonuclease activity. *EMBO J.* **25**, 3880–3889 (2006).

32. Bredemeyer, A. L. *et al.* DNA double-strand breaks activate a multi-functional genetic program in developing lymphocytes. *Nature* **456**, 819–823 (2008).

33. Steinel, N. C. *et al.* The Ataxia telangiectasia mutated kinase controls Igκ allelic exclusion by inhibiting secondary Vκ-to-Jκ rearrangements. *J. Exp. Med.* **210**, 233–239 (2013).

34. Pilzecker, B. & Jacobs, H. Mutating for good: DNA damage responses during somatic hypermutation. *Front. Immunol.* **10**, 1–13 (2019).

35. Chahwan, R., Edelmann, W., Scharff, M. D. & Roa, S. Mismatch-mediated error prone repair at the immunoglobulin genes. *Biomed. Pharmacother.* **65**, 529–536 (2011).

36. Xu, Z. *et al.* DNA lesions and repair in immunoglobulin class switch recombination and somatic hypermutation. *Ann. N. Y. Acad. Sci.* **1050**, 146–162 (2005).

37. Bregenhorn, S., Kallenberger, L., Artola-Borán, M., Peña-Diaz, J. & Jiricny, J. Non-canonical uracil processing in DNA gives rise to double-strand breaks and deletions: Relevance to class switch recombination. *Nucleic Acids Res.* **44**, 2691–2705 (2016).

38. Gapud, E. J. & Sleckman, B. P. Unique and redundant functions of ATM and DNA-PKcs during V(D)J recombination. *Cell Cycle* **10**, 1928–1935 (2011).

39. Weitzman, M. D. & Fradet-Turcotte, A. Virus DNA Replication and the Host DNA Damage Response. *Annu. Rev. Virol.* **5**, 141–164 (2018).

40. Morales, A. J. *et al.* A type I IFN-dependent DNA damage response regulates the genetic program and inflammasome activation in macrophages. *Elife* **6**, 1–20 (2017).

41. Härtlova, A. *et al.* DNA Damage Primes the Type I Interferon System via the Cytosolic DNA Sensor STING to Promote Anti-Microbial Innate Immunity. *Immunity* **42**, 332–343 (2015).

42. Kim, T. *et al.* Activation of interferon regulatory factor 3 in response to DNA-damaging agents. *J. Biol. Chem.* **274**, 30686–30689 (1999).

43. Karpova, A. Y., Trost, M., Murray, J. M., Cantley, L. C. & Howley, P. M. Interferon regulatory factor-3 is an in vivo target of DNA-PK. *Proc. Natl. Acad. Sci. U. S. A.* **99**, 2818–2823 (2002).

44. Dutta, D. *et al.* BRCA1 Regulates IFI16 Mediated Nuclear Innate Sensing of Herpes Viral DNA and Subsequent Induction of the Innate Inflammasome and Interferon-β Responses. *PLoS Pathog.* **11**, (2015).

45. Bhattacharya, S. *et al.* RAD51 interconnects between DNA replication, DNA repair and immunity. *Nucleic Acids Res.* **45**, 4590–4605 (2017).

46. Chatzinikolaou, G., Karakasilioti, I. & Garinis, G. A. DNA damage and innate immunity: Links and trade-offs. *Trends Immunol.* **35**, 429–435 (2014).

47. Mangerich, A. & Bürkle, A. Pleiotropic cellular functions of PARP1 in longevity and aging: Genome maintenance meets inflammation. *Oxidative Medicine and Cellular Longevity* (2012). doi:10.1155/2012/321653

48. Permata, T. B. M. *et al.* Base excision repair regulates PD-L1 expression in cancer cells. *Oncogene* **38**, 4452–4466 (2019).

49. Pan, L. *et al.* OGG1-DNA interactions facilitate NF-k B binding to DNA targets. *Sci. Rep.* **7**, (2017).

50. Li, G. *et al.* 8-Oxoguanine-DNA glycosylase 1 deficiency modifies allergic airway inflammation by regulating STAT6 and IL-4 in cells and in mice. *Free Radic. Biol. Med.* **52**, 392–401 (2012).

51. Lee, H.-M. *et al.* Apurinic/apyrimidinic endonuclease 1 is a key modulator of keratinocyte inflammatory responses. *J. Immunol.* **183**, 6839–48 (2009).

52. Neves-Costa, A. & Moita, L. F. Modulation of inflammation and disease tolerance by DNA damage response pathways. *FEBS J.* **284**, 680–698 (2017).

53. Soriani, A. *et al.* ATM-ATR-dependent up-regulation of DNAM-1 and NKG2D ligands on multiple myeloma cells by therapeutic agents results in enhanced NK-cell susceptibility and is associated with a senescent phenotype. *Blood* **113**, 3503–3511 (2009).

54. Kawai, T. & Akira, S. Toll-like Receptors and Their Crosstalk with Other Innate Receptors in Infection and Immunity. *Immunity* **34**, 637–650 (2011).

55. Roers, A., Hiller, B. & Hornung, V. Recognition of Endogenous Nucleic Acids by the Innate Immune System. *Immunity* **44**, 739–754 (2016).

56. Dempsey, A. & Bowie, A. G. Innate immune recognition of DNA: A recent history. *Virology* **479**–**480**, 146–152 (2015).

57. Hornung, V. *et al.* AIM2 recognizes cytosolic dsDNA and forms a caspase-1-activating inflammasome with ASC. *Nature* **458**, 514–518 (2009).

58. Chiu, Y. H., MacMillan, J. B. & Chen, Z. J. RNA Polymerase III Detects Cytosolic DNA and Induces Type I Interferons through the RIG-I Pathway. *Cell* **138**, 576–591 (2009).

59. Reikine, S., Nguyen, J. B. & Modis, Y. Pattern recognition and signaling mechanisms of RIG-I and MDA5. *Front. Immunol.* **5**, 1–7 (2014).

60. Zhang, X. *et al.* Cutting Edge: Ku70 Is a Novel Cytosolic DNA Sensor That Induces Type III Rather Than Type I IFN. *J. Immunol.* **186**, 4541–4545 (2011).

61. Ferguson, B. J., Mansur, D. S., Peters, N. E., Ren, H. & Smith, G. L. DNA-PK is a DNA sensor for IRF-3-dependent innate immunity. *Elife* **2012**, 1–17 (2012).

62. Kondo, T. *et al.* DNA damage sensor MRE11 recognizes cytosolic double-stranded DNA and induces type i interferon by regulating STING trafficking. *Proc. Natl. Acad. Sci. U. S. A.* **110**, 2969–2974 (2013).

63. Roth, S. *et al.* Rad50-CARD9 interactions link cytosolic DNA sensing to IL-1β production. *Nat. Immunol.* **15**, 538–545 (2014).

64. Marteijn, J. A., Lans, H., Vermeulen, W. & Hoeijmakers, J. H. J. Understanding nucleotide excision repair and its roles in cancer and ageing. *Nat. Rev. Mol. Cell Biol.* **15**, 465–481 (2014).

65. Scharer, O. D. Nucleotide Excision Repair in Eukaryotes. *Cold Spring Harb. Perspect. Biol.* **5**, a012609–a012609 (2013).

66. Vermeulen, W. & Fousteri, M. Mammalian transcription-coupled excision repair. *Cold Spring Harb. Perspect. Biol.* **5**, 1–16 (2013).

67. Sugasawa, K. Molecular mechanisms of DNA damage recognition for mammalian nucleotide excision repair. *DNA Repair (Amst).* **44**, 110–117 (2016).

68. Spivak, G. Nucleotide excision repair in humans. *DNA Repair* **36**, 13–18 (2015).

69. Trego, K. S. *et al.* The DNA repair endonuclease XPG interacts directly and functionally with the WRN helicase defective in Werner syndrome. *Cell Cycle* **10**, 1998–2007 (2011).

70. Schärer, O. D. XPG: Its products and biological roles. *Advances in Experimental Medicine and Biology* **637**, 83–92 (2008).

71. Rimel, J. K. & Taatjes, D. J. The essential and multifunctional TFIIH complex. *Protein Sci.* **27**, 1018–1037 (2018).

72. Kamileri, I., Karakasilioti, I. & Garinis, G. A. Nucleotide excision repair: New tricks with old bricks. *Trends Genet.* **28**, 566–573 (2012).

73. Apostolou, Z., Chatzinikolaou, G., Stratigi, K. & Garinis, G. A. Nucleotide Excision Repair and Transcription-Associated Genome Instability. *BioEssays : news and reviews in molecular, cellular and developmental biology* **41**, e1800201 (2019).

74. Le May, N., Fradin, D., Iltis, I., Bougnères, P. & Egly, J. M. XPG and XPF Endonucleases Trigger Chromatin Looping and DNA Demethylation for Accurate Expression of Activated Genes. *Mol. Cell* **47**, 622–632 (2012).

75. Chatzinikolaou, G. *et al.* ERCC1-XPF cooperates with CTCF and cohesin to facilitate the developmental silencing of imprinted genes. *Nat. Cell Biol.* **19**, 421–432 (2017).

76. Lake, R. J., Boetefuer, E. L., Won, K. J. & Fan, H. Y. The CSB chromatin remodeler and CTCF architectural protein cooperate in response to oxidative stress. *Nucleic Acids Res.* **44**, 2125–2135 (2016).

77. Schärer, O. D. ERCC1-XPF endonuclease—positioned to cut. *EMBO J.* **36**, 1993–1995 (2017).

78. Manandhar, M., Boulware, K. S. & Wood, R. D. The ERCC1 and ERCC4 (XPF) genes and gene products. *Gene* **569**, 153–161 (2015).

79. Batenburg, N. L., Thompson, E. L., Hendrickson, E. A. & Zhu, X. Cockayne syndrome group B protein regulates DNA double-strand break repair and checkpoint activation . *EMBO J.* **34**, 1399–1416 (2015).

80. Stevnsner, T., Muftuoglu, M., Aamann, M. D. & Bohr, V. A. The role of Cockayne Syndrome group B (CSB) protein in base excision repair and aging. *Mech. Ageing Dev.* **129**, 441–448 (2008).

81. Menoni, H. *et al.* The transcription-coupled DNA repair-initiating protein CSB promotes XRCC1 recruitment to oxidative DNA damage. *Nucleic Acids Res.* **46**, 7747–7756 (2018).

82. Melis, J. P. M., Van Steeg, H. & Luijten, M. Oxidative DNA damage and nucleotide excision repair. *Antioxidants Redox Signal.* **18**, 2409–2419 (2013).

83. Kamileri, I. *et al.* Defective transcription initiation causes postnatal growth failure in a mouse model of nucleotide excision repair (NER) progeria. *Proc. Natl. Acad. Sci. U. S. A.* **109**, 2995–3000 (2012).

84. Fekete, R. Xeroderma pigmentosum/De Sanctis-Cacchione syndrome: Unusual cause of ataxia. *Case Rep. Neurol.* **6**, 83–87 (2014).

85. Tiwari, V. & Wilson, D. M. DNA Damage and Associated DNA Repair Defects in Disease and Premature Aging. *Am. J. Hum. Genet.* **105**, 237–257 (2019).

86. Horibata, K. *et al.* Complete absence of Cockayne syndrome group B gene product gives rise to UV-sensitive syndrome but not Cockayne syndrome. *Proc. Natl. Acad. Sci. U. S. A.* **101**, 15410–15415 (2004).

87. Kraemer, K. H. *et al.* Xeroderma pigmentosum, trichothiodystrophy and Cockayne syndrome: A complex genotype-phenotype relationship. *Neuroscience* **145**, 1388–1396 (2007).

88. Agathangelou, K., Apostolou, Z. & Garinis, G. A. Nuclear DNA damage

and ageing. in *Subcellular Biochemistry* **90**, 309–322 (Springer New York, 2018).

89. Niedernhofer, L. J. Nucleotide excision repair deficient mouse models and neurological disease. *DNA Repair (Amst).* **7**, 1180–1189 (2008).

90. Barnhoorn, S. *et al.* Cell-Autonomous Progeroid Changes in Conditional Mouse Models for Repair Endonuclease XPG Deficiency. *PLoS Genet.* **10**, e1004686 (2014).

91. Terabayashi, T. & Hanada, K. Genome instability syndromes caused by impaired DNA repair and aberrant DNA damage responses. *Cell Biol. Toxicol.* **34**, 337–350 (2018).

92. Gregg, S. Q., Robinson, A. R. & Niedernhofer, L. J. Physiological consequences of defects in ERCC1-XPF DNA repair endonuclease. *DNA Repair (Amst).* **10**, 781–791 (2011).

93. Kashiyama, K. *et al.* Malfunction of nuclease ERCC1-XPF results in diverse clinical manifestations and causes Cockayne syndrome, xeroderma pigmentosum, and Fanconi anemia. *Am. J. Hum. Genet.* **92**, 807–819 (2013).

94. Jaspers, N. G. J. *et al.* First reported patient with human ERCC1 deficiency has cerebro-oculo-facio- skeletal syndrome with a mild defect in nucleotide excision repair and severe developmental failure. *Am. J. Hum. Genet.* **80**, 457–466 (2007).

95. Bogliolo, M. *et al.* Mutations in ERCC4, encoding the DNA-repair endonuclease XPF, cause Fanconi anemia. *Am. J. Hum. Genet.* **92**, 800–806 (2013).

96. Sands, A. T., Abuin, A., Sanchez, A., Conti, C. J. & Bradley, A. High susceptibility to ultraviolet-induced carcinogenesis in mice lacking XPC. *Nature* **377**, 162–165 (1995).

97. Cheo, D. L. *et al.* Characterization of defective nucleotide excision repair in XPC mutant mice. *Mutat. Res. - Fundam. Mol. Mech. Mutagen.* **374**, 1–9 (1997).

98. Van der Horst, G. T. J. *et al.* Defective transcription-coupled repair in Cockayne syndrome B mice is associated with skin cancer predisposition. *Cell* **89**, 425–435 (1997).

99. Nakane, H. *et al.* High incidence of ultraviolet-B-or chemical-carcinogen-induced skin tumours in mice lacking the xeroderma pigmentosum group A gene. *Nature* **377**, 165–168 (1995).

100. De Boer, J. *et al.* Premature aging in mice deficient in DNA repair and transcription. *Science (80-. ).* **296**, 1276–1279 (2002).

101. Andressoo, J. O. *et al.* An Xpd mouse model for the combined xeroderma pigmentosum/Cockayne syndrome exhibiting both cancer predisposition and segmental progeria. *Cancer Cell* **10**, 121–132 (2006).

102. Andressoo, J.-O. *et al.* An Xpb Mouse Model for Combined Xeroderma Pigmentosum and Cockayne Syndrome Reveals Progeroid Features upon Further Attenuation of DNA Repair. *Mol. Cell. Biol.* **29**, 1276–1290 (2009).

103. Tian, M., Shinkura, R., Shinkura, N. & Alt, F. W. Growth Retardation, Early Death, and DNA Repair Defects in Mice Deficient for the Nucleotide Excision Repair Enzyme XPF. *Mol. Cell. Biol.* **24**, 1200–1205 (2004).

104. Niedernhofer, L. J. *et al.* A new progeroid syndrome reveals that genotoxic stress suppresses the somatotroph axis. *Nature* **444**, 1038–1043 (2006).

105. Weeda, G. *et al.* Disruption of mouse ERCC1 results in a novel repair syndrome with growth failure, nuclear abnormalities and senescence. *Curr. Biol.* **7**, 427–439 (1997).

106. Van De Ven, M. *et al.* Adaptive stress response in segmental progeria resembles long-lived dwarfism and calorie restriction in mice. *PLoS Genet.* **2**, 2013–2025 (2006).

107. Schumacher, B. *et al.* Delayed and accelerated aging share common longevity assurance mechanisms. *PLoS Genet.* **4**, (2008).

108. Garinis, G. A. *et al.* Persistent transcription-blocking DNA lesions trigger somatic growth attenuation associated with longevity. *Nat. Cell Biol.* **11**, 604–615 (2009).

109. Oishi, Y. & Manabe, I. Macrophages in age-related chronic inflammatory diseases. *npj Aging Mech. Dis.* **2**, 1–8 (2016).

110. Cavanagh, M. M., Weyand, C. M. & Goronzy, J. J. Chronic inflammation and aging: DNA damage tips the balance. *Curr. Opin. Immunol.* **24**, 488–493 (2012).

111. McHugh, D. & Gil, J. Senescence and aging: Causes, consequences, and therapeutic avenues. *J. Cell Biol.* **217**, 65–77 (2018).

112. Kõks, S. *et al.* Mouse models of ageing and their relevance to disease. *Mech. Ageing Dev.* **160**, 41–53 (2016).

113. Bernal, G. M. *et al.* Loss of Nfkb1 leads to early onset aging. *Aging (Albany. NY).* **6**, 931–943 (2014).

114. Tilstra, J. S. *et al.* NF-κB inhibition delays DNA damage - Induced senescence and aging in mice. *J. Clin. Invest.* **122**, 2601–2612 (2012).

115. Osorio, F. G. *et al.* Nuclear lamina defects cause ATM-dependent NF-κB activation and link accelerated aging to a systemic inflammatory response. *Genes Dev.* **26**, 2311–2324 (2012).

116. Karakasilioti, I. *et al.* DNA damage triggers a chronic autoinflammatory response, leading to fat depletion in NER progeria. *Cell Metab.* **18**, 403–415 (2013).

117. Ovadya, Y. *et al.* Impaired immune surveillance accelerates accumulation of senescent cells and aging. *Nat. Commun.* **9**, (2018).

118. Febbraio, M. A. Role of interleukins in obesity: Implications for metabolic disease. *Trends Endocrinol. Metab.* **25**, 312–319 (2014).

119. Shimizu, I., Yoshida, Y., Suda, M. & Minamino, T. DNA damage response and metabolic disease. *Cell Metab.* **20**, 967–977 (2014).

120. Doig, J. *et al.* Mice with skin-specific DNA repair gene (Ercc1) inactivation are hypersensitive to ultraviolet irradiation-induced skin cancer and show more rapid actinic progression. *Oncogene* **25**, 6229–6238 (2006).

121. Clausen, B. E., Burkhardt, C., Reith, W., Renkawitz, R. & Förster, I. Conditional gene targeting in macrophages and granulocytes using LysMcre mice. *Transgenic Res.* **8**, 265–277 (1999).

122. Evangelou, K. *et al.* Robust, universal biomarker assay to detect senescent cells in biological specimens. *Aging Cell* **16**, 192–197 (2017).

123. Levine, B., Mizushima, N. & Virgin, H. W. Autophagy in immunity and inflammation. *Nature* **469**, 323–35 (2011).

124. Schröder, M. Endoplasmic reticulum stress responses. *Cellular and Molecular Life Sciences* **65**, 862–894 (2008).

125. Dicks, N., Gutierrez, K., Michalak, M., Bordignon, V. & Agellon, L. B. Endoplasmic reticulum stress, genome damage, and cancer. *Frontiers in Oncology* **5**, (2015).

126. Saglar, E., Unlu, S., Babalioglu, I., Gokce, S. C. & Mergen, H. Assessment of ER stress and autophagy induced by ionizing radiation in both radiotherapy patients and ex vivo irradiated samples. *J. Biochem. Mol. Toxicol.* **28**, 413–417 (2014).

127. van Beek, A. A., Van den Bossche, J., Mastroberardino, P. G., de Winther, M. P. J. & Leenen, P. J. M. Metabolic Alterations in Aging Macrophages: Ingredients for Inflammaging? *Trends Immunol.* **40**, 113–127 (2019).

128. Lee, A. S. The ER chaperone and signaling regulator GRP78/BiP as a monitor of endoplasmic reticulum stress. *Methods* **35**, 373–381 (2005).

129. Zhang, Z., Singh, R. & Aschner, M. Methods for the Detection of Autophagy in Mammalian Cells. *Curr. Protoc. Toxicol.* **69**, 20.12.1-20.12.26 (2016).

130. Komatsu, M. *et al.* Homeostatic levels of p62 control cytoplasmic inclusion body formation in autophagy-deficient mice. *Cell* **131**, 1149–63 (2007).

131. Nakamura, N. Emerging new roles of GM130, a cis-Golgi matrix protein, in higher order cell functions. *J. Pharmacol. Sci.* **112**, 255–64 (2010).

132. Nacife, V. P. *et al.* Morphological and biochemical characterization of

macrophages activated by carrageenan and lipopolysaccharide in vivo. *Cell Struct. Funct.* **29**, 27–34 (2004).

133. Hessvik, N. P. & Llorente, A. Current knowledge on exosome biogenesis and release. *Cellular and Molecular Life Sciences* **75**, 193–208 (2018).

134. Peterson, K. R., Cottam, M. A., Kennedy, A. J. & Hasty, A. H. Macrophage-Targeted Therapeutics for Metabolic Disease. *Trends in Pharmacological Sciences* **39**, 536–546 (2018).

135. Duan, Y. *et al.* Inflammatory links between high fat diets and diseases. *Front. Immunol.* **9**, (2018).

136. Radi, Z. A., Kehrli, M. E. & Ackermann, M. R. Cell adhesion molecules, leukocyte trafficking, and strategies to reduce leukocyte infiltration. *J. Vet. Intern. Med.* **15**, 516–529 (2001).

137. Rao, R. M., Yang, L., Garcia-Cardena, G. & Luscinskas, F. W. Endothelial-dependent mechanisms of leukocyte recruitment to the vascular wall. *Circulation Research* **101**, 234–247 (2007).

138. Thomas, D. & Apovian, C. Macrophage functions in lean and obese adipose tissue. *Metabolism: Clinical and Experimental* **72**, 120–143 (2017).

139. Mosser, D. M. & Edwards, J. P. Exploring the full spectrum of macrophage activation. *Nature Reviews Immunology* **8**, 958–969 (2008).

140. Viola, A., Munari, F., Sánchez-Rodríguez, R., Scolaro, T. & Castegna, A. The Metabolic Signature of Macrophage Responses. *Front. Immunol.* **10**, 1462 (2019).

141. Sica, A., Erreni, M., Allavena, P. & Porta, C. Macrophage polarization in pathology. *Cellular and Molecular Life Sciences* **72**, 4111–4126 (2015).

142. Parisi, L. *et al.* Macrophage Polarization in Chronic Inflammatory Diseases: Killers or Builders? *Journal of Immunology Research* **2018**, (2018).

143. Goitre, L., Trapani, E., Trabalzini, L. & Retta, S. F. The ras superfamily of small GTPases: The unlocked secrets. *Methods in Molecular Biology* **1120**, 1–18 (2014).

144. Bustelo, X. R., Sauzeau, V. & Berenjeno, I. M. GTP-binding proteins of the Rho/Rac family: Regulation, effectors and functions in vivo. *BioEssays* **29**, 356–370 (2007).

145. Wilson, K. F., Erickson, J. W., Antonyak, M. A. & Cerione, R. A. Rho GTPases and their roles in cancer metabolism. *Trends Mol. Med.* **19**, 74–82 (2013).

146. Marei, H. & Malliri, A. Rac1 in human diseases: The therapeutic potential of targeting Rac1 signaling regulatory mechanisms. *Small GTPases* **8**, 139–163 (2017).

147. Qin, C., Liu, R. & Liu, H. The conflicting role of Rac1 in inflammation. *Inflamm. Cell Signal.* **2**, 922 (2015).

148. Blanc, L. & Vidal, M. New insights into the function of Rab GTPases in the context of exosomal secretion. *Small GTPases* **9**, 95–106 (2018).

149. Chiu, T. T., Sun, Y., Koshkina, A. & Klip, A. Rac-1 superactivation triggers insulin-independent glucose transporter 4 (GLUT4) translocation that bypasses signaling defects exerted by c-Jun N-terminal kinase (JNK)- and ceramide-induced insulin resistance. *J. Biol. Chem.* **288**, 17520–31 (2013).

150. Chiu, T. T., Jensen, T. E., Sylow, L., Richter, E. A. & Klip, A. Rac1 signalling towards GLUT4/glucose uptake in skeletal muscle. *Cell. Signal.* **23**, 1546–54 (2011).

151. Shi, Y. *et al.* Rac1-Mediated DNA Damage and Inflammation Promote Nf2 Tumorigenesis but Also Limit Cell-Cycle Progression. *Dev. Cell* **39**, 452–465 (2016).

152. Prashar, A., Schnettger, L., Bernard, E. M. & Gutierrez, M. G. Rab GTPases in immunity and inflammation. *Frontiers in Cellular and Infection Microbiology* **7**, (2017).

153. Doyle, L. M. & Wang, M. Z. Overview of Extracellular Vesicles, Their Origin, Composition, Purpose, and Methods for Exosome Isolation and Analysis. *Cells* **8**, 727 (2019).

154. Desdín-Micó, G. & Mittelbrunn, M. Role of exosomes in the protection of cellular homeostasis. *Cell Adh. Migr.* **11**, 127–134 (2017).

155. Takasugi, M. Emerging roles of extracellular vesicles in cellular senescence and aging. *Aging Cell* **17**, (2018).

156. Kadota, T. *et al.* Emerging role of extracellular vesicles as a senescence-associated secretory phenotype: Insights into the pathophysiology of lung diseases. *Mol. Aspects Med.* **60**, 92–103 (2018).

157. Veerman, R. E., Güçlüler Akpinar, G., Eldh, M. & Gabrielsson, S. Immune Cell-Derived Extracellular Vesicles – Functions and Therapeutic Applications. *Trends in Molecular Medicine* **25**, 382–394 (2019).

158. Robbins, P. D. Extracellular vesicles and aging. *Stem Cell Investigation* **4**, (2017).

159. Robbins, P. D. & Morelli, A. E. Regulation of immune responses by extracellular vesicles. *Nat. Rev. Immunol.* **14**, 195–208 (2014).

160. Martínez, M. C. & Andriantsitohaina, R. Extracellular Vesicles in Metabolic Syndrome. *Circ. Res.* **120**, 1674–1686 (2017).

161. Lee, M. J., Park, D. H. & Kang, J. H. Exosomes as the source of biomarkers of metabolic diseases. *Annals of Pediatric Endocrinology and Metabolism* **21**, 119–125 (2016).

162. Thorens, B. & Mueckler, M. Glucose transporters in the 21st Century. *American Journal of Physiology - Endocrinology and Metabolism* **298**, E141–E145 (2010).

163. Ebeling, P., Koistinen, H. A. & Koivisto, V. A. Insulin-independent glucose transport regulates insulin sensitivity. *FEBS Letters* **436**, 301–303 (1998).

164. Lee, E. E. *et al.* A Protein Kinase C Phosphorylation Motif in GLUT1 Affects Glucose Transport and is Mutated in GLUT1 Deficiency Syndrome. *Mol. Cell* **58**, 845–853 (2014).

165. Palikaras, K. & Tavernarakis, N. Measuring Oxygen Consumption Rate in Caenorhabditis elegans. *BIO-PROTOCOL* **6**, (2016).

166. Dickinson, S., Hancock, D. P., Petocz, P., Ceriello, A. & Brand-Miller, J. High–glycemic index carbohydrate increases nuclear factor-κB activation in mononuclear cells of young, lean healthy subjects. *Am. J. Clin. Nutr.* **87**, 1188–1193 (2008).

167. Dhindsa, S. *et al.* Differential effects of glucose and alcohol on reactive oxygen species generation and intranuclear nuclear factor-κB in mononuclear cells. *Metabolism.* **53**, 330–334 (2004).

168. Prattichizzo, F. *et al.* Inflammageing and metaflammation: The yin and yang of type 2 diabetes. *Ageing Res. Rev.* **41**, 1–17 (2018).

169. Rønningen, T., Shah, A., Reiner, A. H., Collas, P. & Moskaug, J. Ø. Epigenetic priming of inflammatory response genes by high glucose in adipose progenitor cells. *Biochem. Biophys. Res. Commun.* **467**, 979–86 (2015).

170. Fruman, D. A. *et al.* The PI3K Pathway in Human Disease. *Cell* **170**, 605–635 (2017).

171. Saxton, R. A. & Sabatini, D. M. mTOR Signaling in Growth, Metabolism, and Disease. *Cell* **168**, 960–976 (2017).

172. Zha, X. *et al.* NFκB up-regulation of glucose transporter 3 is essential for hyperactive mammalian target of rapamycin-induced aerobic glycolysis and tumor growth. *Cancer Lett.* **359**, 97–106 (2015).

173. Hakem, R. DNA-damage repair; the good, the bad, and the ugly. *EMBO J.* **27**, 589–605 (2008).

174. Jackson, S. P. & Bartek, J. The DNA-damage response in human biology and disease. *Nature* **461**, 1071–1078 (2009).

175. Keenan, C. R. & Allan, R. S. Epigenomic drivers of immune dysfunction in aging. *Aging Cell* **18**, (2019).

176. Gorbunova, V., Seluanov, A., Mao, Z. & Hine, C. Changes in DNA repair during aging. *Nucleic Acids Research* **35**, 7466–7474 (2007).

177. Chen, Q. *et al.* DNA damage drives accelerated bone aging via an NF-κ B-dependent mechanism. *J. Bone Miner. Res.* **28**, 1214–1228 (2013).

178. Wynn, T. A., Chawla, A. & Pollard, J. W. Macrophage biology in development, homeostasis and disease. *Nature* **496**, 445–55 (2013).

179. Farber-Katz, S. E. *et al.* DNA damage triggers golgi dispersal via DNA-PK and GOLPH3. *Cell* **156**, 413–427 (2014).

180. Cao, S. S., Luo, K. L. & Shi, L. Endoplasmic Reticulum Stress Interacts With Inflammation in Human Diseases. *J. Cell. Physiol.* **231**, 288–94 (2016).

181. Song, M. & Cubillos-Ruiz, J. R. Endoplasmic Reticulum Stress Responses in Intratumoral Immune Cells: Implications for Cancer Immunotherapy. *Trends Immunol.* **40**, 128–141 (2019).

182. Germic, N., Frangez, Z., Yousefi, S. & Simon, H.-U. Regulation of the innate immune system by autophagy: monocytes, macrophages, dendritic cells and antigen presentation. *Cell Death Differ.* **26**, 715–727 (2019).

183. Clarke, A. J. & Simon, A. K. Autophagy in the renewal, differentiation and homeostasis of immune cells. *Nature Reviews Immunology* **19**, 170–183 (2019).

184. Hu, H. *et al.* Arginase inhibition ameliorates adipose tissue inflammation in mice with diet-induced obesity. *Biochem. Biophys. Res. Commun.* **464**, 840–7 (2015).

185. Miller, A. M. *et al.* Interleukin-33 induces protective effects in adipose tissue inflammation during obesity in mice. *Circ. Res.* **107**, 650–658 (2010).

186. Lacy, P. & Stow, J. L. Cytokine release from innate immune cells: Association with diverse membrane trafficking pathways. *Blood* **118**, 9–18 (2011).

187. Murray, R. Z. & Stow, J. L. Cytokine secretion in macrophages: SNAREs, Rabs, and membrane trafficking. *Frontiers in Immunology* **5**, (2014).

188. Hotamisligil, G. S. Foundations of Immunometabolism and Implications for Metabolic Health and Disease. *Immunity* **47**, 406–420 (2017).

189. Van Der Pluijm, I. *et al.* Impaired genome maintenance suppresses the growth hormone-insulin-like growth factor 1 axis in mice with cockayne syndrome. *PLoS Biol.* **5**, 0023–0038 (2007).

190. Ermolaeva, M. A. & Schumacher, B. Systemic DNA damage responses: Organismal adaptations to genome instability. *Trends in Genetics* **30**, 95–102 (2014).

191. Ermolaeva, M. A. *et al.* DNA damage in germ cells induces an innate immune response that triggers systemic stress resistance. *Nature* **501**, 416–420 (2013).

192. Karpac, J., Younger, A. & Jasper, H. Dynamic coordination of innate immune signaling and insulin signaling regulates systemic responses to

localized DNA damage. *Dev. Cell* **20**, 841–854 (2011).

193. Lee, C.-H., Wu, S.-B., Hong, C.-H., Yu, H.-S. & Wei, Y.-H. Molecular Mechanisms of UV-Induced Apoptosis and Its Effects on Skin Residential Cells: The Implication in UV-Based Phototherapy. *Int. J. Mol. Sci.* **14**, 6414–35 (2013).

194. Huelsenbeck, S. C. *et al.* Rac1 protein signaling is required for DNA damage response stimulated by topoisomerase II poisons. *J. Biol. Chem.* **287**, 38590–9 (2012).

195. Fritz, G. & Henninger, C. Rho GTPases: Novel Players in the Regulation of the DNA Damage Response? *Biomolecules* **5**, 2417–34 (2015).

196. Prattichizzo, F. *et al.* Exosome-based immunomodulation during aging: A nano-perspective on inflamm-aging. *Mech. Ageing Dev.* **168**, 44–53 (2017).

197. Guay, C. & Regazzi, R. Exosomes as new players in metabolic organ cross-talk. *Diabetes, Obesity and Metabolism* **19**, 137–146 (2017).

198. Huang-Doran, I., Zhang, C. Y. & Vidal-Puig, A. Extracellular Vesicles: Novel Mediators of Cell Communication In Metabolic Disease. *Trends in Endocrinology and Metabolism* **28**, 3–18 (2017).

199. Deng, Z. Bin *et al.* Adipose tissue exosome-like vesicles mediate activation of macrophage-induced insulin resistance. *Diabetes* **58**, 2498–2505 (2009).

200. Møller, L. L. V., Klip, A. & Sylow, L. Rho GTPases—Emerging Regulators of Glucose Homeostasis and Metabolic Health. *Cells* **8**, 434 (2019).

201. Barros, P., Lam, E. W. F., Jordan, P. & Matos, P. Rac1 signalling modulates a STAT5/BCL-6 transcriptional switch on cell-cycle-associated target gene promoters. *Nucleic Acids Res.* **40**, 7776–7787 (2012).

202. Diekmann, D., Abo, A., Johnston, C., Segal, A. W. & Hall, A. Interaction of Rac with p67phoxand regulation of phagocytic NADPH oxidase activity. *Science (80-. ).* **265**, 531–533 (1994).

203. Ferro, E., Goitre, L., Retta, S. F. & Trabalzini, L. The Interplay between ROS and Ras GTPases: Physiological and Pathological Implications. *J. Signal Transduct.* **2012**, 1–9 (2012).

204. Kozlovsky, N. *et al.* Transcriptional activation of the Glut1 gene in response to oxidative stress in L6 myotubes. *J. Biol. Chem.* **272**, 33367–33372 (1997).

205. Grosick, R., Alvarado-Vazquez, P. A., Messersmith, A. R. & Romero-Sandoval, E. A. High glucose induces a priming effect in macrophages and exacerbates the production of pro-inflammatory cytokines after a challenge. *J. Pain Res.* **11**, 1769–1778 (2018).

206. Torres-Castro, I. *et al.* Human monocytes and macrophages undergo M1-type inflammatory polarization in response to high levels of glucose. *Immunol. Lett.* **176**, 81–9 (2016).

207. Maedler, K. *et al.* Glucose-induced β cell production of IL-1β contributes to glucotoxicity in human pancreatic islets. *J. Clin. Invest.* **110**, 851–860 (2002).

208. Kumar, P., Natarajan, K. & Shanmugam, N. High glucose driven expression of pro-inflammatory cytokine and chemokine genes in lymphocytes: molecular mechanisms of IL-17 family gene expression. *Cell. Signal.* **26**, 528–39 (2014).

209. Lafuente, N. *et al.* The deleterious effect of high concentrations of D-glucose requires pro-inflammatory preconditioning. *J. Hypertens.* **26**, 478–85 (2008).

210. Takayama, K. *et al.* mTOR signaling plays a critical role in the defects observed in muscle-derived stem/progenitor cells isolated from a murine model of accelerated aging. *J. Orthop. Res.* **35**, 1375–1382 (2017).

211. Ramos, F. J. *et al.* Rapamycin reverses elevated mTORC1 signaling in lamin A/C-deficient mice, rescues cardiac and skeletal muscle function, and extends survival. *Sci. Transl. Med.* **4**, (2012).

212. Saci, A., Cantley, L. C. & Carpenter, C. L. Rac1 regulates the activity of mTORC1 and mTORC2 and controls cellular size. *Mol. Cell* **42**, 50–61 (2011).

213. Yang, Y., Hong, Y., Cho, E., Kim, G. B. & Kim, I.-S. Extracellular vesicles as a platform for membrane-associated therapeutic protein delivery. *J. Extracell. vesicles* **7**, 1440131 (2018).

214. Margolis, L. & Sadovsky, Y. The biology of extracellular vesicles: The known unknowns. *PLOS Biol.* **17**, e3000363 (2019).

215. De Wever, O. & Hendrix, A. A supporting ecosystem to mature extracellular vesicles into clinical application. *EMBO J.* **38**, (2019).

216. Francke, A., Herold, J., Weinert, S., Strasser, R. H. & Braun-Dullaeus, R. C. Generation of mature murine monocytes from heterogeneous bone marrow and description of their properties. *J. Histochem. Cytochem.* **59**, 813–825 (2011).

217. Théry, C., Amigorena, S., Raposo, G. & Clayton, A. Isolation and Characterization of Exosomes from Cell Culture Supernatants and Biological Fluids. *Curr. Protoc. Cell Biol.* **30**, 3.22.1-3.22.29 (2006).

218. Aivaliotis, M. *et al.* Large-scale identification of N-terminal peptides in the halophilic archaea Halobacterium salinarum and Natronomonas pharaonis. *J. Proteome Res.* **6**, 2195–204 (2007).

219. Apweiler, R. The universal protein resource (UniProt) in 2010. *Nucleic Acids Res.* **38**, (2009).

220. Rappsilber, J., Ryder, U., Lamond, A. I. & Mann, M. Large-scale

proteomic analysis of the human spliceosome. *Genome Res.* **12**, 1231–45 (2002).

221. Keller, A., Nesvizhskii, A. I., Kolker, E. & Aebersold, R. Empirical statistical model to estimate the accuracy of peptide identifications made by MS/MS and database search. *Anal. Chem.* **74**, 5383–92 (2002).

222. Nesvizhskii, A. I., Keller, A., Kolker, E. & Aebersold, R. A Statistical Model for Identifying Proteins by Tandem Mass Spectrometry abilities that proteins are present in a sample on the basis. *Anal. Chem.* **75**, 4646–4658 (2003).

223. Searle, B. C., Turner, M. & Nesvizhskii, A. I. Improving sensitivity by probabilistically combining results from multiple MS/MS search methodologies. *J. Proteome Res.* **7**, 245–53 (2008).

224. Asara, J. M., Christofk, H. R., Freimark, L. M. & Cantley, L. C. A label-free quantification method by MS/MS TIC compared to SILAC and spectral counting in a proteomics screen. *Proteomics* **8**, 994–9 (2008).

225. Szklarczyk, D. *et al.* The STRING database in 2011: functional interaction networks of proteins, globally integrated and scored. *Nucleic Acids Res.* **39**, D561-8 (2011).